Quantitative Magnetization Transfer Imaging:

Theory and Applications

By

Pouria Mossahebi

A dissertation submitted in partial fulfillment of

the requirement for the degree of

Doctor of Philosophy

(Biomedical Engineering)

at the

UNIVERSITY OF WISCONSIN-MADISON

2013

Date of final oral examination: 10/30/2013

The dissertation is approved by the following members of the Final Oral Committee:

Aaron S. Field, Associate Professor, Biomedical Engineering and Radiology

Andrew L. Alexander, Professor, Medical Physics and Psychiatry

Walter F. Block, Professor, Biomedical Engineering and Medical Physics

Mary Elizabeth Meyerand, Professor, Biomedical Engineering and Medical Physics

Alexey A. Samsonov, Associate Scientist, Radiology

Quantitative Magnetization Transfer Imaging:

Theory and Applications

Pouria Mossahebi

Under the supervision of Professor Walter F. Block, PhD

At the University of Wisconsin-Madison

Abstract

Magnetic resonance imaging (MRI) is a medical imaging modality that produces images of soft tissues and metabolic processes in the human body. While contrast in conventional MRI is generated by protons with free mobility, magnetization transfer (MT) imaging is commonly recognized as a source of essential information about tissue microstructure because of its sensitivity to immobile macromolecular protons, which are invisible by conventional MRI. Over past years, there has been a growing interest in advanced methods for quantitative characterization of the MT effect. Such methods are intended to generate quantitative maps of molecular parameters describing the MT effect within the two-pool model. Promising biological findings were reported for the bound pool fraction (the key parameter of two-pool model), which provides strong associations with myelin content in neural tissues. This work describes recent development in quantitative magnetization transfer (qMT) imaging to correct the biases in cross-

relaxation imaging (CRI), one of qMT methods, due to unaccounted biexponential behavior of the longitudinal relaxation of water protons. Furthermore, this work introduces the new three-pool MT model to minimize the partial volume effects of non-exchanging component (i.e. CSF) in qMT measurements. These new methods are validated through simulation, phantom experiment, animal model, and human subject and stability of these techniques is investigated. The research in this dissertation provided the foundation for continued development and translation of new biomarker for macromolecular content in tissue (i.e. myelin content in nervous system and collagen matrix in cartilage) and can assist in early detection and quantitative staging of diseases caused by loss of macromolecules in tissues (i.e. multiple sclerosis and osteoarthritis).

Table of Contents

Acknowledgements

I would like to express my deepest appreciation for my faculty advisor Dr. Aaron Field; his trust in my intellectual capacity from the outset paved the path for my future endeavors. The very first year of my PhD program Dr. Field gave me the opportunity through the joint BME-Radiology fellowship, and with it he sparked my interest and fostered my career in medical imaging. Above all, he has provided me with constant encouragement and support in so many ways throughout my graduate studies; he made it possible for me to participate in different research studies. His intuition and passion for science and medicine inspired and enriched my growth as a student, a researcher, and the scientist that I aspire to be. I am forever indebted to him for his support.

I would like to express my sincere gratitude to my project advisor, Dr. Alexey Samsonov, for his immense guidance, thoughtful criticisms, and support, in addition to his exceptional mentoring throughout my dissertation projects. I have been very fortunate to have an advisor who gave me the freedom to explore; at the same time the guidance to recover when my steps faltered. During the past three years, he has taught me how to express ideas in a clear and simple manner for the purpose of simply communicating with other, writing scientific papers, or giving oral presentations. I have learned a great deal from him; and will never forget the valuable lessons he has taught me through the years. I am very thankful for his support and guidance.

I am truly grateful to my faculty advisor Dr. Andrew Alexander, for his continues support and guidance throughout my graduate studies. Our valuable discussions have helped me to better understand my research area. His advice and encouragements after each meeting motivated me to

pursue my research with even more determination. His insightful comments and constructive criticisms at different stages of my research were thought provoking, and have helped me focus my ideas and my efforts. He has taught me how to question thoughts, and how to critically evaluate various approaches. This work would not be possible without his constructive feedbacks and supervision. I owe him my deepest appreciation.

I would like to thank my academic advisor Dr. Walter Block, for his support and presence from the very beginning. Dr. Block has helped me with course selections all the way through evaluation of my dissertation research. He has been always there to listen and give advice. I am truly thankful for his support.

I am also thankful to Dr. Elizabeth Meyerand, the Chair of the Biomedical Engineering Department, for attending the committee meetings and evaluating my research. Without the assistance of my committee members the work presented in the dissertation would not have been possible.

The acknowledgment is not complete without the recognition of my family. Words fail me to express my appreciation to my parents, Shahnaz and Mohammad, and my uncle, Bozorgmehr, who deserve a very special mention for their constant encouragement, support, and their unconditional love. I am also grateful to my wonderful sister, Sara, and my brother, Sina, for their love and confidence in me.

Finally, I would like to express my appreciation to the University of Wisconsin, Department of Biomedical Engineering, and the University of Wisconsin School of Medicine and Public Health, Departments of Medical Physics and Radiology, for providing such an invaluable opportunity, excellent education, and training to the graduate students.

Introduction

Magnetic resonance imaging (MRI) is a medical imaging modality that produces images of soft tissues and metabolic processes in the human body. While contrast in conventional MRI is generated by protons with free mobility, magnetization transfer (MT) imaging is commonly recognized as a source of essential information about tissue microstructure because of its sensitivity to immobile macromolecular protons, which are invisible by conventional MRI (e.g., those associated with proteins and lipid bilayers of myelin, collagen matrix in cartilage, etc.) (1).

Several studies have shown that conventional MT imaging methods (i.e. MT ratio) are sensitive to the macromolecular content (i.e. lipid bilayers of myelin) and they have suggested these methods to study diseases caused by loss of macromolecules in tissue. Unfortunately, the parameters of such methods are not specific to different tissue abnormalities as they can be influenced by overall water and macromolecule content in tissues. Furthermore, these parameters are sensitive to the sequence parameters and B_0 and B_1 inhomogeneities. Therefore, over past years, there has been a growing interest in advanced methods for quantitative characterization of the MT effect (1-12). Such methods are intended to generate quantitative maps of molecular parameters describing the MT effect within the two-pool model (1). The key parameters of interest in this model are associated with the state of macromolecular protons, which is characterized by their molar fraction (bound pool fraction, f), the rate constant describing cross-relaxation with water protons (k), and the transverse relaxation time of free and bound pools (T_2^F and T_2^B). Particularly promising biological findings were reported for the bound pool fraction, which provides strong associations with myelin content in neural tissues (13-16) and was shown to allow tracking age-related changes of WM myelination in animal

studies (17). The first two chapters of this dissertation introduces the basics of magnetic resonance imaging (MRI) and the principles of magnetization transfer (MT) imaging; also different MT methods such MT-ratio (*MTR*), MT-saturation (*MT-Sat*), and quantitative magnetization transfer will be introduced.

The estimation of quantitative magnetization transfer (qMT) imaging is not straightforward. Numerical or analytical modeling of magnetization effect and non-linear fitting of measured data are required to estimate these parameters. For the last few years, my research has been focused on investigating the magnetization transfer effect, developing qMT imaging techniques, and applying qMT methods on both human and animal studies, which are included in this dissertation.

Chapter 3 introduced the modified cross-relaxation imaging (mCRI) which corrects the biases in cross-relaxation imaging (CRI) due to unaccounted biexponential behavior of the longitudinal relaxation of water protons. Chapter 4 describes a new method for fast and accurate bound pool fraction (f) and longitudinal relaxation time (T_1) mapping within the two-pool MT model. In chapter 5, the new three-pool MT model will be introduced to minimize the partial volume effects of non-exchanging component (i.e. CSF) in qMT measurements, the accuracy and precision of this model to the two-pool model will be compared through numerical simulation, phantom experiment, and in vivo study. Chapter 6 presents the applications of MT imaging in animal study and human study to elucidate the sensitivity and specificity of qMT imaging to macromolecule such as myelin and collagen. Chapter 7 summarizes the contribution of this dissertation in quantitative magnetization transfer imaging and suggests future work and directions that could promote clinical implementation of this work.

List of Tables

List of Figures

Chapter 4

Chapter 5

Chapter 1: The Basics of Magnetic Resonance Imaging

1.1 Introduction

Magnetic resonance imaging (MRI) is a medical imaging modality to produce images of soft tissues and metabolic processes in the human body. MRI is based on the principles of nuclear magnetic resonance (NMR), a phenomenon that occurs when nuclei of certain atoms are placed in a static magnetic field and experience a second oscillating magnetic field. Generally, all nuclei with an odd number of neutrons, protons, or both possess a net angular momentum (spin) and they are NMR active. Hydrogen (^{1}H) nucleus in water molecules is composed of a single proton (½ nuclear spin) and is abundant in the body, therefore it is the most widely imaged nucleus in MRI experiments.

1.2 Magnetic Dipole Moment and Larmor Frequency

A nucleus with a non-zero spin creates a circulating electric current and magnetic field around itself whose strength can be described as a magnetic dipole moment ($\vec{\mu}$). The magnetic dipole moment ($\vec{\mu}$) is directly proportional to spin angular momentum ($\vec{J}$) by the proportionality constant called gyromagnetic ratio (γ), which depends on the nucleus. The gyromagnetic ratio of proton is 2.675×10^8 *rad/s/T*.

$$\vec{\mu} = \gamma \vec{J} \qquad [1.1]$$

The direction of magnetic $\vec{\mu}$ is completely random in the absence of an external magnetic field due to thermal random motion. According to classical mechanics, if a spin with a magnetic dipole moment $\vec{\mu}$ is placed in an external magnetic field $\overrightarrow{B_0}$ it experiences a torque, which is equal to the rate of change of its angular momentum.

$$\frac{d\vec{J}}{dt} = \vec{\mu} \times \overrightarrow{B_0} \quad [1.2]$$

Since $\vec{\mu} = \gamma\vec{J}$, we have

$$\frac{d\vec{\mu}}{dt} = \gamma\vec{\mu} \times \overrightarrow{B_0} \quad [1.3]$$

This equation of motion characterizes the fundamental precession for a spin in an external magnetic field and it is a simple version of Bloch equation (figure 1.1).

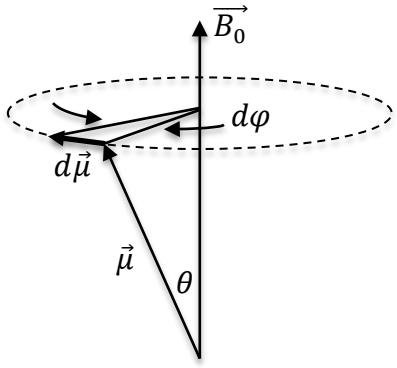

Figure 1.1: Precession of a proton's spin about a magnetic field

From figure 1.1, the differential changes in magnetic dipole moment is

$$|d\vec{\mu}| = \mu \sin\theta \, |d\varphi| \quad [1.4]$$

Also from equation 1.3 we have $|d\vec{\mu}| = \gamma\left|\vec{\mu} \times \overrightarrow{B_0}\right| dt = \gamma\mu B_0 \sin\theta \, dt$, therefore we can define the precession angular frequency, Larmor frequency, as

$$\omega_0 = \left|\frac{d\varphi}{dt}\right| = \gamma B_0 \quad [1.5]$$

1.3 Spin Alignment and Bulk Magnetization

The macroscopic magnetization vector ($\vec{M}$) is defined as the vector sum of all microscopic magnetic dipole moments in the object. In the absence of an external magnetic field, the direction of magnetic dipole moment is completely random so $\vec{M} = 0$. In the presence of an external magnetic field $\overrightarrow{B_0}$, all magnetic dipole moments are either lined up parallel to $\overrightarrow{B_0}$ (lower energy) or anti-parallel to $\overrightarrow{B_0}$ (higher energy). Based on Zeeman splitting phenomenon, the energy difference between these two spin states is given by

$$\Delta E = \gamma \hbar B_0 \qquad [1.6]$$

Where $\hbar = h/(2\pi)$ in terms of Planck's constant h. According to Boltzmann relationship the spin excess on lower energy state can be given by

$$\text{Spin excess} \approx N \frac{\gamma \hbar B_0}{2KT} \qquad [1.7]$$

Where *N* is the total number of spins presented in the object, *K* is Boltzmann constant, and *T* is absolute temperature of the spin system. The spin excess is very small and it is only 10 in a million spins for a magnetic field strength of 3T, but it generates detectable net magnetization $\vec{M}$ due to large population of spins in the system.

1.4 Resonance Condition and RF Excitation

In order to detect the MRI signal, the magnetization vector must be tipped away from $\overrightarrow{B_0}$ direction by applying a radiofrequency (RF) pulse. This RF pulse is produced by another magnetic field ($\overrightarrow{B_1}$) with relatively small field strength for a short time interval. Under resonance

condition ($\omega_{RF} = \omega_0$), the B_1 field is maximally synchronized to the tip the spin around its axis. A B_1 field is applied for a short time interval (τ) to rotate the spins around its axis, and the angle of rotation (α) is determined by

$$\alpha = \gamma B_1 \tau \quad [1.8]$$

1.5 The Bloch Equation and Relaxation

The time-dependent behavior of $\vec{M}$ in the presence of $\overrightarrow{B_1}(t)$ field is described by the Bloch equation:

$$\frac{d\vec{M}}{dt} = \gamma \vec{M} \times \vec{B}_{ext} + \frac{1}{T_1}(M_0 - M_z)\vec{k} - \frac{1}{T_2}\vec{M}_{xy} \quad [1.9]$$

In which $\vec{B}_{ext} = \vec{B}_0 + \vec{B}_1$. Equation 1.9 can be written in a rotating frame, a coordinate system whose transverse plane is rotating clockwise at the Larmor precession frequency with orthogonal axes of x', y', and z', as:

$$\frac{dM_{x'}}{dt} = \Delta\omega M_{y'} - \frac{M_{x'}}{T_2} \quad [1.10]$$

$$\frac{dM_{y'}}{dt} = -\Delta\omega M_{x'} + \omega_1 M_{z'} - \frac{M_{y'}}{T_2} \quad [1.11]$$

$$\frac{dM_{z'}}{dt} = -\omega_1 M_{y'} - \frac{M_{z'} - M_0}{T_1} \quad [1.12]$$

Where $\Delta\omega = \omega_0 - \omega$, ω_0 is the Larmor frequency, ω_1 is the spin frequency due to RF field, ω is the RF frequency of oscillation; T_1 and T_2 are longitudinal and transverse relaxation time constants respectively.

When an RF pulse is applied to the spin system the magnetization is perturbed from its equilibrium, and if this external force is removed from the system magnetization will return back to its equilibrium state. The recovery of the longitudinal magnetization (M_z) is called longitudinal relaxation; and the destruction of the transverse magnetization (M_{xy}) is called transverse relaxation. The longitudinal and transverse relaxation are described by first-order process:

$$\frac{dM_{z'}}{dt} = -\frac{M_{z'} - M_0}{T_1} \quad [1.13]$$

$$\frac{dM_{x'y'}}{dt} = -\frac{M_{x'y'}}{T_2} \quad [1.14]$$

The time evolution of the longitudinal and transverse magnetization can be obtained by solving the above equations and illustrated in figure 1.2:

$$M_{z'}(t) = M_0(1 - e^{-t/T_1}) + M_{z'}(0_+)e^{-t/T_1} \quad [1.15]$$

$$M_{x'y'}(t) = M_{x'y'}(0_+)e^{-t/T_2} \quad [1.16]$$

$M_{z'}(0_+)$ and $M_{x'y'}(0_+)$ are the longitudinal and transverse magnetization immediately after RF pulse.

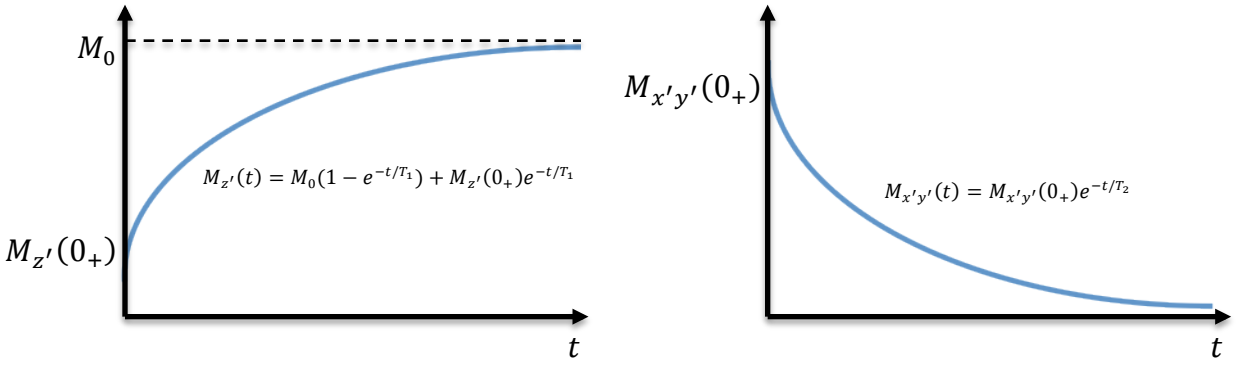

Figure 1.2: The regrowth of the longitudinal magnetization and the decay of transverse magnetization.

T_1 is called spin-lattice relaxation time, which shows regrowth of longitudinal magnetization due to the proton interaction with the lattice. The value of relaxation time T_1 depends of the tissue characteristics (tumbling rate) and the strength of the main magnetic field, i.e. the typical range of T_1 values for white matter and gray matter at 3.0T are 1000-1100 ms and 1700-1900 ms, respectively (18).

The decay of transverse magnetization is characterized by T_2, which is called spin-spin relaxation time. The local field that spins experience is combinations of the main magnetic field and the fields produced by neighbor spins. The variation in the local fields leads to different local precession frequencies of spins and causes dephasing of spins. Therefore, T_2 value depends on time spent in vicinity of nuclear neighbors and it is independent of the strength of the main magnetic field; more time near same neighbors causes shorter T_2. The typical range of T_2 values for white matter and gray matter are 65-75 ms and 90-105 ms, respectively (18).

In practice, there is an additional dephasing of the transverse magnetization caused by the external field inhomogeneities, which is characterized by T_2' decay. Therefore, the total transverse magnetization decay can be characterized by T_2^*, which is defined by

$$\frac{1}{T_2^*} = \frac{1}{T_2} + \frac{1}{T_2'} \qquad [1.17]$$

1.6 MRI System, Image Formation, and Image Contrast

An MRI scanner is composed of three major components: the main magnetic field, the RF system (transmitter and receiver), and the gradient system. As mention before, the primary function of the main magnetic field is to generate a strong uniform static field (B_0). The RF system consists of a transmitter coil to generate a rotating magnetic field (B_1) for excitation of spin system, and a receiver coil to convert the precessing magnetization into an electrical signal. The gradient system consists of three orthogonal gradient coils to localize the signal by generating spatially varying magnetic field so the spins at different location precess at different frequencies with different phases unique to their location. The measured signal is then reconstructed by Fourier transform to produce the image of the volume.

Conventional MRI methods (T_1-weighted, T_2-weighted, and *PD*-weighted) utilize the fact that different tissues have different T_1, T_2, and proton density (*PD*) to provide image contrast between tissues by setting the parameters of MRI scan such as repetition time (*TR*), echo time (*TE*), excitation flip angle (α), etc. There are other MRI methods that use different contrast mechanism to provide unique information about tissues, such magnetization transfer (MT) (19-21), diffusion MRI (22-28), multicomponent relaxometry (29-35), functional MRI (fMRI) (36,37), and MR angiography (MRA) (38-42). Among these advanced MRI methods, magnetization transfer imaging (MTI) is a novel method that shows promising results in assessing the information about macromolecule content in tissues, and it is the focus of this dissertation.

Chapter 2: Introduction to Magnetization Transfer Imaging

2.1 Introduction

MRI can detect signal only from mobile protons (free water protons) that have sufficiently long T_2 relaxation times (in the range of ms). Less mobile protons (i.e. protons bound to macromolecules) have very short T_2 relaxation times (in the range of μs) to be detected by traditional MRI because their signal has completely decayed before encoding. However, dipolar coupling and chemical exchange facilitate an exchange of magnetization between these two pools of protons (free water protons and protons bound to macromolecules). This mechanism is known as magnetization transfer (figure 2.1)(19-21).

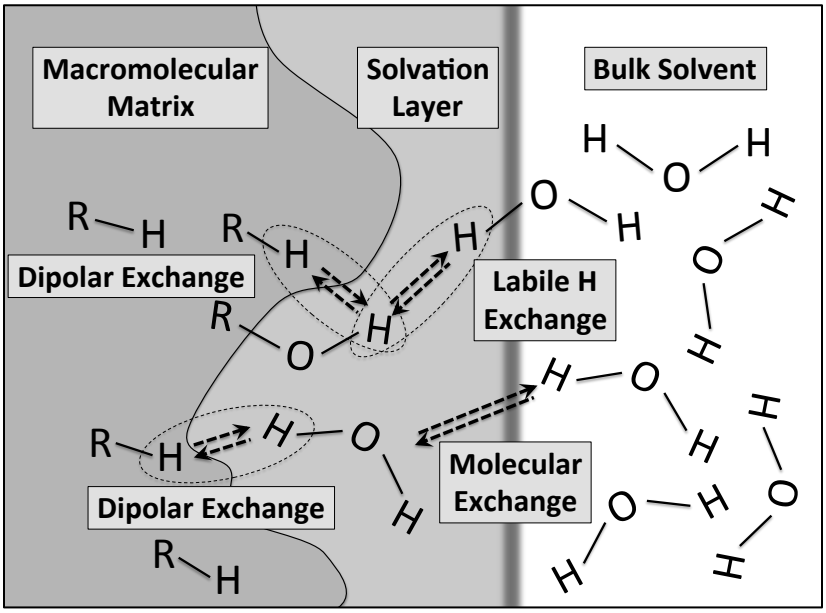

Figure 2.1: Schematic of proton populations and magnetization transfer pathways between different proton pools (21).

2.2 Principles of Magnetization Transfer

While conventional MRI generates contrast by protons with free mobility, magnetization transfer imaging generates contrast from protons bound to macromolecules. Magnetization transfer (MT) imaging is based on the exchange of magnetization between free pool and bound

pool in biological tissues. The protons from the bound pool are strongly coupled resulting in a very broad absorption lineshape (frequency spectrum), while free water protons have very narrow frequency spectrum (the bandwidth is inversely proportional to T_2). It is possible to saturate the bound pool and leave free pool relatively intact by applying a strong off-resonance RF pulse at a frequency far from the free water resonance frequency. This saturation of bound pool magnetization can be transferred to free pool magnetization causing a decrease in the detected signal from free pool (Figure 2.2). While off-resonance RF pulse is typically used in MT approaches, on-resonance RF pulse or in fact any RF pulse that has different effects on each pool will induce MT. Later in this dissertation, we will show the importance of considering two-pool model even for on-resonance pulses.

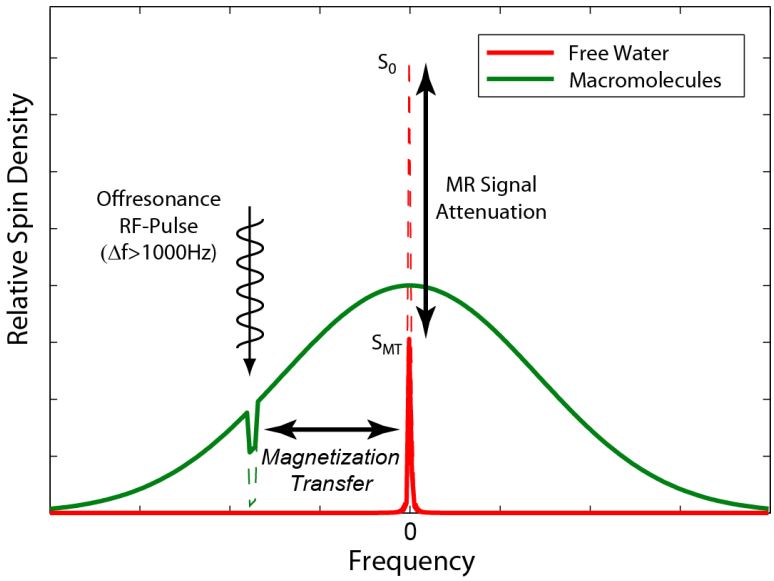

Figure 2.2: Schematic of the MT saturation process. Off-resonance RF pulse saturates the magnetization of the bound pool. Magnetization transfer between two pools attenuates the free water signal.

Most MT imaging methods are based on two-pool MT model (Figure 2.3), which considers that protons are either from free water (free pool) or from protons bound to the macromolecules (bound pool).

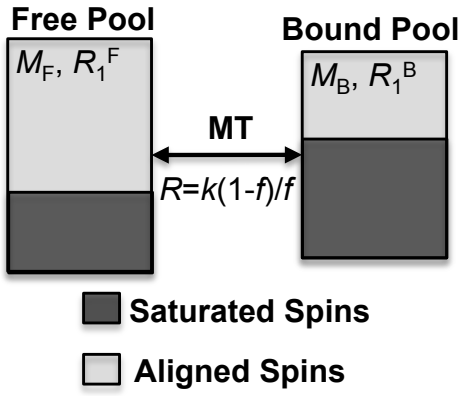

Figure 2.3: A two-pool MT model. M and R_1 are magnetization and longitudinal relaxation of each pool; R is magnetization transfer exchange between two pools (1).

Right after each RF pulse, some of the spins in each pool are in the longitudinal orientation (aligned spins) and some are saturated (saturated spins). The time-dependent changes of the magnetization of each pool is given by different rate constants: $R_1^{F,B} = 1/T_1^{F,B}$ are the longitudinal relaxation rates of each pool, R is the exchange rate from free pool to bound pool, and k is the exchange rate from bound pool to free pool. The MT exchange between two pools depends on the relative magnetization of each pool and the rate of the exchange between these pools. At equilibrium, we have the same amount of magnetization transferring from each pool to the other, therefore:

$$R \times f = k \times (1 - f) \qquad [1.2]$$

where *f* is the fraction of bound spins relative to the total spin:

$$f = \frac{M_B}{M_F + M_B} \quad [2.2]$$

The model of MT exchange for a two-pool system has been proposed by (43) and can be written as:

$$\frac{dM_x^F}{dt} = -\frac{M_x^F}{T_2^F} - 2\pi\Delta M_y^F \quad [2.3]$$

$$\frac{dM_y^F}{dt} = -\frac{M_y^F}{T_2^F} + 2\pi\Delta M_x^F - \gamma B_1(t) M_z^F \quad [2.4]$$

$$\frac{dM_z^F}{dt} = \gamma B_1(t) M_y^F - (R_1^F + k) M_z^F + k(1-f)/f M_z^B + R_1^F(1-f) \quad [2.5]$$

$$\frac{dM_z^B}{dt} = -(R_1^B + k(1-f)/f + \pi\gamma^2 B_1^2(t) g(\Delta, T_2^B)) M_z^B + k M_z^F + R_1^B f \quad [2.6]$$

where $M_{x,y,z}^{F,B}$ are the *x*, *y*, and *z*-components of magnetization of the free (*F*) and bound (*B*) pools; Δ and $B_1(t)$ are the frequency and the amplitude of the RF pulse; $g(\Delta, T_2^B)$ is the absorption lineshape, which is the function of the frequency of RF pulse and transverse relaxation time constant of the bound pool (T_2^B), and it is assumed by a Super-Lorentzian function for a biological tissues (2,3,44,45).

$$g(\Delta, T_2^B) = \sqrt{\frac{2}{\pi}} \int_0^{\frac{\pi}{2}} \frac{T_2^B}{|3\cos^2\theta - 1|} \exp\left(-2\left(\frac{2\pi\Delta T_2^B}{3\cos^2\theta - 1}\right)^2\right) \sin\theta \, d\theta \quad [2.7]$$

2.3 Magnetization Transfer Imaging Techniques

There are several methods using MT effect to generate a contrast and assess the macromolecular content in different tissues, and in general they use MT saturation pulse to selectively saturate the magnetization of protons bound to macromolecule and the magnetization of the free pool protons is indirectly affected by the saturation of bound pool protons. As a part of this dissertation, we describe several methods using MT effect such as magnetization transfer ratio (*MTR*), magnetization transfer saturation (*MT-Sat*), and quantitative magnetization transfer (qMT) imaging.

2.4 Magnetization Transfer Ratio (*MTR*)

The most common approach using MT effect is MT ratio (*MTR*) (46) , calculated as the relative change in intensity of images acquired without (S_0) and with (S_{MT}) MT pulses:

$$MTR = \frac{S_0 - S_{MT}}{S_0} \qquad [2.8]$$

Figure 2.4 shows an example of images from *MTR* experiment and obtained images with and without MT saturation pulse. The higher *MTR* in white matter (WM) is associated with the proteins and lipids associated with myelinated axons (47).

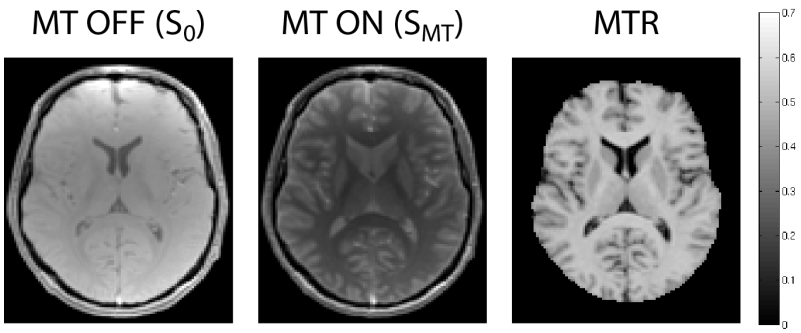

Figure 2.4. Example images of *MTR* and obtained images with and without MT pulse .

MTR has been shown to be proportional to the product of bound pool fraction (*f*) and observed T_1 of the free pool (T_1^{obs}) (48). Yarnykh (3) expressed *MTR* from the approximated analytical model of pulsed MT as

$$MTR \approx \frac{sW^B}{P + QsW^B} \quad [2.9]$$

where $s = t_m/TR$ is the duty cycle of the sequence given as ratio of time interval of MT pulse (t_m) to the repetition time (*TR*); $W^B = \pi\gamma^2 B_1^2(t) g(\Delta, T_2^B)$ is the average saturation rate for the bound pool given; *P* and *Q* are independent of the properties of a saturation RF field and are function of observed R_1 of the free pool ($R_1^{obs} = 1/T_1^{obs}$), bound pool fraction (*f*), cross-relaxation rate (*k*), sequence parameters such as repetition time (*TR*) and excitation flip angle (α)

$$P \approx \left(R_1^{obs} - \frac{(1-f)(\ln\cos\alpha)}{TR} \right) f^{-1} \quad [2.10]$$

$$Q \approx \left(R_1^{obs} - \frac{(\ln\cos\alpha)}{TR} \right) k^{-1} + 1 \quad [2.11]$$

Although the *MTR* measurement is sensitive to macromolecular content of tissue it is highly dependent on pulse sequence parameters, magnetic field strength, B_0 and B_1 inhomogeneity, as well as shape, amplitude, and offset frequency of MT pulse; these factors causes variability of *MTR* measurements across scanners, coils, and scanned objects. Yarnykh (49) has proposed a analytical method to correct B_1 errors in *MTR* experiment using an external B_1 mapping. Using the first-order approximation equation [2.9] can be written as

$$MTR \approx \frac{kfsW^B}{k\left(R_1 - \frac{(1-f)\ln\cos(\alpha)}{TR}\right) + fsW^B(R_1 + k - \frac{\ln\cos(\alpha)}{TR})} \quad [2.12]$$

and B_1 corrected MTR can be written as

$$MTR_{cor} = \frac{A(c)B(c)MTR_{obs}}{1-(1-A(c)B(c))MTR_{obs}} \quad [2.13]$$

Where

$$A(c) = \frac{R\times TR + c^2 t_m W^B}{c^2(R\times TR + t_m W^B)} \quad [2.14]$$

$$B(c) = \frac{R_1\times TR - \ln\cos(c\alpha)}{R_1\times TR - \ln\cos(\alpha)} \quad [2.15]$$

and $c = B_1/B_{1nom}$ is the scaling coefficient of B_1 measured by any B_1 mapping sequence. Figure 2.5 shows the effect of B_1 correction on *MTR* map, which shows more uniform *MTR* map after B_1 correction (50).

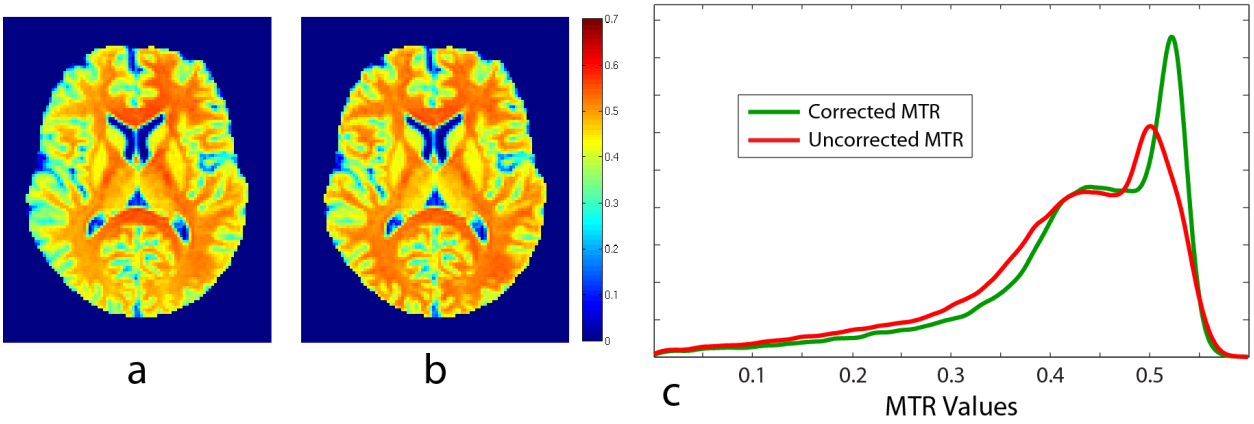

Figure 2.5. Effect of B_1 inhomogeneity on *MTR*. Uncorrected *MTR* map **(a)** demonstrates by slow spatially varying intensity inhomogeneity **(a)**. Correction of *MTR* using separately acquired B_1 map eliminates the intensity bias **(b)** and leads to improved localization of WM and GM peaks on the corresponding whole brain histograms **(c)**.

2.5 Magnetization Transfer Saturation (*MT-Sat*)

MT-Sat method was proposed by in 2008 (51), where the empirical signal equation for a spoiled gradient echo sequence (SPGR) with MT pulse saturation was derived. This equation is based on a biexponential time course including T_1 relaxation and MT saturation. *MT-Sat* map (δ_{app}) can be derived from three datasets of MT-weighted, *PD*-weighted, and T_1-weighted SPGR sequence from following equations:

$$\delta_{\mathrm{app}} = \left(\frac{A_{\mathrm{app}}\alpha_{\mathrm{MT}}}{S_{\mathrm{MT}}} - 1\right) R_{1\mathrm{app}} TR - \frac{\alpha_{\mathrm{MT}}^2}{2} \quad [2.16]$$

$$A_{\mathrm{app}} = S_{\mathrm{PD}} S_{\mathrm{T}_1} \frac{TR_{\mathrm{PD}}\alpha_{\mathrm{T}_1}/\alpha_{\mathrm{PD}} - TR_{\mathrm{T}_1}\alpha_{\mathrm{PD}}/\alpha_{\mathrm{T}_1}}{S_{\mathrm{T}_1} TR_{\mathrm{PD}}\alpha_{\mathrm{T}_1} - S_{\mathrm{PD}} TR_{\mathrm{T}_1}\alpha_{\mathrm{PD}}} \quad [2.17]$$

$$R_{1\mathrm{app}} = \frac{1}{2} \frac{S_{\mathrm{T}_1}\alpha_{\mathrm{T}_1}/TR_{\mathrm{T}_1} - S_{\mathrm{PD}}\alpha_{\mathrm{PD}}/TR_{\mathrm{PD}}}{S_{\mathrm{PD}}/\alpha_{\mathrm{PD}} - S_{\mathrm{T}_1}/\alpha_{\mathrm{T}_1}} \quad [2.18]$$

where S is the signal, α is the excitation flip angle, TR is the repetition, subscripts MT, *PD*, T_1 label different datasets, and subscript app is the apparent parameters without flip angle correction. The major advantage of *MT-Sat* is that inhomogeneities of the receiver coil and the transmitted RF field are inherently accounted for. Figure 2.6 shows an example of *MT-Sat* map.

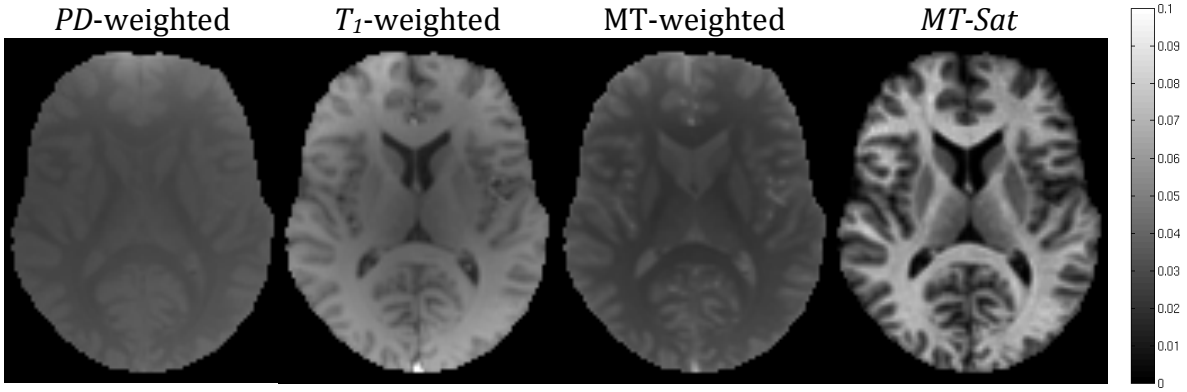

Figure 2.6. Example of *MT-Sat* map and obtained *PD*-weighted, T_1-weighted, and MT-weighted SPGR.

2.6 Quantitative Magnetization Transfer (qMT) Imaging

Several studies have shown that *MTR* and *MT-Sat* are sensitive to the macromolecular content and they have suggested these methods to study diseases caused by loss of macromolecules in tissue. Although loss of macromolecules in tissue causes reduction of these parameters, other factors such as overall water and macromolecule contents, and other pathology (edema, inflammation, axonal loss, and etc.) can affect these parameters. Therefore, these parameters are not specific to different tissue abnormalities as they can be influenced by overall water and macromolecule content in tissues (52). Furthermore, these parameters (specially *MTR*) are sensitive to the sequence parameters and B_0 and B_1 inhomogeneities so fully quantitative MT (qMT) methods are required to improve sensitivity, specificity, and stability of MT parameters. Several methods have been proposed to quantify the MT parameters of the two-pool model (1-12). The key parameters of interest in this model are associated with the state of macromolecular protons, which is characterized by their molar fraction (*f*), the forward rate constant describing cross-relaxation with water protons (*k*), and transverse relaxation time T_2^B.

Cross-relaxation imaging (CRI) (7) is one of qMT methods, which maps the fundamental parameters (*f*, *k*, and T_2^B) determining MT effect in tissues. The theory of pulsed MT effect on the two-pool MT model has been described previously (3,7,53). In summary, the vector of longitudinal steady state magnetizations of the SPGR acquisition in the presence of an off-resonance saturation radio frequency (RF) pulse can be shown in the following matrix format:

$$\mathbf{M_z} = (\mathbf{I} - \mathbf{E_s}\mathbf{E_m}\mathbf{E_r}\mathbf{C})^{-1}([\mathbf{E_s}\mathbf{E_m}(\mathbf{I} - \mathbf{E_r}) + (\mathbf{I} - \mathbf{E_s})]\mathbf{M_{eq}} + \mathbf{E_s}(\mathbf{I} - \mathbf{E_m})\mathbf{M_{ss}}) \qquad [2.19]$$

where $\mathbf{M_z} = [M_z^F \;\; M_z^B]^T$, M_z^F, M_z^B are longitudinal magnetizations of free and bound protons, respectively; $\mathbf{I}$ is the identity; $\mathbf{E_m} = \exp((\mathbf{R} + \mathbf{W})t_m)$ describes off-resonance saturation by the

pulse with duration t_m; $\mathbf{E_s} = \exp(\mathbf{R}t_s)$ and $\mathbf{E_r} = \exp(\mathbf{R}t_r)$ describe longitudinal relaxations during delays before (t_s) and after (t_r) the excitation pulse; $\mathbf{C} = \mathrm{diag}(S^f, S^b)$, where $S^f = \cos(\alpha)$, $S^b = 1$ describe the attenuation of longitudinal magnetizations of free and bound protons by the on-resonance excitation pulse with the flip angle α, respectively; $\mathbf{M_{eq}}$ and $\mathbf{M_{ss}}$ are the vectors of equilibrium and steady-state longitudinal magnetization, and **R** and **W** are matrices of longitudinal relaxation and saturation defined as follows:

$$\mathbf{M_{eq}} = \begin{bmatrix} 1-f \\ f \end{bmatrix} \qquad \mathbf{M_{ss}} = \frac{1}{D}\begin{bmatrix} (1-f)(A + R_1^F W^B) \\ f(A + R_1^B W^F) \end{bmatrix}$$
$$\mathbf{R} = \begin{bmatrix} -R_1^F - k & k(1-f)/f \\ k & -R_1^F - k(1-f)/f \end{bmatrix} \qquad \mathbf{W} = -\mathrm{diag}(W^F, W^B) \quad [2.20]$$

Where

$$A = R_1^F R_1^B + R_1^F(1-f)/f + R_1^B k \quad [2.21]$$

$$D = A + (R_1^F + k)W^B + (R_1^B + k(1-f)/f)W^F + W^B W^F \quad [2.22]$$

R_1^F and R_1^B are the longitudinal relaxation rate of free and bound spins, respectively; the effective saturation rates of the pools W^F and W^B are calculated from the absorption line-shapes of the pools $g^{F,B}(\Delta, T_2^{F,B})$ and the root-mean-square amplitude of saturation pulse ω_{1rms} averaged over the pulse duration as follows:

$$W^{F,B} = \pi\omega_{1rms}^2 g^{F,B}(\Delta, T_2^{F,B}) \quad [2.23]$$

where absorption line-shape of the free and bound pools $g^{F,B}(\Delta, T_2^{F,B})$ are defined by the Lorentzian and Super-Lorentzian (or Gaussian for non-biological sample) functions, respectively (figure 2.7) (54).

Lorentzian lineshape:

$$g(\Delta, T_2) = \frac{T_2}{\pi} \frac{1}{[1 + (2\pi\Delta T_2)^2]} \quad [2.24]$$

Super-Lorentzian lineshape:

$$g(\Delta, T_2) = \sqrt{\frac{2}{\pi}} \int_0^{\frac{\pi}{2}} \frac{T_2}{|3\cos^2\theta - 1|} \exp\left(-2\left(\frac{2\pi\Delta T_2}{3\cos^2\theta - 1}\right)^2\right) \sin\theta \, d\theta \quad [2.25]$$

Gaussian lineshape:

$$g(\Delta, T_2) = \frac{T_2}{\sqrt{2\pi}} \exp\left(\frac{-(2\pi\Delta T_2)^2}{2}\right) \quad [2.26]$$

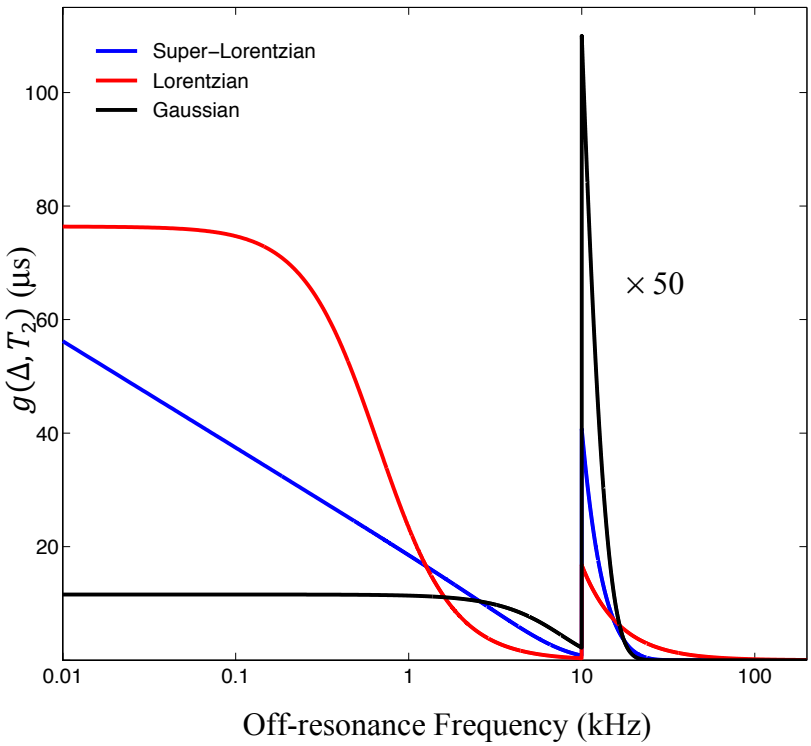

Figure 2.7. Lineshapes: Super-Lorentzian (T_2=17.7 μs), Lorentzian (T_2=17.7 μs), and Gaussian (T_2=29 μs). The lineshapes are 50 times magnified above 10kHz to better appreciate the differences (33).

The saturation rate of free pool at the offset frequencies much larger than the spectral line width of the free pool, $(2\pi\Delta T_2^F)^2 \gg 1$ (1,54), can be approximated by

$$W^F = (\omega_{1rms}/2\pi\Delta)^2/T_2^F \quad [2.27]$$

Estimating of T_2^F can be obtained using the fact that the product of $T_2^F R_1^F$ is pretty constant in brain tissues and it's approximately 0.022 at 3.0T.

$$W^F = (\omega_{1rms}/2\pi\Delta)^2 R_1^F/0.022 \quad [2.28]$$

where R_1^F can be estimated from the fact that the observed $R_1 = 1/T_1$, measured from variable flip angle (VFA) method is equal to the slow eigenvalue of matrix **R** (1):

$$R_1^F = R_1 - \frac{k(R_1^B - R_1)}{R_1^B - R_1 + k(1-f)/f} \quad [2.29]$$

and R_1^B cannot be experimentally measured but can be assumed as $R_1^B = 1$ (1,2,4,7,45,54). The reconstruction of parametric maps is performed in two steps (figure 2.8 (7)). During the first step, *PD* and R_1 maps are calculated by fitting VFA SPGR data the Ernst equation (55):

$$S_\alpha = PD\frac{1-\exp(-R_1 TR)}{1-\cos\alpha\exp(-R_1 TR)}\sin\alpha \quad [2.30]$$

In the second step, the matrix model of pulsed MT is fitted to MT-weighted data, while R_1 is supplied as an external parameter. Prior to fit, MT data are normalized pixel-wise by an arbitrary reference image typically obtained without saturation to reduce the number of free parameters in the fit by excluding *PD* or synthesized from *PD* and R_1 maps. The normalized

data are then fitted to the corresponding ratio of analytical signal expressions with and without saturation (S_{MT-ON}, S_{MT-OFF}):

$$S_{MT-ON} = PD \times M_z^F \sin\alpha \quad [2.31]$$

$$S_{MT-OFF} = PD \times M_z^F (W^B = 0, W^F = 0) \sin\alpha \quad [2.32]$$

where α is excitation flip angle and *PD* consists of the spin density, instrumental scaling, and the effect of T_2^* decay.

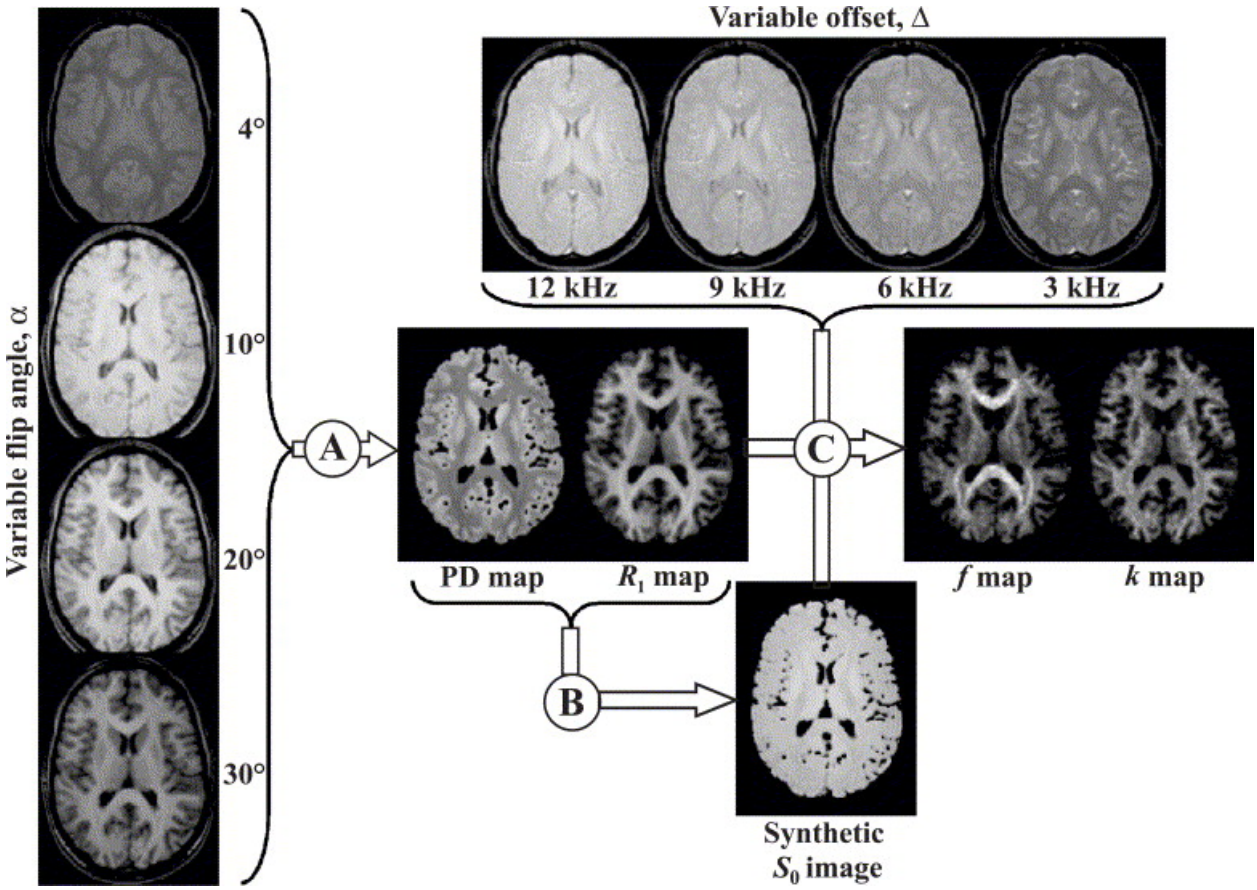

Figure 2.8. Cross-relaxation image processing scheme. In the step (A) *PD* and R_1 maps are generated from VFA data, in step (B) synthetic S_0 is computed from Ernst equation, and in the step (C) *f* and *k* maps are reconstructed from a set of MT-weighted data normalized to S_0. Adapted from (7).

2.7 Optimization Strategies for Accurate Quantitative MT Imaging

2.7.1 Introduction

Quantification of two-pool MT (qMT) model parameters (longitudinal relaxation rate R_1, bound pool fraction *f,* cross relaxation rate *k,* transverse relaxation times of the bound pool T_2^B, and free pool T_2^F) allows inferring useful information about MRI-invisible macromolecular tissue content such as myelin (2,6). Many qMT methods such as cross-relaxation imaging (CRI) and modified CRI (mCRI) (7,53) use efficient pulsed MT in steady state, however data acquisition time may be too long for clinical applications. One CRI acceleration approach is to exclude T_2^F from estimation by sampling high offset frequencies (Δ>2.5 kHz) where direct saturation of free water is minimized. Going from 1.5T, the system used in early qMT applications (2,6,7), to 3T may improve CRI by utilizing the field-dependent SNR increase (7). However, translation to 3T faces an increased specific absorption rate (SAR); the related decrease in highest attainable MT flip angle may lead to SNR loss in parametric maps. In this section we study the challenges of CRI at 3T and proposes several optimizations at both 1.5 and 3T field strengths.

2.7.2 Effect of Experiment Design

Two families of experiment designs were studied: 1) Standard CRI with higher Δ=2.5, 5, 9, 13 kHz (only R_1, *f,* *k,* T_2^B are estimated). 2) Extended design with additional optimized low Δ=0.8 kHz (T_2^F is also estimated). Data were synthesized for white matter for 18ms Fermi MT pulse with flip angles 500˚ (1.5T and 3T) and 1100˚(3T) /1600˚(1.5T) (maximal allowed values on our GE Signa 1.5T and MR750 3T for the given patient weight and coil type). Monte-Carlo simulations were performed to find noise level σ in qMT estimates (figure 2.9).

Efficiency was defined as $1/\sigma$ and did not include field dependent SNR gain. Using low Δ significantly improved estimation of CRI measures (especially *k*) despite dimensionality increase (T_2^F estimation).

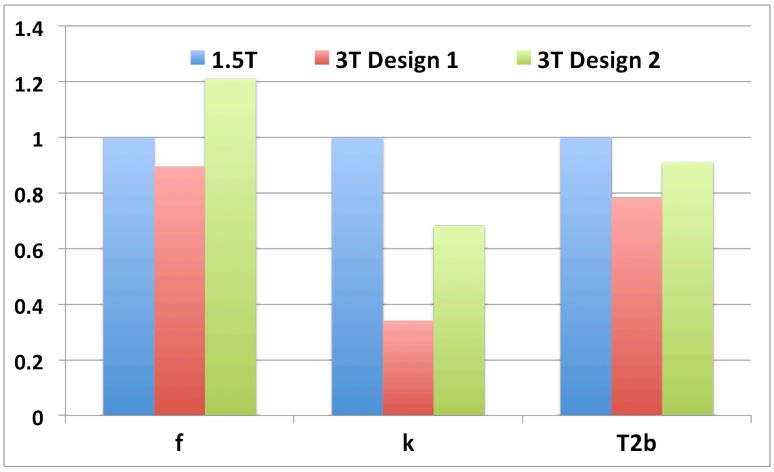

Figure 2.9: Relative efficiency of CRI parameter mapping at 3T using regular (#1) and extended (#2) designs (normalized to 1.5T values).

2.7.3 Effect of MT Pulse Shape

The effect of using MT pulses with low (Gaussian) and high (Fermi) SAR-efficiency (56) (figure 2.10) on the qMT mapping performance were examined for Design #2. The pulses had same duration and peak SAR. Fermi pulse was more SNR-efficient for parameter estimation than Gaussian pulse with most gain observed for *k* (Table 2.1).

Table 2.1: Efficiency of Fermi relative to that of Gaussian MT pulses ($\sigma_{gauss}/\sigma_{fermi}$).

R_1	f	k	T_2^B	T_2^F
1.0413	1.5820	2.9149	1.7558	1.9361

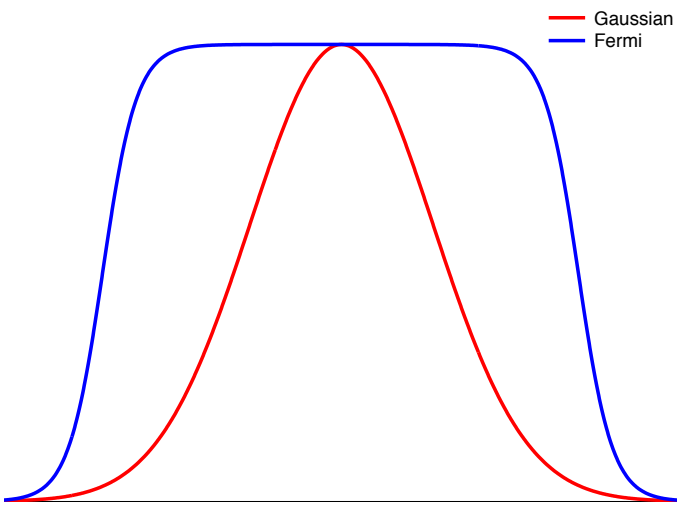

Figure 2.10: Fermi pulse and Gaussian pulse.

2.7.4 Effect of MT Pulse Bandwidth

Higher BW (shorter) Fermi pulse may cause large errors in qMT maps using low offset frequencies (Table 2.2). The standard approach is to use Lorentzian lineshape to model the effect of MT pulse on free pool.

Table 2.2: Percent of error in CRI parameters for different MT pulse widths (Design #2).

	R_1	f	k	T_2^B	T_2^F
8ms Fermi	-11.33	40.7	-48.7	18.23	-83.33
20ms Fermi	-0.01	-0.12	-3.24	-0.32	-31.72

The approach fails to adequately describe the behavior of free pool in the range<1kHz (figure 2.11). The deviation is due to Rabi oscillations arising in near-resonance excitation regime, the effect highly dependent on local B1 distribution not accounted for in realistic qMT models (57).

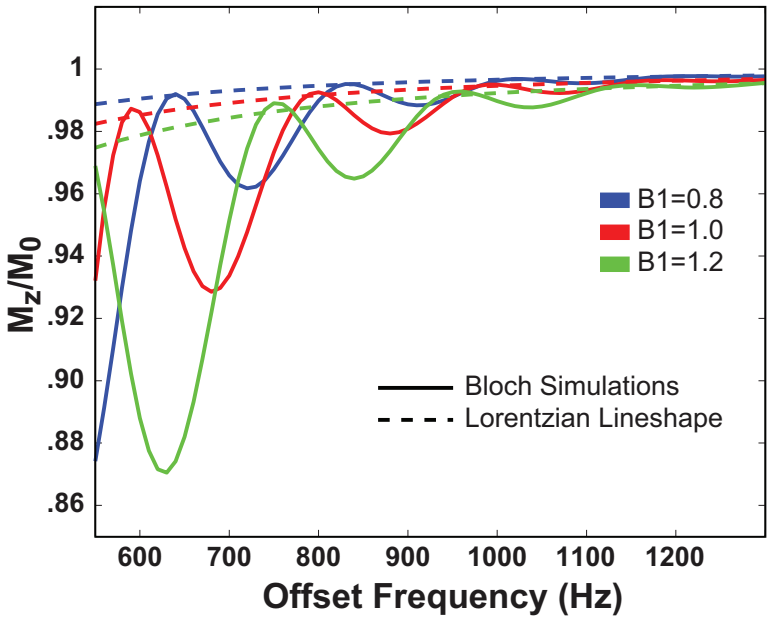

Figure 2.11: The Rabi oscillations make the standard Lorentzian lineshape approximation inadequate to model effect of higher BW pulse on free pool for low offset frequencies.

The MT signal is much more sensitive to changes in B_0 and B_1 for shorter pulse (figure 2.12). The effect is hard to account for in realistic qMT models (57) because it is highly dependent on local distribution of transmit field B_1 (figure 2.11 and 2.12). The accuracy loss for 20 ms pulse (narrower bandwidth) was much less for most measures (R_1, f, k, T_2^B) while still significant for T_2^F (Table 2.2).

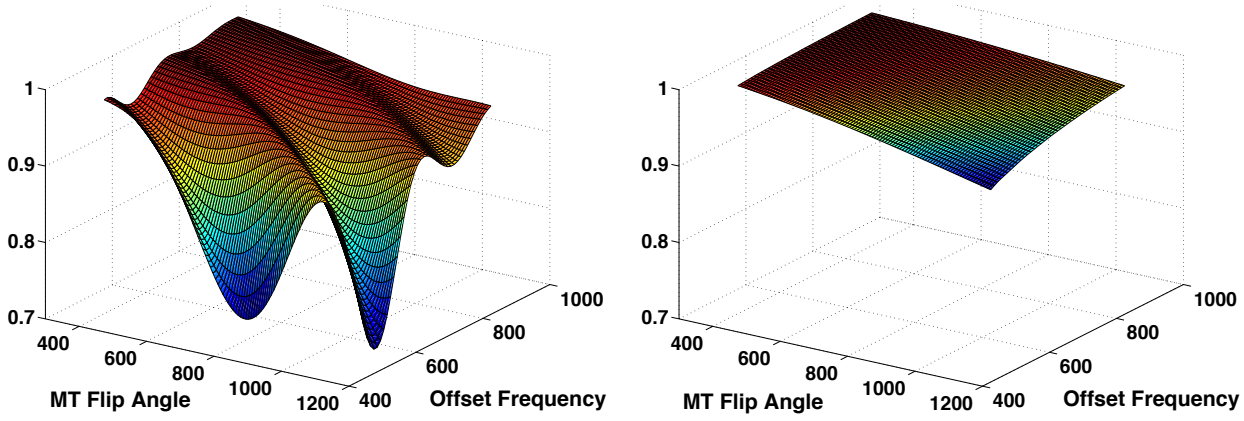

Figure 2.12: Normalized MT signal vs. offset frequency and MT flip angles for 8ms (left) and 20ms (right) MT pulse widths shows significant Rabi oscillations for higher BW pulse.

2.7.5 Phantom Results

MT weighted data of FBRIN phantom (http://www.birncommunity.org.) were acquired at offset frequencies 0.6 and 20kHz with 8ms Fermi MT pulse with flip angle 750˚. Range of offset frequency in the phantom was provided using shim gradients and measured using IDEAL (58). Flip angle map was measured by optimized AFI method (59). The 3D images of MT ratio (S_{MT}(0.6kHz)/S_{MT}(20kHz)) were plotted against local flip angle (~B_1) and B_0 values (figure 2.13). The observed oscillations were consistent with simulations for free water magnetization (figure 2.11 and 2.12) (full quantitative comparison between theoretical predication phantom data was not made because of additional MT effect in the agar phantom and uncertainties in B_1 field determination from actual flip angle values).

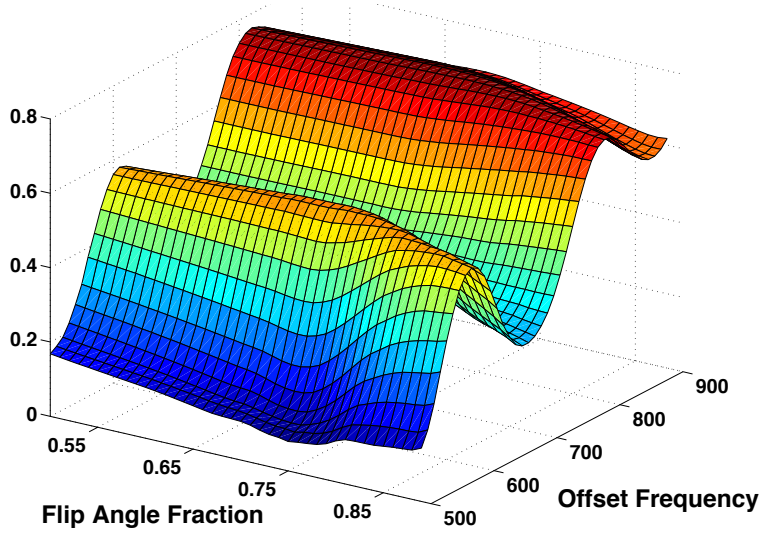

Figure 2.13: MT signal from FBRIN phantom for the range of Δ and $\alpha_{MT.}$ The observed oscillations were consistent with simulations for free water magnetization

2.7.6 Discussion

We studied several ways to optimize efficiency of CRI at both 1.5 and 3T. We showed (for 3T case) that the CRI efficiency might be improved by including extra sample(s) from low Δ range (<1 kHz). Further, we demonstrated that SAR-efficient pulses might provide additional large efficiency gains in CRI. At the same time, high bandwidth SAR-efficient pulses may lead to a significant error in qMT measures for the low offset frequency designs. One simple solution is to resort to longer SAR-efficient pulses. We found the reasonable tradeoff to be 16-20 ms Fermi pulses. Therefore, cross-relaxation imaging (CRI) and other related qMTI methods may be optimized to significantly improve their accuracy and efficiency.

Chapter 3: Analysis and Correction of Biases in Cross-Relaxation MRI Due to Biexponential Longitudinal Relaxation

3.1 Introduction

Magnetization transfer (MT) effect is commonly recognized as a source of important information about tissue microstructure due to its sensitivity to immobile macromolecular protons not detectable by the conventional MRI (e.g., those associated with proteins and lipid bilayers of myelin, collagen matrix in cartilage, muscle fibers, etc.) (1,19). Various approaches have been proposed to quantify the MT effect in-vivo including empirical indexes characterizing signal saturation due to MT (19,46,51) and methods for quantitative mapping of specific parameters describing MT within the two-pool model (1-12). The key parameters of interest in this model are associated with the state of macromolecular protons, which is characterized by their molar fraction (bound pool fraction, f), the forward rate constant describing cross-relaxation with water protons (k), and the transverse relaxation time T_2^B. Particularly promising findings were reported for the bound pool fraction, which was found to be correlated with the myelin content in neural tissues (13-16) and was shown to be capable of tracking age-related changes of the white matter (WM) myelination in animal studies (17).

One group of quantitative MT methods termed cross-relaxation imaging (CRI) (3,7,9) is specifically targeted at mapping the parameters f, k, and T_2^B or their subsets in the isolation from relaxation properties of the water proton magnetization. Collectively, these techniques rely on the approximate two-pool pulsed MT formalism (3,7) where the action of off-resonance saturation pulses on the macromolecular proton pool is described by an effective time-independent saturation rate calculated for a square pulse with the equivalent power and duration. Further, direct saturation of the free water proton pool is either neglected (3) or estimated within the stationary approximation sufficiently far from the resonance(7). These techniques allow 3D acquisition with clinically acceptable scan times and resolution based on a limited number of

MT-weighted images obtained with variable off-resonance saturation. The common feature of CRI and other off-resonance qMT techniques is the need for complementary T_1 mapping, which allows decoupling of the two-pool model parameters from the longitudinal relaxation rate $R_1=1/T_1$ (2-4,7,9). Because of the need for the fast 3D acquisition, T_1 maps are often generated using the variable flip angle (VFA) method with a spoiled gradient-echo (SPGR) sequence (55). It has been realized recently that the VFA method originally derived for the single-pool model inaccurately describes the SPGR signal, which often leads to biased R_1 estimation in tissues with rich macromolecular content. This bias is due to unaccounted cross-relaxation caused by magnetization transfer effect between macromolecular and water protons, which leads to the bi-exponential behavior of longitudinal relaxation of water proton magnetization in such tissues (60). The cross-relaxation contribution was shown to dominate R_1 of water in hydrated collagen (60) and more recently in neural tissues (61). Deviation of longitudinal relaxation from a single-exponential behavior due to cross-relaxation significantly affects signal intensities in the fast gradient-echo sequences (62,63) and introduces a bias in VFA R_1 measurements that depends on the pulse sequence parameters and may reach up to 14-15% in brain white matter (WM) (62).

Apart from biasing VFA R_1 estimation, systematic errors from unaccounted bi-exponential relaxation may further propagate into the two-pool model parameters estimated by quantitative MT techniques such as CRI. Conversely, an unbiased determination of R_1 values in tissues requires the knowledge about the rest of parameters of the two-pool model, which may not be practical for data correction within the VFA method alone (62). In this study, we propose the unified treatment of VFA and MT SPGR signals using a modified CRI analysis, which enables simultaneous corrections of R_1 and two-pool MT model parameters. In particular, we theoretically and experimentally characterize systematic errors in CRI caused by bi-exponential

relaxation in VFA R_1 mapping and demonstrate a new processing algorithm, which corrects for such errors and yields accurate parametric *f, k,* T_2^B, and R_1 maps. Additionally, we propose an analytical correction procedure allowing recalculation of previously obtained cross-relaxation parameter values with acceptable residual errors.

3.2 Theory

3.2.1 Analytical Theory of the SPGR Signal in the Presence of Cross-Relaxation

To estimate the effect of cross-relaxation on the apparent R_1 measured by the VFA method, we employ the previously described pulsed steady-state formalism (3,7) in the simplified form, where no off-resonance saturation is applied. The matrix model of the longitudinal magnetization (based on Eq. [3.1] in Ref. (7)) can be rewritten as:

$$\mathbf{M_z} = (\mathbf{I} - \mathbf{EC})^{-1}(\mathbf{I} - \mathbf{E})\mathbf{M_{eq}} \qquad [3.1]$$

Where $\mathbf{M_z} = [M_z^F \;\; M_z^B]^T$ corresponds to the longitudinal magnetization before the excitation pulse, M_z^F, M_z^B are the longitudinal magnetizations of free and bound protons, respectively, $\mathbf{M_{eq}} = \mathbf{M_0}[1-f \quad f]^T$ is the vector of equilibrium magnetization, $\mathbf{I}$ is the identity matrix, the matrix $\mathbf{E} = \exp(\mathbf{R}TR)$ describes relaxation during repetition time TR, and the diagonal matrix $\mathbf{C} = \mathrm{diag}(S^f, S^b)$, $S^f = \cos(\alpha)$, $S^b = 1$ corresponds to the instant rotation of the magnetization M_z^F by an excitation pulse with the flip angle α. The relaxation matrix $\mathbf{R}$ is defined as follows:

$$\mathbf{R} = \begin{bmatrix} -R_1^F - k & k(1-f)/f \\ k & -R_1^F - k(1-f)/f \end{bmatrix} \qquad [3.2]$$

where R_1^F and R_1^B are the longitudinal relaxation rates of the free pool and bound pool respectively. Applying the first-order approximation to the exponential terms, Eq. [3.1] can be simplified to

$$\mathbf{M_z} \approx (\mathbf{R}TR - \ln \mathbf{C})^{-1}\mathbf{R}\mathbf{M_{eq}}TR \qquad [3.3]$$

Corresponding approximated expression for the observed signal can be explicitly written as follows:

$$S \approx \frac{M_0(1-f)(R_1^F R_1^B + R_1^F k(1-f)/f + R_1^B k)\sin\alpha \exp(-TE/T_2^*)}{R_1^F R_1^B + R_1^F k(1-f)/f + R_1^B k - (R_1^B + k(1-f)/f)TR^{-1}\ln(\cos\alpha)} \quad [3.4]$$

We further assume that $R_1^F = R_1^B = R_1$ similar to earlier studies (3,9) that corresponds to the fast exchange conditions (51). With these assumptions, the signal intensity is expressed as:

$$S \approx \frac{M_0(1-f)R_1 TR\sin\alpha \exp(-TE/T_2^*)}{R_1 TR - \ln(\cos\alpha) + \frac{k\ln(\cos\alpha)}{R_1 + k/f}} \quad [3.5]$$

Finally, the relaxation rate R_1 can be neglected in the sum with a much larger term *k/f*, thus providing the signal equation

$$S \approx M_0(1-f)\frac{R_1 TR}{R_1 TR - (1-f)\ln(\cos\alpha)}\sin\alpha \exp(-TE/T_2^*) \quad [3.6]$$

By comparing Eq. [3.6] with the first-order approximation of the Ernst equation (64) (not shown for brevity), the relationship between the true R_1 and its apparent value R_1^{app} estimated from VFA data becomes evident:

$$R_1^{app} \approx R_1/(1-f) \quad [3.7]$$

Equation [3.7] demonstrates that the bias in R_1 caused by cross-relaxation is on the order of f and independent of the sequence parameters (TR and flip angles), if the first-order approximation is justified by a short TR. More general treatment for arbitrary sequence parameters can be found in Ref. (62,63).

3.2.2 *Effect of Apparent R_1 on the CRI Parameters*

The next goal is to estimate systematic errors in the two-pool model parameters due to R_1^{app} in the CRI method. We start our analysis with a simplified CRI model (3), which allows analytical investigation of errors in the estimated parameters in the regime where the direct saturation effect is negligible (Δ> 2.5 kHz) (57). According to this model, the ratio of signals with and without off-resonance saturation in a pulsed MT experiment can be expressed as

$$\frac{M_z^F(W^B)}{M_z^F(W^B=0)} \approx \frac{P+(Q-1)sW^B}{P+QsW^B} \qquad [3.8]$$

Where

$$P \approx \left(R_1 - \frac{(1-f)(\ln\cos\alpha)}{TR}\right)f^{-1} \qquad [3.9]$$

$$Q \approx \left(R_1 - \frac{(\ln\cos\alpha)}{TR}\right)k^{-1} + 1 \qquad [3.10]$$

and W^B is the saturation rate of the bound pool scaled by the duty cycle of the saturation pulse ($s = t_m/TR$, where t_m is the pulse duration). The saturation rate W^B depends on the offset frequency and the flip angle of the saturation pulse and is determined by the parameter T_2^B based on an appropriate spectral line shape model (typically Super-Lorentzian (44)). If the data are fitted in the form given by Eq. [3.8], the fitting algorithm searches for the optimal parameters P, Q, and T_2^B regardless of an actual R_1.

The effect of R_1 errors on the two-pool model parameters originates from the dependence of the coefficients P and Q on R_1 (Eqs. [3.9] and [3.10]). Accordingly, if R_1^{app} is supplied as input information, apparent values f^{app} and k^{app} will be obtained. The relationships between the

true f and k and their apparent values can be derived from the conditions $P(R_1^{app}, f^{app}) = P(R_1, f)$ and $Q(R_1^{app}, k^{app}) = Q(R_1, k)$, which result in the simple recalculation formulas:

$$f = Cf^{app}, \quad k = Ck^{app} \qquad [3.11]$$

Where the correction coefficient C is the same for both f and k and depends on T_R and the flip angle:

$$C = (R_1^{app} - TR^{-1}\ln(\cos\alpha))/(R_1^{app} - TR^{-1}\ln(\cos\alpha) + f^{app}R_1^{app}) \qquad [3.12]$$

The above analysis also suggests that R_1 errors should not affect T_2^B, since W^B is independent of R_1 (3). We refer below to the recalculation formulas (Eqs. [3.11] and [3.12]) as CRI with 1st order correction.

3.2.3 Standard and Modified CRI Approaches

In the original CRI approach (7), reconstruction of parametric maps is performed in two stages (figure 3.1). During the first stage, R_1 map is calculated by fitting VFA SPGR data the Ernst equation (55). During the second step, the matrix model of pulsed MT is fitted to MT-weighted data, while R_1 is supplied as an external parameter. Prior to fit, MT data are normalized pixel-wise by an arbitrary reference image typically obtained without saturation. The purpose of this normalization is to reduce the number of free parameters in the fit by excluding a multiplicative factor commonly referred to as *proton density*, which absorbs the effects of spin concentration, T_2^* decay, and coil sensitivity. The normalized data are then fitted to the corresponding ratio of analytical signal expressions with and without saturation $M_z^F(W^B)/M_z^F(W^B = 0)$. As an alternative to the standard CRI approach, we propose a modified CRI

(mCRI) reconstruction algorithm to perform a global fit of VFA and MT SPGR data simultaneously (figure 3.1). On the first stage, similarly to the standard CRI approach, the normalization procedure is uniformly applied to both VFA and MT data to exclude the common proton density term. Then, the normalized images are simultaneously fitted to the corresponding ratios of analytical signal expressions with and without saturation using Eq. [3.1] from this paper and Eq. [1] from Ref. (7), respectively. Accordingly, the global fit simultaneously yields all the remaining parameters (R_1, f, k, T_2^B) and automatically takes into account the cross-relaxation contribution into VFA data (figure 3.1).

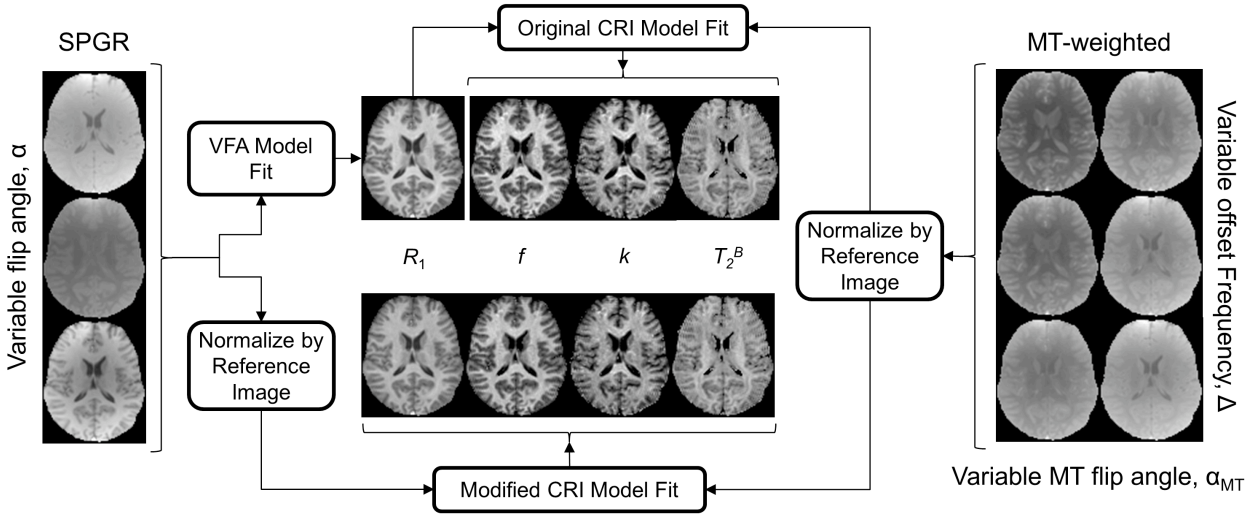

Figure 3.1. Original CRI and mCRI processing pipelines.

3.3 Materials and Methods

3.3.1 Simulations

To estimate errors in the two-pool model parameters caused by the unaccounted bi-exponential relaxation, synthetic VFA and MT SPGR signal intensities were generated using Eq. [3.1] from this paper and Eq. [1] from Ref. (7), respectively. Then, datasets were fitted using the

original CRI algorithm. The first-order correction formulas (Eqs. [3.7], [3.11], and [3.12]) were also evaluated. Specific parameters used in the simulations were taken from ROI measurements in the genu of corpus callosum (WM) and thalamus (GM) from full mCRI fit of the *in vivo* data presented below: 1) WM: $R_1 = 0.97s^{-1}$; $f = 15.36$ %; $k = 2.70s^{-1}$; $T_2^B = 9.84\mu s$; 2) GM: $R_1 = 0.71s^{-1}$; $f = 8.8\%$; $k = 1.57s^{-1}$; $T_2^B = 10.21\ \mu s$. To study the effect of approximations of the 1st order correction in realistic the imaging regime, pulse sequence parameters and sampling scheme in these simulations corresponded to those used in the *in-vivo* experiments detailed below.

3.3.2 Phantom Preparation

Five cross-linked BSA samples (98% bovine serum albumin, essentially fatty acid free, Sigma-Aldrich Corp., St. Louis, MO) were prepared with BSA percent weight of 10, 15, 20, 25, and 30 as described in (65). The BSA was dissolved in distilled water and was placed in the ice bath for 10 minutes. Then, 50 µl/ml of an ice-cold 25% glutaraldehyde solution (Sigma-Aldrich Corp., St. Louis, MO) were added to the BSA solution while stirring with a syringe needle. The samples were kept at the room temperature for two hours and then stored at 4º C.

3.3.3 Data Acquisition

Imaging experiments were carried out on a 3.0T GE Discovery MR750 (GE Healthcare; Waukesha, WI) using either an eight-channel transmit/receive knee coil (for phantom scans) or eight-channel phased array head coil (for a volunteer scan). All data were acquired with the 3D MT-weighted SPGR sequence in a strong spoiling regime (66) (spoiling gradient area $A_G = 450$ mT·ms/m, RF phase increment 169º). In the phantom experiment, eight Z-spectroscopic datasets were acquired (*TR*/*TE*=37/2.3ms, excitation flip angle α=15˚) with the 18 ms Fermi saturation

pulse applied at the offset frequencies Δ = 2.5, 10, 18, 26 kHz with two nominal saturation flip angles α_{MT} = 850˚ and 1300˚. Additionally, four VFA SPGR datasets were acquired using the same sequence with Δ = 250 kHz to ensure that the transmitter operates with identical gain settings (no MT effect is observed at this frequency) and flip angles optimized for the range of T_1 values in the phantoms (α = 6˚, 15˚, 35˚, and 50˚). The SPGR dataset with the highest signal-to-noise ratio (α = 15˚) was used as a reference image to normalize both Z-spectroscopic and VFA data as explained in the previous section. All datasets were acquired with FOV =140×105×48mm and matrix = 128×96×24. Single-slice 2D inversion-prepared spin-echo (IR) data were collected to determine reference T_1 values in the phantoms (*TR*/*TE* =5000/8.2ms, *TI* = 0.3, 0.5, 0.7, 0.9, 1.2, 1.6, 2s).

Informed written consent was obtained from a healthy volunteer in accordance with the local institutional policy. Eight Z-spectroscopic datasets were acquired using the same pulse sequences (Δ =2.5, 5, 9, 13 kHz, α_{MT} = 500˚, 1100˚, α=10˚). Four VFA datasets were acquired with flip angles α = 5˚, 10˚, 20˚, and 30˚. The image with α = 10˚ was used as a reference dataset. All Z-spectroscopic and VFA data were acquired with *TR*/*TE* = 40/2.0ms, FOV = 240×180×80mm and matrix = 128×96×42. The total scan time for this protocol was 35 minutes.

B_0 and B_1 maps were used to correct flip angle and local off-resonance frequency values in both phantom and volunteer studies. B_1 maps were acquired using the actual flip angle imaging (AFI) method (59) ($TR_1/TR_2/TE$ = 37/185/2.3 ms, α= 55˚, FOV =240×180×80mm, matrix = 96×72×28) with the strong spoiling regime. B_0 maps were calculated from the 3D fat-water separation method known as “iterative decomposition of water and fat with echo asymmetry and least squares estimation” (IDEAL) with FOV =240×180×80 mm and matrix =

256×256×42 (58). The scan time for these additional B_0 and B_1 mapping sequences was 10 minutes.

3.3.4 Image Processing and Analysis

The standard CRI processing workflow (figure 3.1) was implemented according to (7,67). In mCRI, all parametric maps were generated by fitting the normalized VFA and MT data simultaneously as described above (figure 3.1) using in-house-written C and MATLAB (MathWorks, Natick, MA) software utilizing a standard "*lsqnonlin"* function for nonlinear least squares voxel-based fitting (http://www.medphysics.wisc.edu/~samsonov/qmap). All quantitative parameters estimated in phantom scans and *in-vivo* were obtained from parametric maps in manually drawn regions-of- interest (ROIs).

To study the association between BSA content and the bound pool fraction determined by different processing approaches, we performed linear regression analysis using the following model:

$$f = \beta_1 \times BSA\% + \beta_0 \qquad [3.13]$$

The strength of anticipated linear relationships was assessed using the Pearson's correlation coefficient. We additionally tested if the intercept β_0 is significantly different from zero (the anticipated value for f at BSA%=0). Statistical significance of differences between parameter measurements by CRI, mCRI, and CRI with the first-order correction was assessed using a paired two-tailed t-test.

3.4 Results

3.4.1 Simulations

Table 3.1 shows the systematic errors in the estimated parameters in WM and GM obtained from the original CRI method, mCRI, and CRI with the first-order correction. As predicted by the theory, the R_1 bias propagates into f and k measurements but does not affect T_2^B, and it is most prominent for WM. A major portion of the biases is removed by proposed the first-order correction, with R_1 and f being corrected most efficiently (<1% residual error).

Table 3.1. Simulated relative bias in two-pool MT model parameters obtained by the original CRI and its first-order correction due to unaccounted bi-exponential relaxation for WM and GM.

	Original CRI				**1st Order Correction**		
	R_1	f	k	T_2^B	R_1	f	k
WM	16.92%	12.42%	15.20%	-0.08%	-0.96%	-0.42%	2.04%
GM	8.88%	5.95%	6.46%	-0.07%	-0.64%	-0.24%	0.24%

Figure 3.2 further illustrates the dependence of the biases on the fraction of bound protons in WM. Again, unaccounted bi-exponential relaxation in the SPGR signal model introduces a substantial bias into all quantitative MT parameters except for T_2^B when estimated by the original CRI method. These errors affect most significantly R_1 values, then k and f values. They are steadily growing with the bound pool fraction as predicted by Eqs. [3.7] and [3.11]. The first-order correction (Eqs. [3.11] and [3.12]) removes most of the bias for a wide range of f values, while the level of residual errors increases with an increase in f. The first-order correction is less accurate for k values where the residual bias may reach up to ~5% for tissues with a higher macromolecular content.

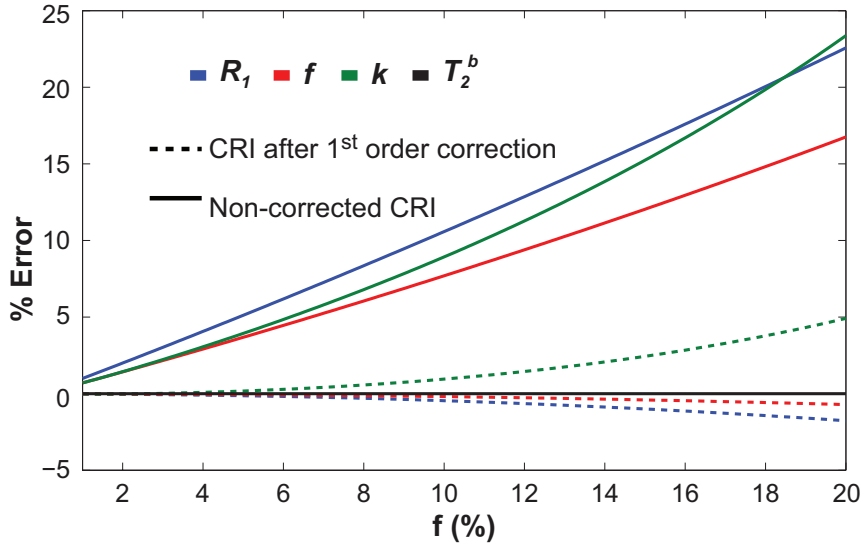

Figure 3.2. Relative bias in parameters estimated using original CRI before and after first-order correction vs. bound pool fraction. The other two-pool model parameters were fixed with values corresponding to WM.

3.4.2 Phantom Studies

Figure 3.3 shows estimates of the two-pool MT model parameters in the BSA phantoms obtained by the original CRI, mCRI, and CRI with the first-order correction, as well as R_1 values from the reference IR experiment. Both mCRI fit and the first-order correction of CRI fit provide a good agreement with the reference IR R_1 measurements, while the standard VFA method results in substantial discrepancy with IR R_1 estimates. The difference between R_1 values measured by the VFA method and IR method increases with BSA concentration as predicted by Eq. [3.7] and the simulations (figure 3.2).

Similarly, the original CRI tends to overestimate bound pool fraction f and cross-relaxation rate k in the phantoms with a higher concentration of BSA. Although the first-order correction of f provides a good agreement with the mCRI fit for all concentrations, an increase in

the macromolecular content leads to a poorer first-order correction for k, as predicted by the simulations (figure 3.2). T_2^B is consistent among different concentrations of BSA.

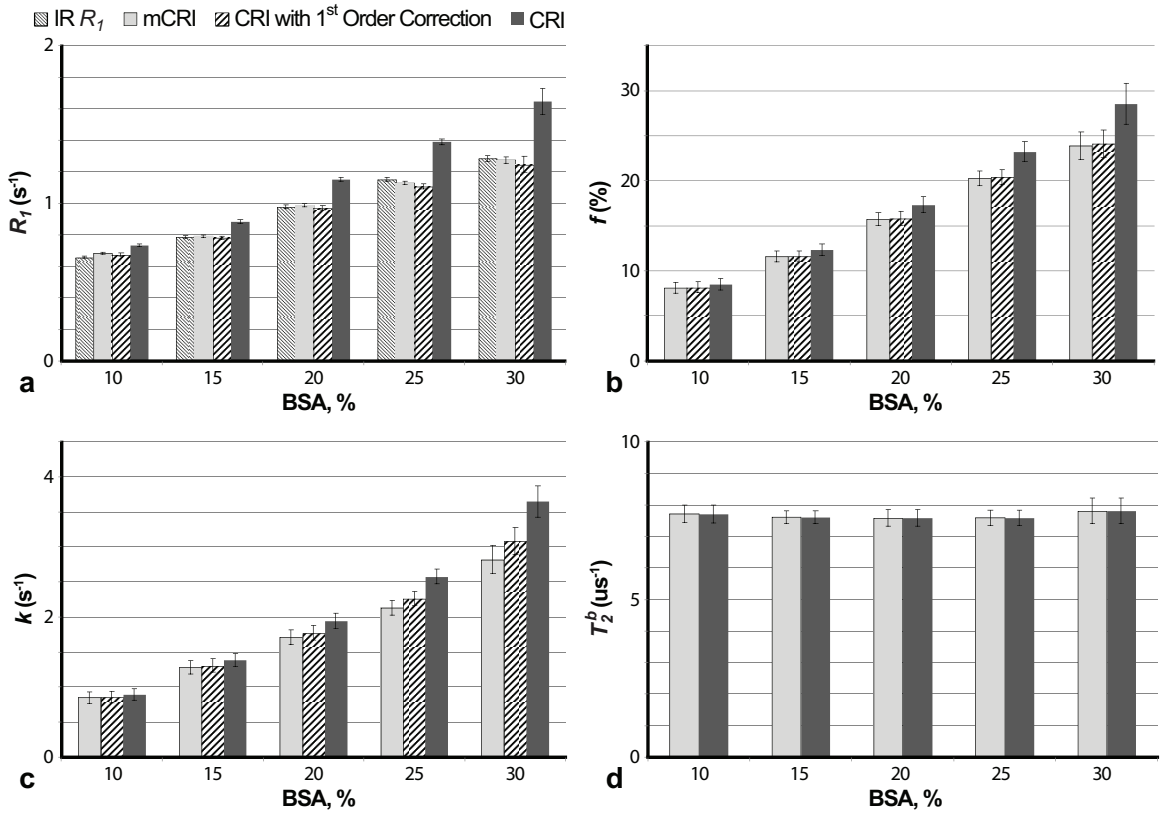

Figure 3.3. Comparison of qMT parameters estimated using original CRI (without and with first-order correction) and mCRI in phantoms with different BSA concentrations. **a**: R_1 measurements. IR R_1 values are shown for reference. **b–d**: f, k, and T_2^B measurements, respectively. Error bars indicate standard deviations in ROI measurements taken from parameter maps.

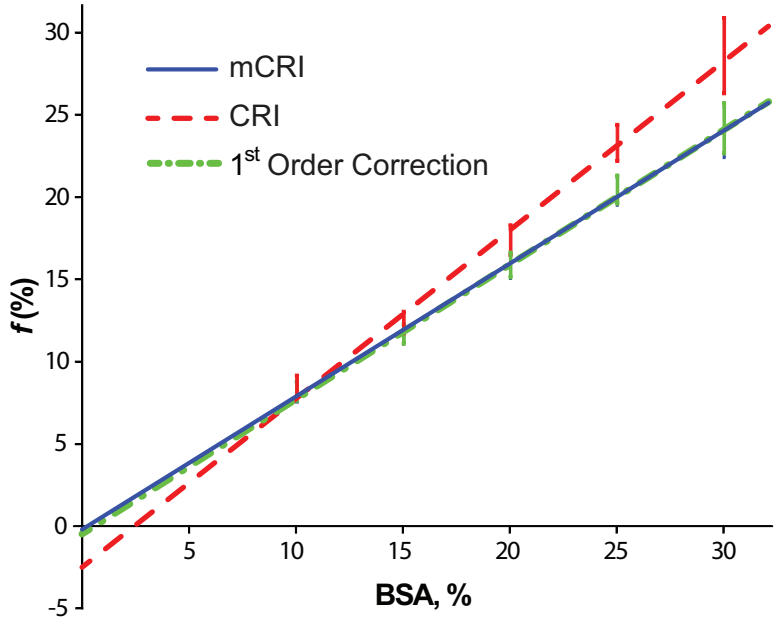

Figure 3.4. Results of linear regression of bound pool fraction values derived by CRI, CRI with the first-order correction, and mCRI vs. BSA concentration. Error bars indicate standard deviations in ROI measurements taken from parameter maps.

Figure 3.4 and Table 3.2 show results of linear regression analysis of *f* from phantom data. The bound pool fraction strongly correlates with BSA concentration for both CRI and mCRI, though the original CRI estimation lead to a somewhat weaker correlation (Table 3.2). The intercept of the fitted line for mCRI and the first-order correction is not significantly different from zero, thus reflecting the anticipated absence of the bound proton pool at 0% BSA concentration. At the same time, the intercept of the fitted line for original CRI is significantly different from zero and appears in the physically unrealistic range (~ -2.5%).

Table 3.2. Results of linear regression analysis for bound pool fraction *f* in BSA phantoms.

	β_0 (*p*-value)	β_1	R^2
CRI	-2.46e-2 ± 0.18e-3 ($<10^{-4}$)*	1.02e-2 ± 8.63e-5	0.965
First Order Correction	-0.25e-2 ± 1.31e-3 (0.053)	0.81e-2 ± 6.16e-5	0.972
mCRI	-0.14e-2 ± 1.27e-3 (0.256)	0.80e-2 ± 6.00e-5	0.972

Asterisk (*) indicated that the difference between the intercept of the fitted line and zero is statistically significant.

3.4.3 In-Vivo Results

Figure 3.5 compares parametric maps obtained using the mCRI processing approach with original CRI and its first-order correction. Table 3.3 provides quantitative comparisons of qMT parameters in several WM and GM regions of interest. Processing with mCRI resulted in structurally similar, but quantitatively different parametric maps.

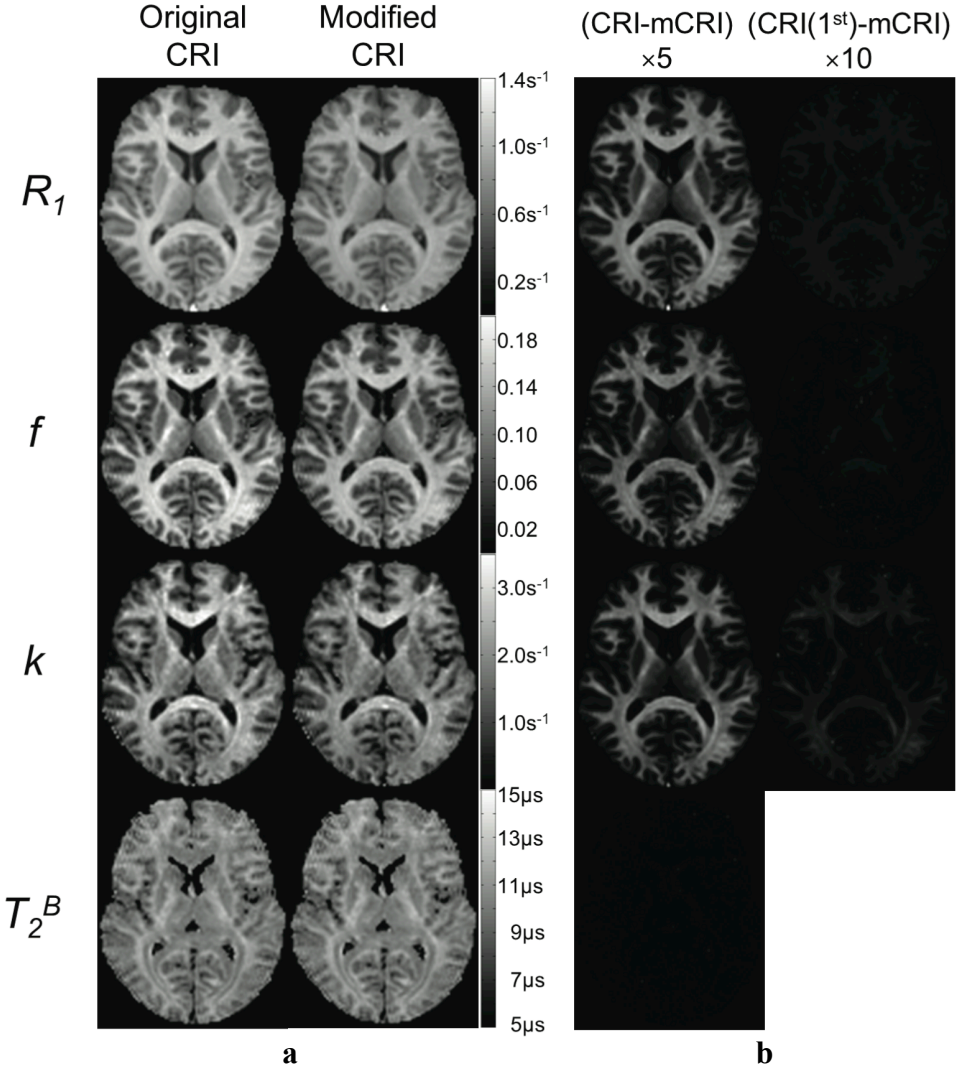

Figure 3.5. Parametric MT maps estimated using original CRI and mCRI (**a**), and errors of original CRI and its first-order correction [CRI (1^{st})] presented as difference maps with respect to mCRI (**b**). Note the consistency between levels of error in individual maps vs. macromolecular content as revealed by the bound pool fraction.

Table 3.3. In vivo measurements of the two-pool MT model parameters using modified CRI (mCRI), original CRI, and CRI with first-order correction.

Regions of Interest	mCRI				Original CRI				1st Order Correction		
	R_1 (s^{-1})	f (%)	k (s^{-1})	T_2^B (μs)	R_1 (s^{-1})	f (%)	k (s^{-1})	T_2^B (μs)	R_1 (s^{-1})	f (%)	k (s^{-1})
White Matter											
Cerebral peduncle	0.933	14.81	2.064	11.560	1.088	16.54	2.353	11.556	0.928	14.73	2.097
Corona radiata	0.894	13.87	1.979	11.731	1.032	15.44	2.247	11.722	0.889	13.87	2.019
Corpus callosum, genu	0.966	15.36	2.702	9.844	1.133	17.28	3.115	9.836	0.959	15.30	2.758
Corpus callosum, splenium	0.942	14.92	2.517	10.197	1.105	16.75	2.890	10.187	0.940	14.90	2.570
Frontal white matter	0.898	13.93	2.161	11.231	1.036	15.49	2.445	11.223	0.892	13.90	2.196
Internal capsule, anterior limb	0.932	13.88	2.327	10.171	1.085	15.52	2.651	10.162	0.934	13.91	2.378
Internal capsule, posterior limb	0.903	15.33	2.048	11.836	1.057	17.20	2.356	11.829	0.896	15.26	2.092
Middle cerebrallar peduncle	0.855	14.28	1.993	10.473	0.999	15.99	2.220	10.443	0.855	14.33	1.990
Occipital white matter	0.924	14.79	1.898	10.628	1.080	16.73	2.198	10.621	0.919	14.89	1.956
Gray Matter											
Cerebral cortex	0.739	6.6	1.102	9.023	0.781	6.89	1.122	8.987	0.729	6.58	1.072
Caudate nucleus	0.655	6.42	1.321	9.628	0.702	6.71	1.380	9.619	0.657	6.43	1.322
Putamen	0.710	7.29	1.432	9.736	0.770	7.66	1.512	9.728	0.714	7.29	1.439
Substantia nigra	0.788	8.59	1.371	9.817	0.863	9.14	1.462	9.808	0.789	8.59	1.375
Thalamus	0.707	8.77	1.569	10.208	0.780	9.36	1.682	10.198	0.711	8.8	1.583

For all parameters except for T_2^B, the error images reveal dependence of the bias on the macromolecular content as predicted by simulations and phantom studies. First-order correction efficiently minimizes the errors in f and R_1. However, there is still visible residual error for k values after first-order correction, with most appreciable residue in WM regions, which is in agreement with simulations and phantom experiments (figures 3.2 and 3.3, Table 3.1). Statistical analysis of ROI data detected significant differences between CRI and mCRI for all parameters except for T_2^B in gray matter (Table 3.4). The effect of first-order correction was also significant

for R_1, f, and k. There were significant differences between mCRI and the first-order correction for R_1 and k. These systematic errors as well as bias between mCRI and the first-order correction (Table 3.4) are consistent with the estimates predicted in simulations (Table 3.1).

Table 3.4. Average relative bias between mCRI and CRI without and with first-order correction calculated from in vivo ROI measurements (Table 3). Bold font indicates significantly different results ($p<0.05$).

	CRI				**1st Order Correction**		
	R_1	f	k	T_2^B	R_1	f	k
WM	**15.33%**	**11.34%**	**13.21%**	**0.09%**	**-0.41%**	-0.06%	**1.85%**
GM	**7.94%**	**5.39%**	**5.2%**	0.15%	0.03%	0.05%	0.06%

3.5 Discussion

MT imaging offers unique sensitivity to macromolecular content in tissues that cannot be assessed with conventional MRI. Accurate modeling of MT processes using the two-pool model is essential to yield specific parameters characterizing the macromolecular fraction in both normal and pathological conditions. This study demonstrates on the example of CRI, one of qMT methods based on SPGR pulse sequence, that separate treatment of VFA and MT data may cause non-negligible systematic errors in both R_1 and quantitative MT parameters such as bound pool fraction f and cross-relaxation rate k. Specifically, this type of errors can be characterized as overestimation of R_1, f, and k with a relative bias comparable with magnitude of f (figure 3.2, Tables 3.1, 3.3, and 3.4). As the effect of the MT-induced bi-exponential longitudinal relaxation on the parameter estimates strongly depends on the macromolecular content in tissues (figure 3.2), the original CRI method and other qMT analysis techniques that do not take into account this effect may make interpretation of quantitative parameters inconsistent for different tissues types in different pathological conditions. It is also important to emphasize that apparent R_1

values obtained from the standard single-compartment VFA technique are biased proportionally to f, and, hence, represent non-specific measures containing contributions from both intrinsic T_1 relaxation properties of water protons in tissues and cross-relaxation.

We demonstrated that the accuracy of CRI estimates could be noticeably improved with the proposed combined data fit algorithm. Our modified CRI (mCRI) data processing approach does not require any additional measurements, thus maintaining the same time-efficiency as the original CRI technique. The mCRI method yields unbiased VFA R_1 estimation, resulting in a decrease in R_1 values by approximately 15% in WM and 8% in GM (Tables 3.3 and 3.4), which agrees well with the bias predicted earlier (62). In addition to the modified CRI fit, we have proposed simple analytical first-order approximated correction formulas allowing recalculation of original CRI-based parameters. The residual bias of such correction was shown both theoretically and experimentally to increase with macromolecular content due to violation of the first-order approximation. It may reach about 2% for k and 1% for f and R_1 in the ranges of physiologically reasonable values for brain tissues. Nevertheless, first-order correction employed as a simple post-processing step in the original CRI processing pipeline (figure 3.1) may be a valid alternative to mCRI when either faster processing is required or previously computed parameter values need to be refined. Since the residual error after first-order correction increases with f, care must be taken when applying this approach to tissues with a markedly high macromolecular content. Additionally, a combination of either mCRI fit or the first-order correction with the recent single-point CRI technique (9) provides a promising approach for fast and unbiased estimation of water proton R_1 values within the VFA method (68). Finally, it should be pointed out that other sources of bias in the VFA method need to be eliminated in conjunction with the proposed methodology, similar to the procedures described in

this study. Practically, VFA R_1 mapping should be performed with a 3D sequence providing a uniform slab profile, B_1 correction, and appropriate spoiling conditions (65,66).

The described analysis and correction methods have several potential limitations. One is the fundamental limitation of the two-pool model for accurate description of multiple exchanging compartments in biological tissues (47,69). Another is a specific assumption about the longitudinal relaxation rate of the bound pool $R_1{}^{\mathrm{B}}$. Particularly, a recent study (51) demonstrated that widely adapted approximations $R_1^B = 1s^{-1}$ (1,2) or $R_1^F = R_1^B$ (3,9) may considerably underestimate actual values of this parameter. Accordingly, this may cause an additional bias in the two-pool model parameters obtained using all qMT techniques based on the above assumptions about R_1^B. However, it remains unclear at this point whether a faster longitudinal relaxation rate of the bound pool is an intrinsic property of macromolecular protons or a manifestation of more complex equilibriums involving water proton fractions with different mobility. The later hypothesis is logical in view of a shorter T_1 found for the short-T_2 water fraction commonly termed "myelin water" (33,35,47,70,71). Yet another limitation is the assumption about a negligible effect of the excitation pulse on the bound pool. This approximation is common for off-resonance pulsed quantitative MT methods employing low-angle excitation pulses (2-4,7,9), which cause negligible on-resonance saturation of the bound pool magnetization. However, as was shown earlier (63), the effect of on-resonance saturation should be taken into account for sequences with very short *TR* and high flip angles, the conditions typical for balanced steady state precession (bSSFP) imaging. In the two-pool formalism with pulsed excitation (Eq. [3.1]), on-resonance saturation of the bound pool can be taken into account by assigning an actual saturation factor S^b<1 in the diagonal matrix **C**. Corresponding S^b values can be estimated from the properties of the excitation pulse (duration

and flip angle) and a spectral line shape of the bound pool (8,60). Based on this approach, we found for a particular pulse used in our sequence that on-resonance saturation of the bound pool results in an almost negligible effect on the accuracy of the two-pool model parameters determined by mCRI (<1% relative error for comparison between fits with actual S^b vs. S^b =1). However, this aspect of the technique could be important in the context of its standardization for future multi-center clinical studies since variations in the shape, duration, and flip angle of the excitation pulse may introduce a small but non-negligible bias dependent on a particular sequence implementation. Similarly, the approximation of the effect of the excitation pulse on the free pool by the term $\cos\alpha$ in the matrix **C** (Eq. [3.1]) may not be absolutely correct due to relaxation during RF pulses of finite duration. Such an effect has been recently described (72), and its role for both VFA R_1 and CRI parameter measurements remains to be investigated. In summary, while this study relies on the commonly accepted in the quantitative MT methodology approximations, future refinements of CRI accuracy seem to be possible based on accommodation of multi-compartment magnetization exchange schemes and a more rigorous analysis of magnetization dynamics during RF pulses.

3.6 Conclusions

This study demonstrates on the example of CRI that the accuracy of quantitative MT imaging can be considerably improved by taking into account the contribution of bi-exponential longitudinal relaxation into VFA R_1 measurements. We have developed the two technical approaches allowing correction of biases in CRI parameter estimates caused by the MT-induced bi-exponential behavior of longitudinal relaxation of water spins based on either the global fit of both VFA and MT SPGR data to the two-pool signal model or the simple analytical recalculation formulas for key cross-relaxation parameters. While the choice between these techniques depends on a tradeoff between the correction accuracy and image processing speed, both approaches do not require extra data compared to the original CRI method.

Chapter 4: Rapid and Accurate Bound Pool Fraction (f) and T_1 Mapping

4.1 Introduction

Several studies have found a strong association between bound pool fraction (*f*) and the myelin content in neural tissues (13-15,17,73-75). In previous chapters, we demonstrated cross-relaxation imaging method (7) to estimate *f* and other parameters of a two-pool MT model and showed the method to correct the biases in CRI parameters and R_1 ($1/T_1$) estimation caused by on-resonance MT effect (53).

Furthermore, variable flip angle (VFA) acquisition using spoiled gradient echo (SPGR) (55,76) has become a widely accepted approach for fast high resolution mapping of longitudinal relaxation rate $R_1=1/T_1$. However, recent studies have shown that magnetization transfer (MT) between free and bound protons due to the application of an on-resonance excitation pulses causes a significant bias in steady state MR signal in tissues with natural abundance of macromolecular content (53,63). Ou et al. predict up to 14% error in white matter (WM) VFA *T1* values (62), an effect comparable to white matter T_1 changes observed in multiple sclerosis (77). Explicit consideration of a two-pool MT model in VFA experiments may improve the accuracy of *T1* estimation (53,62). However, due to very low sensitivity of the modified VFA signal model to parameters of the two pool MT model such as bound pool fraction *(f)*, cross-relaxation rate *(k)*, transverse relaxation times of the bound pool T_2^B, and free pool T_2^F, the feasibility of MT-corrected *in vivo* T_1 mapping using VFA measurements only is limited. Cross-relaxation imaging (CRI) provides a convenient framework to model the effect of both off-resonance MT and on-resonance excitation pulses on bound and free proton pools (7). It was recently demonstrated that combination of VFA and pulsed MT-weighted SPGR measurements within modified CRI (mCRI) framework might be used to remove bias due to on-resonance MT in both VFA R_1 values and two-pool MT parameters (53). However, this approach requires

augmenting VFA measurements with multiple MT acquisitions (more than 4) to allow estimation of the full set of parameters.

Here, we demonstrate a method to obtain accurate *f* and T_1 maps of clinical quality; using a standard set of VFA datasets augmented with just a single off-resonance MT-weighted SPGR scan.

4.2 Theory

The theory of pulsed MT was comprehensively described in chapter 2. In summary, the longitudinal magnetization in the pulsed steady state derived for SPGR sequence with MT pulse for two-pool MT model can be expressed as:

$$\mathbf{M_z} = (\mathbf{I} - \mathbf{E_s}\mathbf{E_m}\mathbf{E_r}\mathbf{C})^{-1}([\mathbf{E_s}\mathbf{E_m}(\mathbf{I} - \mathbf{E_r}) + (\mathbf{I} - \mathbf{E_s})]\mathbf{M_{eq}} + \mathbf{E_s}(\mathbf{I} - \mathbf{E_m})\mathbf{M_{ss}}) \qquad [4.1]$$

The above equation is used to estimate the parameters (*PD*, T_1, *f*, *k*, T_2^B, T_2^F) of two-pool model from several SPGR data without and with MT pulse at different offset frequency (Δ) and MT pulse power (α_{MT}). To target this approach for fast *f* and T_1 mapping, we simplify the full model by constraining some of the parameters (*k*, T_2^B, T_2^F) of two-pool model for brain proposed by previous studies (9,13). Estimating of T_2^F can be obtained using the fact that the product of $T_2^F R_1^F$ is pretty constant in brain tissues and it's approximately 0.022 at 3.0T. It was shown that the reverse constant rate (*R*) could be fixed to 19.0 s^{-1} within tissue as tissue-dependent variability *R* is much smaller compared to the other parameters of two-pool MT model, which makes the forward rate constant *k* constrained.

$$R = k(1 - f)/f \qquad [4.2]$$

Another parameter that can be constrained in brain is T_2^B, which is shown to be less variable within the whole brain and the average-brain T_2^B is 10 μs. The specific values of these fixed parameters are listed in the literature from different ROIs of brain (7,9,13,67), but the choice of MT measurement is important to preserve the accuracy and precision of f and T_1 estimation.

The sensitivity analysis of pulsed z-spectra in white matter, gray matter, and MS lesion has been demonstrated by (9) to examine the effect of two-pool MT parameters on the signal across the range of Δ and α_{MT}, where the relative sensitivities are defined as:

$$s_p = \frac{\partial m_z}{\partial p}\frac{p}{m_z}, \qquad \text{where } p \equiv f, R, T_2^B, T_2^F \qquad [4.3]$$

Which shows the percentage change in the signal caused by a percentage change of each parameter. Therefore, if the sensitivity to a particular parameter is low then we could use this knowledge for model reduction.

It has been shown that the sensitivity to f has the largest value compared to the other parameters of two-pool model, and the sensitivity to the other parameters (R, T_2^B, T_2^F) has its minimum value in ranges Δ = 4-7kHz, and α_{MT} = 600°-900° (9).

4.3 Simulation

Furthermore, we run simulations to identify the ranges of an offset frequency and an MT flip angle of a VFA-augmenting MT scan for which the effect of such constraints on accuracy of T_1 and f is minimal. Figure 4.1 illustrates the effect of two-pool MT model parameters on

observable T_1 values when calculated using standard VFA method. The error in T_1 increases almost linearly with f for typical values of k observed in neural tissues (>1) and hence is expected to be most biased in macromolecular-rich tissues such as white matter. The sensitivity of T_1 to T_2^B was negligible.

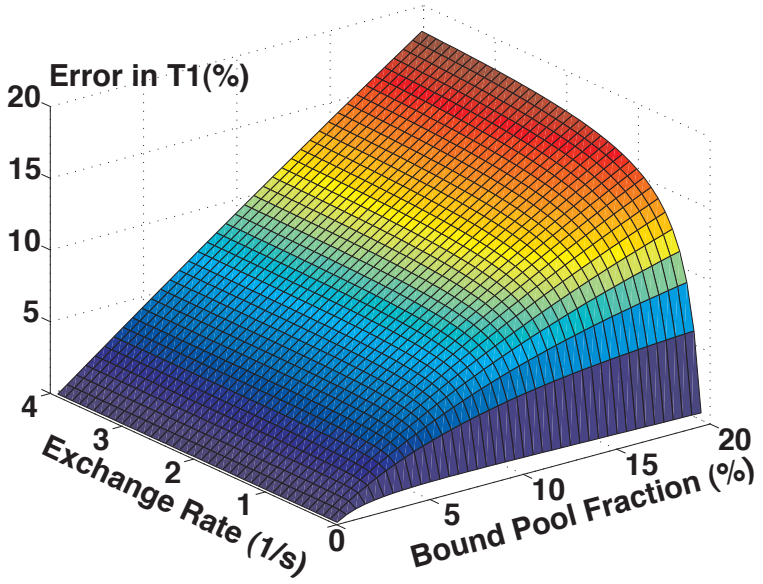

Figure 4.1. Error of VFA T_1 values vs. quantitative MT parameters f and k. The error in T_1 increases almost linearly with f for typical values of k observed in neural tissues.

Figure 4.2 shows the effect of off-resonance frequency and MT flip angle of a VFA-augmenting MT scan on the average loss in R_1 and f for the proposed simultaneous constrained estimation of these parameters. Similar to observations in [7], there is a range of Δ and MT flip angle with low sensitivity to the fixed parameters (Δ=4-6kHz, α_{MT}=400-600˚).

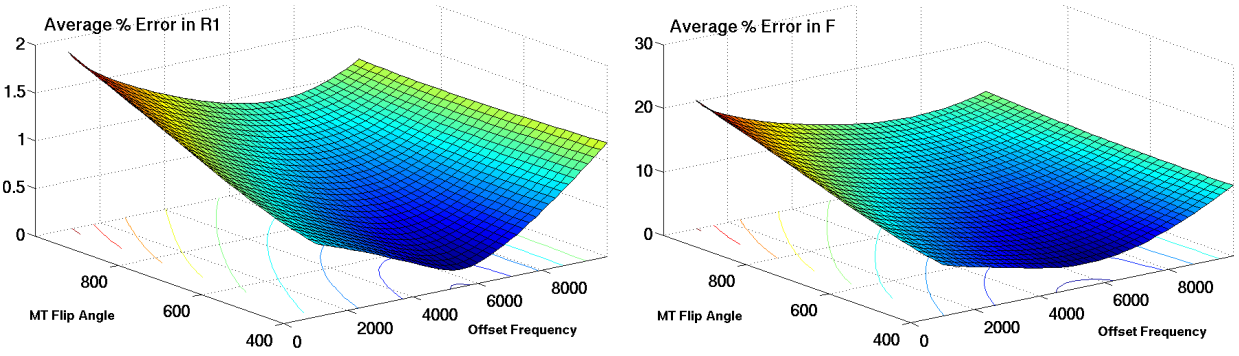

Figure 4.2. Dependence of error in estimation of $R_1=1/T_1$ (left) and f (right) due to constraining vs. offset frequency and MT flip angle for proposed 3-point protocol. We have lowest error in R_1 and f estimation in the ranges of Δ = 4-6kHz, α_{MT} = 400-600˚.

4.4 Rapid and Accurate T_1 Mapping

Accurate estimation of T_1 values from VFA measurements requires consideration of magnetization transfer effects, which may introduce T_1 bias roughly proportional to the macromolecular content. The fast T_1 correction protocol (VFA-MT) requires a single MT scan in addition to regular VFA measurements for accurate *T1* mapping.

4.4.1 Phantom Experiment

The proposed method was applied to correct T_1 mapping in the 25% gelatin phantom (f≈4%). Phantom protocol included acquisition of 3D VFA data α = [7, 15, 35, 50]˚ and MT SPGR data (α = 15˚, offset Δ = 2.5, 5, 9, 13 kHz, α_{MT} = [850,1300]˚, 18ms Fermi pulse, 120×120×88mm FOV, 128×128×44 matrix, TR/TE=37/2.3ms). Single-slice, 2D inversion-prepared spin-echo (IR) data was collected to determine a reference *T1* value in the phantom (TR/TE=5000/8.2ms, TI = 0.05, 0.1, 0.2, 0.3, 0.5, 0.7, 0.9, 1.2, 1.6, 2s). Examination of mean phantom T_1 values obtained with full mCRI (12 measurements), proposed constrained VFA-MT (3 measurements) and VFA (2 measurements) confirmed that both full mCRI and VFA-MT

provide excellent agreement with the reference IR T_1 measurement (figure 4.3). At the same time, VFA T_1 was biased by approximately f, which is consistent with simulations in figure 4.1.

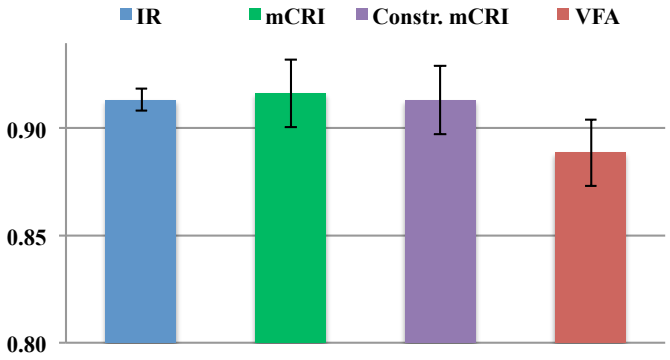

Figure 4.3. Phantom T_1 values calculated by different methods. Both mCRI and proposed 3-point method provide excellent agreement with the reference IR T_1 measurement.

4.4.2 In Vivo Experiment

Volunteer brain data included 3D VFA (α = [5, 10, 20, 30]˚) and MT SPGR (α = 10˚, Δ=2.5, 5, 9, 13 kHz, α_{MT} = [500,1100]˚, 18ms Fermi pulse, 240×180×80mm FOV, 128×96×40 matrix, TR/TE=40/2.0ms). The reference MT-corrected T_1 maps were obtained by simultaneous fit of all VFA and all MT data to the modified CRI model. Figure 4.4 reveals that there is a visible bias in T_1 map obtained with regular VFA compared to T_1 maps obtained with on-resonance MT effect correction. The MT-corrected values (T_{1WM}=1050±25, T_{1GM}=1537±25) agree well with literature (78) (T_{1WM}≈1060, T_{1GM}≈1630), while VFA underestimated them (T_{1WM}=931±34, T_{1GM}=1462±28).

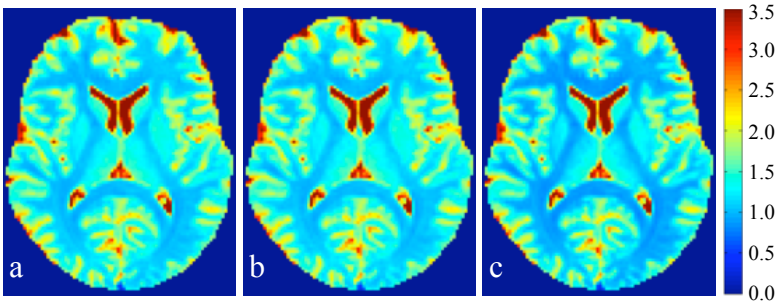

Figure 4.4. *In vivo* T_1 maps estimated by full mCRI (**a**), 3-point VFA-mCRI (**b**), and VFA (**c**). There is a visible bias in T_1 map obtained with regular VFA compared to T_1 maps obtained with on-resonance MT effect correction.

The whole brain T_1 histograms (figure 4.5) show excellent correlation between reference mCRI values and proposed 3-point VFA-MT approach. The method corrected VFA T_1 values by 11.5% in WM and 6.2% in GM, which agrees well with the bias predicted by (62).

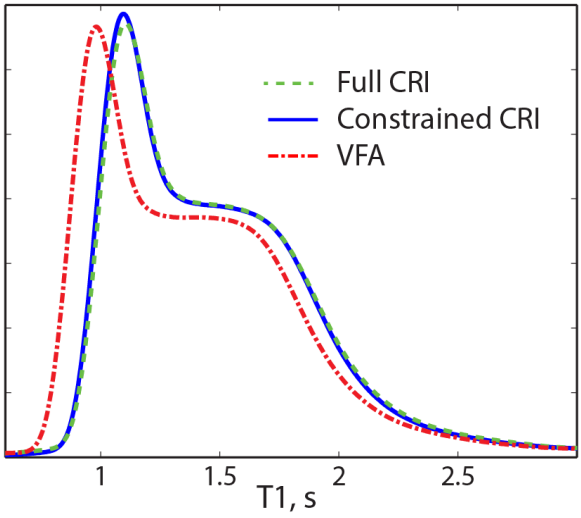

Figure 4.5. Brain T_1 histograms from different methods. There is a great correlation in T_1 estimation between full mCRI and constrained.

4.5 High Resolution and Rapid *f* And T_1 Mapping

The presented approach is promising for fast high-resolution whole brain f and T_1 mapping within clinically acceptable scan times. The original mCRI protocol was using 12 measurements (4 SPGR and 8 MT-weighted SPGR) to estimate all parameters of two-pool

model. The total scan time with this protocol is about 40 minutes at 2×2×2 mm^3 resolution. With new proposed 3-point constrained method, we can correctly estimate f and T_1 of the brain using 3 measurements (2 SPGR and one MT-weighted SPGR) in 20 minutes at 1×1×2 mm^3.

Figure 4.6 shows the results of brain f and T_1 mapping using the full mCRI protocol and the new 3-point constrained method from separate scan of the same volunteer.

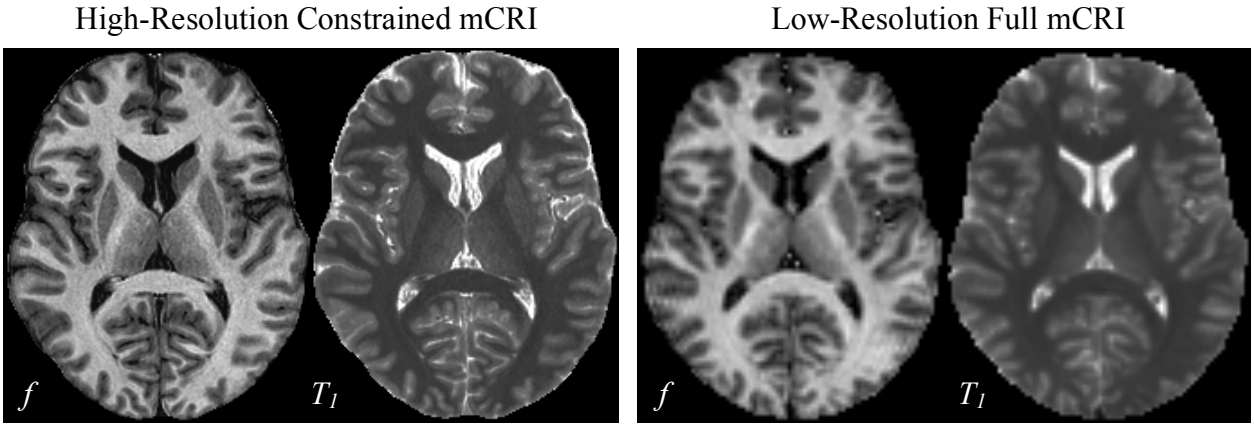

Figure 4.6. Brain f and T_1 maps generated by different methods. Using 3-point constrained mCRI method we can acquire 4 times higher resolution f and T_1 maps in half the scan time compared to full mCRI method.

Furthermore, the 3-point constraint protocol can even get faster using parallel MRI. We recently, acquire high-resolution (1.3×1.3×1.3 mm^3) sagittal brain f and T_1 in 15 minutes, which makes this protocol clinically convenient (figure 4.7).

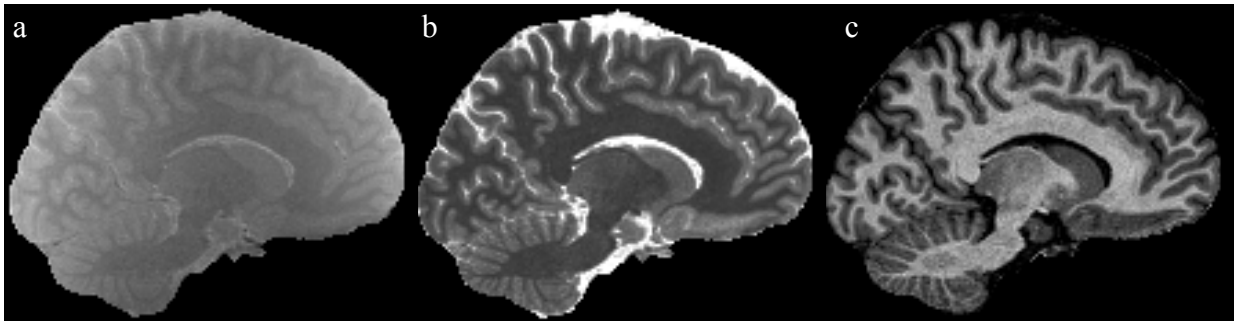

Figure 4.7. Brain PD (**a**), T_1 (**b**), and f (**c**) maps generated by 3-point mCRI method using parallel MRI in 15 minutes.

4.6 Discussion

Accurate estimation of f and T_1 values requires consideration of magnetization transfer effects, which may introduce T_1 bias roughly proportional to the macromolecular content. The optimized fast f and T_1 correction protocol developed in this work (VFA-MT) requires a single MT scan in addition to regular VFA measurements for accurate T_1 mapping. Our results show that accuracy of the original CRI approach is improved with the proposed combined data fit, which accounts for MT effects on the apparent T_1. In brain imaging, the method corrected VFA T_1 values by 13% in WM and 5% in GM, which agrees well with the bias predicted by (62). The presented approach is promising for fast high-resolution whole brain f and T_1 mapping with correction of MT effects within clinically acceptable scan times (~15 minutes).

Chapter 5: Modeling and Minimization the Effects of a Non-Exchanging Water Component in Quantitative Magnetization Transfer Imaging

5.1 Introduction

Multiple sclerosis (MS) is a chronic demyelinating disease that affects both the gray matter and white matter of central nervous system. Recently, it has been shown different pathological abnormalities in the gray matter of MS patients such as hypo-metabolism (79), atrophy (80,81), direct plaque formation (82), depletion of neuronal metabolites (80), and change in imaging parameters such as reduced *MTR* (83-85), increased diffusivity (86), and T_2 hypo-intensity (87). This demonstrates MS as a whole brain disease in which gray matter involvement has been identified pathologically and through imaging (79-85,88-95). Therefore, there is a need to correctly characterize the changes in GM due to disease process.

Magnetization transfer (MT) imaging provides essential information about tissue microstructure due to its sensitivity to immobile macromolecular protons not detectable by conventional MRI. MT imaging including both semi-quantitative, MT ratio (*MTR*), and quantitative (qMT) approaches serve as natural indicators of tissue microstructural properties such as myelination level in both gray and white matter structures. Various methods have been proposed to quantify the MT effect in tissue (2,3,6,7). Such quantitative MT (qMT) imaging methods provide unique parameters sensitive to macromolecular tissue composition, which is useful for assessing pathological tissue conditions (13,17).

The majority of *in vivo* qMT imaging methods are based on a two-pool model, in which macromolecular protons (bound pool) are assumed in exchange with free water protons (free pool). The two-pool MT model often provides a reasonable tradeoff between accuracy of complex MT models (96) and feasibility of *in vivo* application (47), and this two-pool model is a good approximation for homogenous tissue with no partial volume effect (PVE) with non-exchanging or very slow exchanging components such as cerebrospinal fluid (CSF).

Its applications to cortical GM characterization, however, have to take into account additional factors pertinent to anatomical organization of cortical GM such as partial volume effect with CSF, the significant confounder in many quantitative MRI techniques (97-99). Therefore, a better characterization of CSF contamination effects in different cortical regions is required in order to disentangle actual changes in microstructure of GM itself from changes due to other effects such as macroscopic morphological changes (97). However, at typical MRI resolutions, the two-pool model is inadequate to describe the signal behavior with partial volume effect with non-exchanging compartments. The presence of these non-exchanging or very slowly exchanging compartments will underestimate key qMT parameters, especially in gray matter (GM) where significant CSF partial volume voxels exists (98,99).

To minimize partial volume effects in qMT measurements, we propose an extended MT model where a two-pool MT subsystem is augmented by a third non-exchanging and very slowly exchanging (NE) pool. We compare the accuracy and precision of the three-pool model to the two-pool model through numerical simulation, and we validate the three-pool model in phantom experiment and in vivo study.

5.2 Theory

5.2.1 Cross-Relaxation Imaging

The theory of pulsed MT effect on the two-pool MT model has been described previously (3,7,53). In summary, the vector of longitudinal steady state magnetizations of the SPGR acquisition in the presence of an off-resonance saturation radio frequency (RF) pulse can be shown in the following matrix format:

$$\mathbf{M_z} = (\mathbf{I} - \mathbf{E_s}\mathbf{E_m}\mathbf{E_r}\mathbf{C})^{-1}([\mathbf{E_s}\mathbf{E_m}(\mathbf{I} - \mathbf{E_r}) + (\mathbf{I} - \mathbf{E_s})]\mathbf{M_{eq}} + \mathbf{E_s}(\mathbf{I} - \mathbf{E_m})\mathbf{M_{ss}}) \quad [5.1]$$

Where $\mathbf{M_z} = [M_z^F \ M_z^B]^T$, M_z^F, M_z^B are longitudinal magnetizations of free and bound protons, respectively; $\mathbf{I}$ is the identity; $\mathbf{E_m} = \exp((\mathbf{R} + \mathbf{W})t_m)$ describes off-resonance saturation by the pulse with duration t_m ; $\mathbf{E_s} = \exp(\mathbf{R}t_s)$ and $\mathbf{E_r} = \exp(\mathbf{R}t_r)$ describe longitudinal relaxations during delays before (t_s) and after (t_r) the excitation pulse; $\mathbf{C} = \mathrm{diag}(S^f, S^b)$, where $S^f = \cos(\alpha)$, $S^b = 1$ describe the attenuation of longitudinal magnetizations of free and bound protons by the on-resonance excitation pulse with the flip angle α, respectively; $\mathbf{M_{eq}}$ and $\mathbf{M_{ss}}$ are the vectors of equilibrium and steady-state longitudinal magnetization, and $\mathbf{R}$ and $\mathbf{W}$ are matrices of longitudinal relaxation and saturation defined as follows:

$$\mathbf{M_{eq}} = \begin{bmatrix} 1-f \\ f \end{bmatrix} \qquad \mathbf{M_{ss}} = \frac{1}{D}\begin{bmatrix} (1-f)(A + R_1^F W^B) \\ f(A + R_1^B W^F) \end{bmatrix}$$
$$\mathbf{R} = \begin{bmatrix} -R_1^F - k & k(1-f)/f \\ k & -R_1^F - k(1-f)/f \end{bmatrix} \qquad \mathbf{W} = -\mathrm{diag}(W^F, W^B) \quad [5.2]$$

Where

$$A = R_1^F R_1^B + R_1^F(1-f)/f + R_1^B k \quad [5.3]$$

$$D = A + (R_1^F + k)W^B + (R_1^B + k(1-f)/f)W^F + W^B W^F \quad [5.4]$$

R_1^F and R_1^B are the longitudinal relaxation rate of free and bound spins, respectively; the effective saturation rates of the pools W^F and W^B are calculated from the absorption line-shapes of the pools $g^{F,B}(\Delta, T_2^{F,B})$ and the root-mean-square amplitude of saturation pulse ω_{1rms} averaged over the pulse duration as follows:

$$W^{F,B} = \pi\omega_{1rms}^2 g^{F,B}(\Delta, T_2^{F,B}) \quad [5.5]$$

Where absorption line-shape of the free and bound pools $g^{F,B}(\Delta, T_2^{F,B})$ are defined by the Lorentzian and Super-Lorentzian (or Gaussian for non-biological sample) functions, respectively (44,54).

Therefore, a general form of the SPGR signal for a two-pool MT model with and without MT saturation (S_{MT-ON}, S_{MT-OFF}) can be expressed as:

$$S_{MT-ON} = PD \times M_z^F \sin\alpha \quad [5.6]$$

$$S_{MT-OFF} = PD \times M_z^F(W^B = 0, W^F = 0) \sin\alpha \quad [5.7]$$

Where α is excitation flip angle and *PD* consists of the spin density, instrumental scaling, and the effect of T_2^* decay.

5.2.2 Enhanced 3-pool mCRI Model

The outline of image processing has been previously proposed by the modified cross-relaxation imaging (mCRI) approach (7,53). This approach acquires SPGR data with varying excitation flip angles (α) (VFA) and MT-weighted SPGR data with several combinations of off-resonance frequencies (Δ) and powers (α_{MT}) of MT saturation pulse, which are fit simultaneously to the following signal model to yield bound pool fraction *f*, longitudinal relaxation rate R_1^F, cross-relaxation rate *k*, transverse relaxation time of the bound pool T_2^B, and proton density term *PD*. Therefore, the signal equation can be derived from Eq. [5.6] in the unified format:

$$s = S^{\mathrm{MT}}_{\alpha,\Delta,\alpha_{\mathrm{MT}}}(PD, R_1^{\mathrm{F}}, f, k, T_2^{\mathrm{B}}) \quad [5.8]$$

In the absence of direct saturation due to off-resonance irradiation (Δ>2.5 kHz) (57), the signal from NE pool is independent of Δ and α_{MT} and may be described by a standard single pool SPGR signal equation. As a result, the compartment contributes to the total signal in additive fashion:

$$s = S^{\mathrm{MT}}_{\alpha,\Delta,\alpha_{\mathrm{MT}}}(PD, R_1^{\mathrm{F}}, f, k, T_2^{\mathrm{B}}) + S^{\mathrm{SPGR}}_{\alpha}(PD_{\mathrm{NE}}, R_1^{\mathrm{NE}}) \quad [5.9]$$

Where $PD_{\mathrm{E}} = PD_{\mathrm{F}} + PD_{\mathrm{B}}$, R_1^{F}, PD_{NE}, and R_1^{NE} are proton density and longitudinal relaxation rate of exchanging subsystem and non-exchanging pool, and the SPGR signal for non-exchanging component is defined by

$$S_\alpha = PD\,\frac{1-\exp(-R_1 TR)}{1-\cos\alpha\exp(-R_1 TR)}\sin\alpha \quad [5.10]$$

The resulting NE-mCRI method fits an extended set of VFA and MT measurements to the signal equation to yield all seven parameters describing both exchanging subsystem and non-exchanging pool (figure 5.1). The acquisition protocol consists of acquisition of SPGR data with varying excitation flip angles (α) (VFA) and MT-weighted VFA SPGR data with several combinations of off-resonance frequencies (Δ) and powers (α_{MT}) of MT saturation pulse. These data are fit simultaneously to the unified signal model as described in Eq. [5.9].

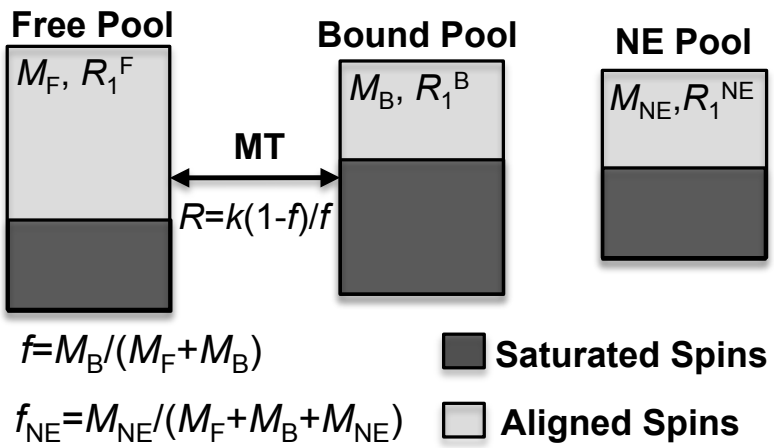

Figure 5.1. Proposed Three-Pool Model. There is a magnetization exchange within exchanging compartment (free pool and bound pool) while there is no magnetization exchange between non-exchanging pool and the exchanging component.

5.3 Materials and Methods

5.3.1 Simulations

To estimate errors in the two-pool model parameters and *MTR* caused by unaccounted partial volume with the non-exchanging component especially in GM, synthetic VFA and MT SPGR signal intensities were generated using the three-pool model (figure 5.1) and equation [5.9] with the pulse sequence parameters of the in vivo study, then the dataset were fit by standard two-pool mCRI model (53). Specific parameters used in the simulation were taken from region-of-interest (ROI) measurements in the thalamus (GM) from (53) (R_1 = 0.71s^{-1}; f = 8.8%; k = 1.57s^{-1}; T_2^B = 10.21 μs).

Additional numerical simulations were used to compare the accuracy and precision in fitting both two-pool and three-pool models over the range of experimental conditions. Theoretical data were generated using the three-pool model (figure 5.1) and equation [5.9] for the range of brain bound pool fraction f (%) = (2, 4, 6, 8, 10, 12, 14, 16, 18, and 20) in the

presence of different amount of non-exchanging fraction NE_f = (0, 0.05, 0.10, 0.15, 0.20, 0.25, 0.30, 0.35, 0.40, 0.45, and 0.50). This provided a 10×11 bound pool fraction (f) vs. non-exchanging fraction (NE_f) grid. For each simulation, 10,000 signals were generated from theoretical data with Gaussian-distributed additive noise. Then, the parameters of each model were estimated by fitting the synthetic data to both two-pool and three-pool models.

5.3.2 Data Acquisition

Imaging experiments were carried out on a 3.0T GE Discovery MR750 (GE Healthcare; Waukesha, WI) using either an eight-channel transmit/receive knee coil (phantom scans) or eight-channel phased array head coil (volunteer scan). All data were acquired with the 3D MT-weighted SPGR sequence in a strong spoiling regime (66) (spoiling gradient area AG5450 mT.ms/m, RF phase increment 169°). The appropriate experimental design was first determined using Monte-Carlo simulations for both phantom and in-vivo experiments. B_0 and B_1 maps were used to correct flip angle and local off-resonance frequency values in both phantom and volunteer studies. B_1 maps were acquired using the optimized actual flip angle imaging (AFI) method ($T_{R,1}/T_{R,2}/T_E$ = 37/185/2.3 ms and α= 55˚, strong spoiling regime) (59). B_0 maps were calculated from the 3D spoiled multi-gradient echo (SPGR) sequence and calculated using IDEAL technique (58).

5.3.3 Phantom Experiment

25% gelatin phantom was scanned in tilted position in respect to the imaging plane to introduce partial volume effect from surrounding water varying along the phantom axis. Z-spectroscopic datasets were acquired using a 3D MT-weighted SPGR sequence with 18 ms - Fermi saturation pulse with different excitation flip angle α and the combination of offset frequencies Δ and effective MT flip angles α_{MT} (α=19˚, Δ=2.5,5,9,13kHz, α_{MT}=[800,1300]˚) and (α=[3,7,40]˚, Δ=2.5,13 kHz, α_{MT} =[800,1300]˚). Additionally, four VFA SPGR datasets were acquired using the same sequence with Δ = 250 kHz (no MT effect at this frequency) and flip angles α= 3˚, 7˚, 19˚, and 40˚. The subset of data at α=7˚, Δ=2.5 kHz, α_{MT}=1300˚ and corresponding SPGR dataset was used to calculate *MTR*. All datasets were acquired with T_R/T_E=37/2.3ms, FOV =140×140×60mm and matrix = 128×128×20.

5.3.4 In-vivo Experiment (Standard Protocol)

The standard mCRI protocol is used in healthy volunteer experiments. Z-spectroscopic datasets were acquired using 18 ms - Fermi saturation pulse (Δ = 2.5, 5, 9, 13 kHz, α_{MT} = 500˚, 1100˚, α=10˚) and (α=[5,20,30]˚, Δ=2.5 kHz, α_{MT} =[785]˚). Four VFA data were acquired with flip angles α= 5˚, 10˚, 20˚, and 30˚. All Z-spectroscopic and VFA data were acquired with T_R/T_E=40/2.0ms, FOV =240×180×80mm and matrix = 128×96×40.

5.3.5 In-vivo Experiment (Optimized Protocol)

The optimized qMT design was determined using Monte-Carlo simulations with less number of measurements. In order to introduce more partial volume with non-exchanging component and better appreciate the effect of partial volume with non-exchanging component

the slice thickness was doubled to 4mm. Five z-spectroscopic datasets were acquired using 18 ms - Fermi saturation pulse ($\Delta/\alpha_{MT}/\alpha$ = 2 kHz/ 1170˚/ 4˚, 2 kHz/ 1170˚/ 14˚, 2 kHz/ 1170˚/ 26˚, 2 kHz/ 600˚/ 14˚, 8kHz / 1170˚/ 14˚) with T_R/T_E=40/2.0ms. Three VFA data were acquired with flip angles α= 4˚, 14˚, and 26˚ with T_R/T_E=23/2.0ms. All Z-spectroscopic and VFA data were acquired with FOV =220×220×176mm and matrix = 150×150×44.

5.3.6 Image Processing

All parametric maps were generated by fitting the VFA and MT data simultaneously to the general signal equation based on the two-pool (Eq. [5.8]) and three-pool (Eq. [5.9]) models using in-house-written C and MATLAB (MathWorks, Natick, MA) software utilizing a standard "*lsqnonlin*" function for nonlinear squares voxel-based fitting.

5.4 Results

5.4.1 Simulations

Figure 5.2 illustrates the level of errors of estimated parameters in gray matter with partial volume effect with non-exchanging component using two-pool model.

As expected, partial volume effect with the non-exchanging component progressively decreases apparent estimates of all qMT parameters and *MTR*. The effect of non-exchanging component on *k* is higher than *f*, *MTR*, and T_2^B. *MTR* and *f* have almost the same level of error in the presence of non-exchanging component while T_2^B is less sensitive to the presence of non-exchanging component. In contrast, as hoped, NE-mCRI corrects partial volume effect errors in all qMT parameters (*f*, *k*, and T_2^B).

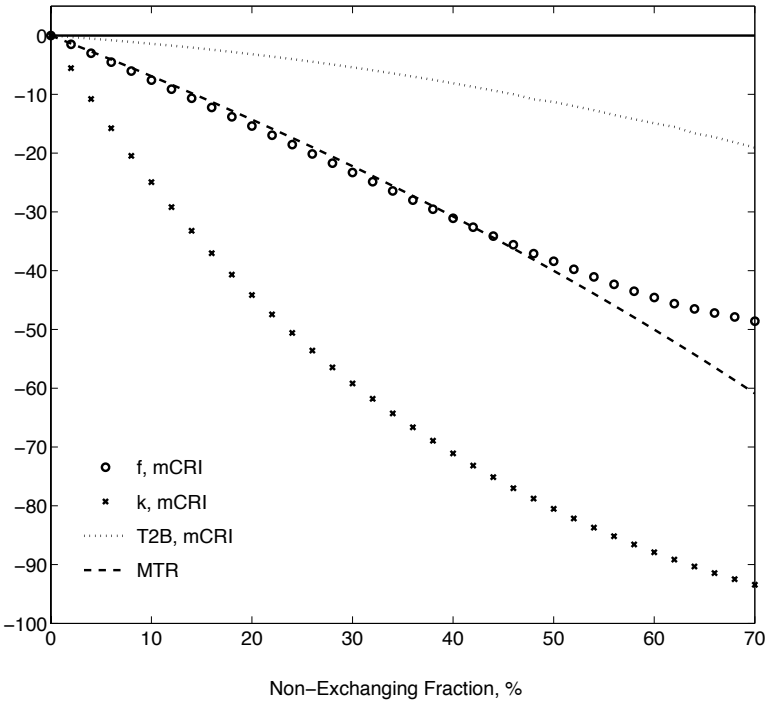

Figure 5.2. Percent error in estimation of MT parameters in the presence of Non-Exchanging pool from numerical simulation.

Figure 5.3 shows the estimated bound pool fraction across the range of f and NE_f values for both mCRI (two-pool model) and NE-mCRI (three-pool model) methods. As expected, mCRI method increasingly underestimates the bound pool fraction as the NE_f increases, while NE-mCRI method correctly estimates the bound pool fraction for the range of NE_f, which can be appreciated by the uniform bound pool fraction estimated for each f for the range of NE_f (across each column). Also this figure contains histograms showing the distribution of the fitted bound pool fraction and non-exchanging fraction for 10,000 simulation realizations for the case of f = 10% and NE_f = 25%. The results show Gaussian distributions for each parameter, centered about the "true" value, suggesting that the algorithm is converging to the same solution repeatedly.

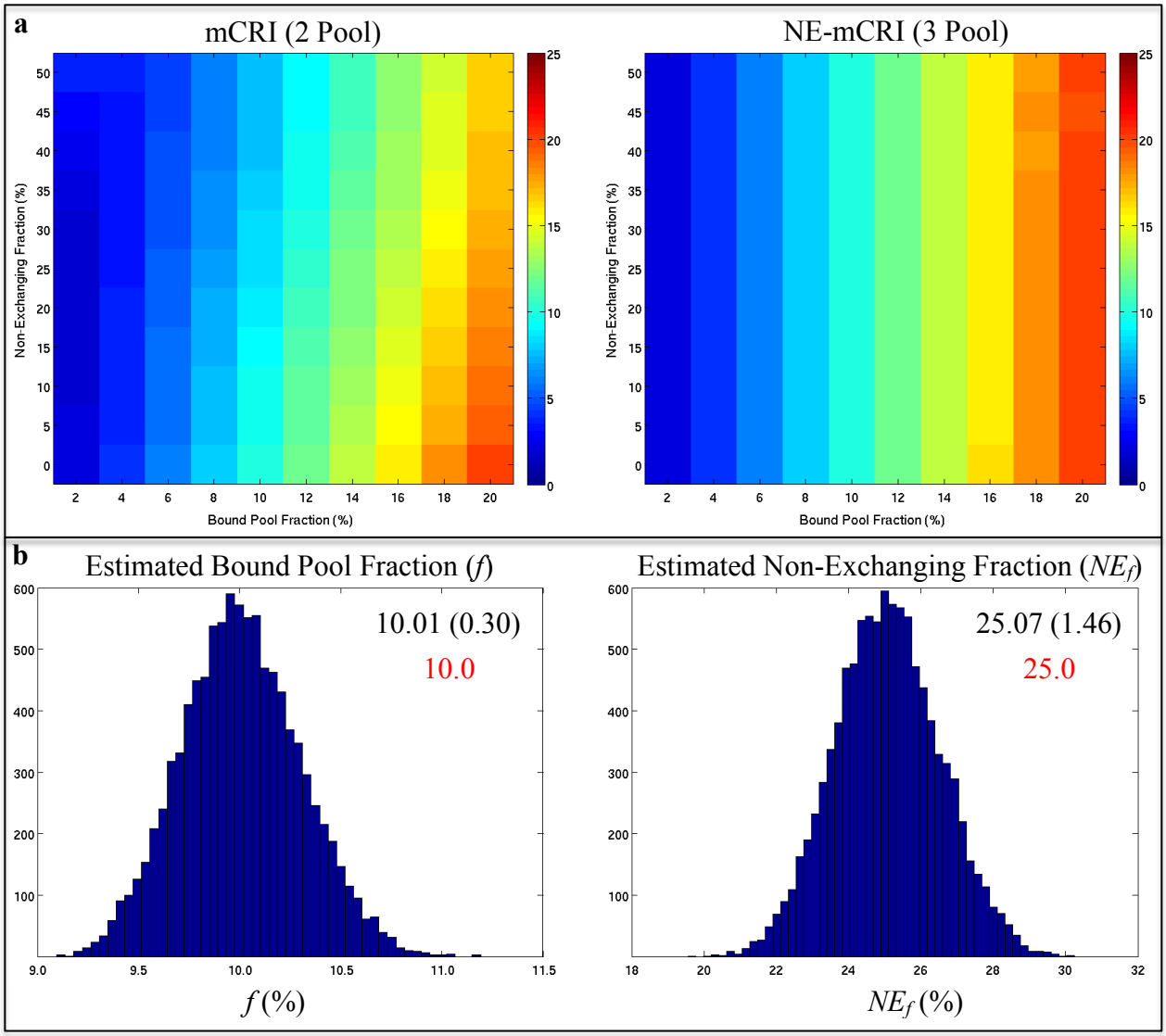

Figure 5.3. Numerical simulation results. a) Comparing mCRI and NE-mCRI models in estimation of the range of bound pool fraction (f) in the presence of non-exchanging component. b) Histogram of estimated bound pool fraction (f) and non-exchanging fraction (NE_f) for the case of f = 10% and NE_f = 25% and mean and standard deviation of estimated parameters [Mean(Std. Dev.)].

5.4.2 Phantom Experiment

Figure 5.4 shows *MTR* and estimated parameters using mCRI and NE-mCRI in the gelatin phantom along the line profile. The NE water fraction estimated by NE-mCRI follows the expected linear dependence along the tilted phantom. These changes are accompanied by

decrease of *MTR* and *f* estimated by standard two-pool model mCRI. NE-mCRI estimate of *f* shows much less variability along the phantom reflecting uniform composition of MT phantom rather than macroscopic partial volume.

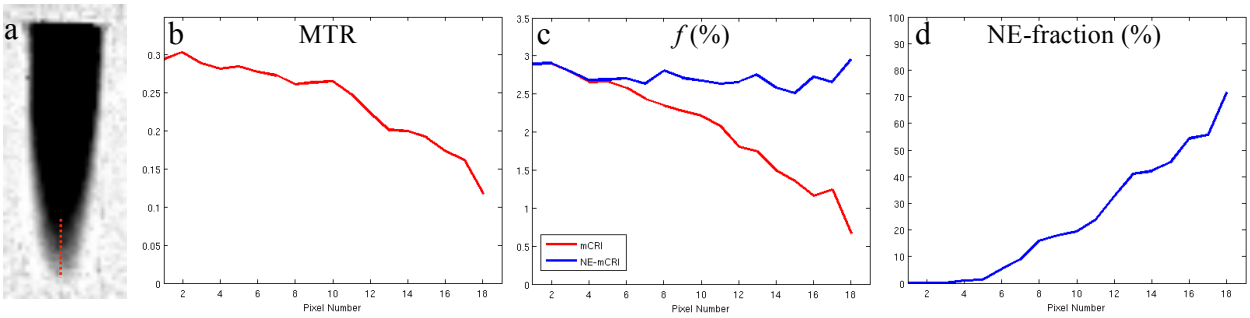

Figure 5.4. **a:** Estimated non-exchanging PVE component with line profile (red) used to track parameters in b,c,d. **b,c,d:** MTR, *f,* and NE (PV) fractions, respectively.

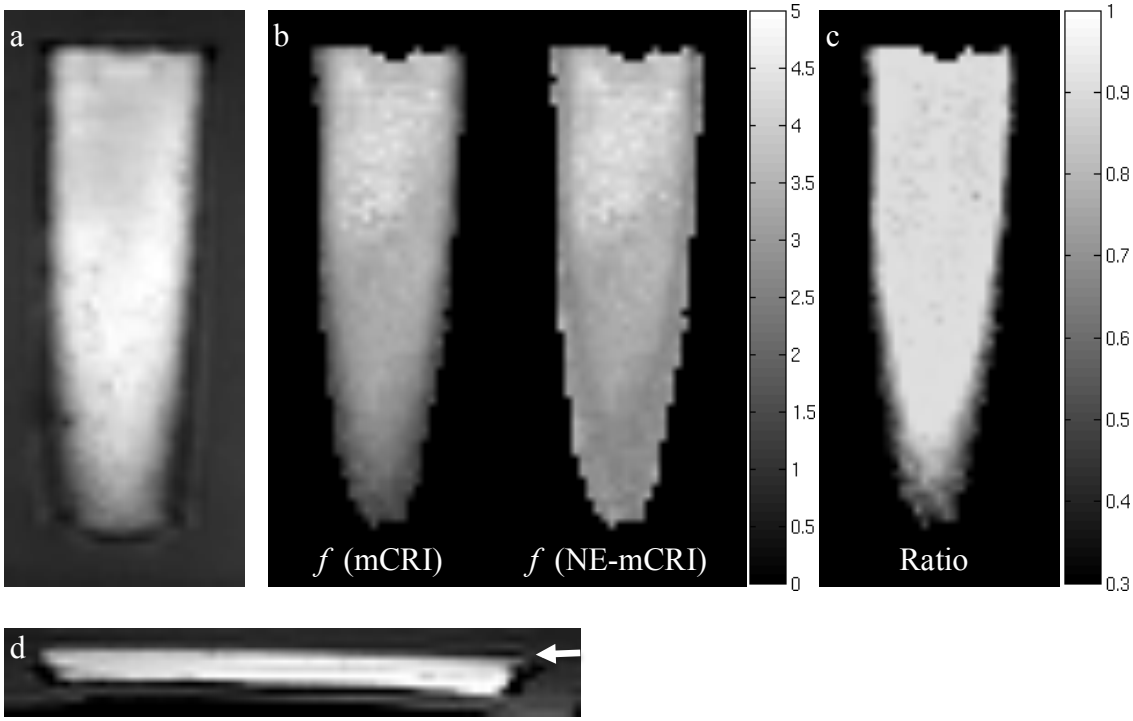

Figure 5.5. a, b: MRI raw image at different plane, white arrow shows the slice shown in quantitative maps. **c**: Bound pool fraction (*f*) estimated from different methods. **d**: The ratio of bound pool fraction maps ($f_{mCRI}/f_{NE\text{-}mCRI}$) maps shows underestimation of mCRI (two-pool model) in peripheral regions of phantoms. The phantom container is masked out in the quantitative maps.

Figure 5.5 shows the bound pool fraction maps estimated with mCRI and NE-mCRI along with the MRI raw image to show the position of phantom and the corresponding slice from the volume. In order to better appreciate the affect of using three-pool model the ratio of bound pool fraction maps ($f_{mCRI}/f_{NE\text{-}mCRI}$) were generated showing the underestimation of bound pool fraction in partial volume pixels (peripheral pixels).

5.4.3 In Vivo Experiment (Standard Protocol)

Figure 5.6 shows that NE-mCRI efficiently decomposes the standard two-pool (*PD*) model into exchanging and non-exchanging terms (PD_E and PD_{NE}), the latter showing high contrast and expected anatomical distribution for CSF. The removal of the CSF component markedly increases the apparent size of GM structures on *f* map in the areas with partial volume effect from CSF (red arrows, bordering the ventricles and CSF). Model preference is quantified in the figure 5.6, which compares mCRI (two-pool model) and NE-mCRI (three-pool model) fit residuals as well as results of a model selection approach using the Bayesian information criterion (BIC, (100)), which shows NE-mCRI approach to be justified over the majority of brain voxels.

The removal of CSF partial volume effect also significantly affects several key qMT parameters in GM (figure 5.7), especially the cross-relaxation rate *k*. The histograms in figure 5.7 demonstrate underestimation in GM *f*, R_1, and *k* values obtained with standard mCRI fit (black arrow). The removal of CSF partial volume effect (shown in figure 5.7) using NE-mCRI removes the bias and corrects the effect of presenting non-exchanging component.

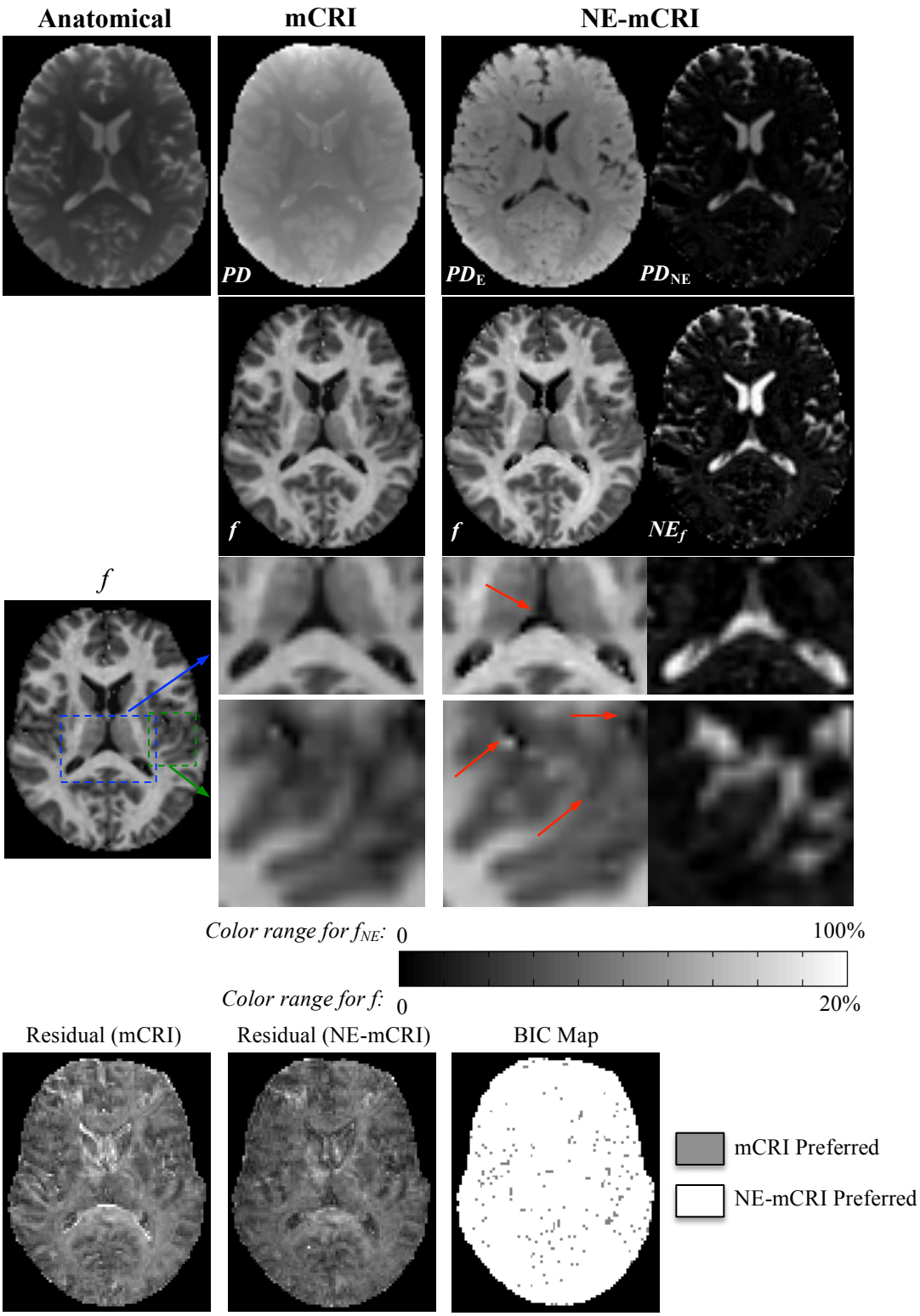

Figure 5.6. First row: Anatomical image and proton density (*PD*) estimated by each method. **Second row:** Bound pool fraction (*f*) estimated by each method and non-exchanging fraction map (NE_f) estimated by NE-mCRI method. **Third and forth rows:** Zoom areas of *f* maps and corresponding NE_f map. **Last row:** Residual maps from each method and BIC map.

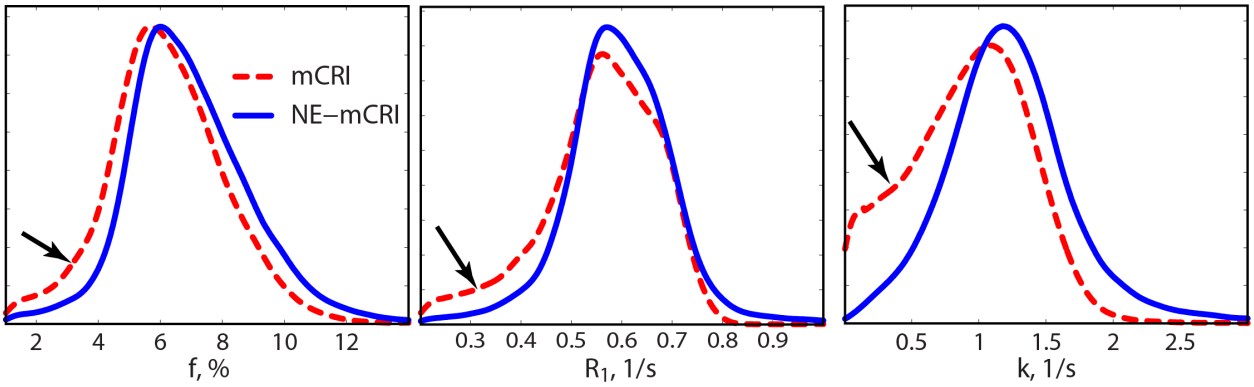

Figure 5.7. GM histograms of key qMT parameters. Arrows point to the histogram areas most affected by CSF partial volume effect.

Further investigation of accuracy of three-pool model in region with and without partial volume effect with CSF is shown in figure 5.8, which shows raw SPGR and MT-weighted SPGR data vs. flip angle and off-resonance frequency curves for intact white matter, gray matter, and partial volume regions of interest (ROIs) and reconstructed two-pool and three-pool model curves. Although insignificant differences are apparent between these two models for intact white matter and gray matter ROIs, both models fit pretty well with the acquired MT and VFA data. In partial volume ROI, mCRI (two-pool model) was not able to fit well to the acquired data while NE-mCRI (three-pool model) still fits pretty well with the acquired data. This observation demonstrates that two-pool model is not adequate to estimate parameters in the presence of non-exchanging components.

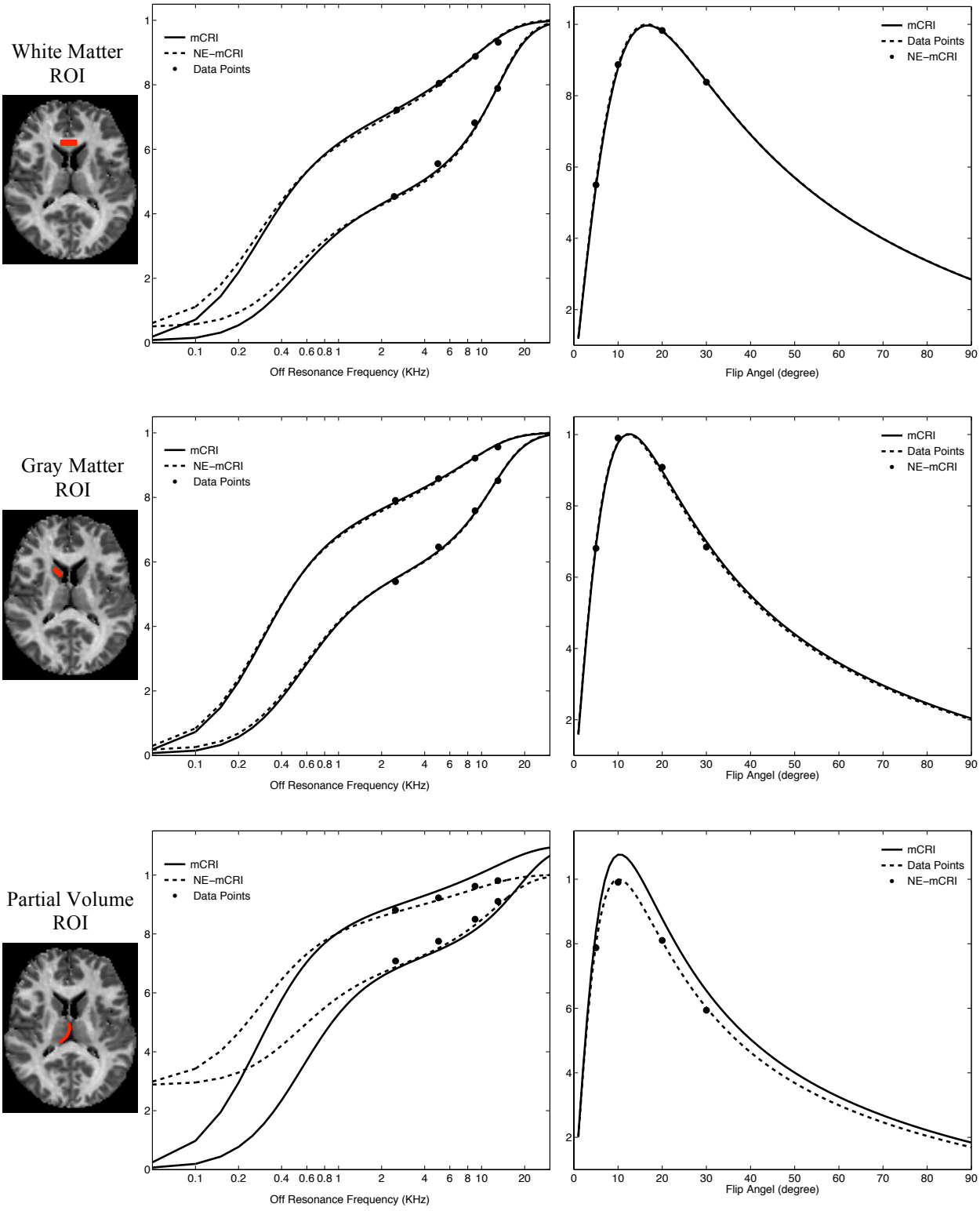

Figure 5.8. Example of SPGR and MT-weighted SPGR raw data and reconstructed two- and three-pool signal curves for intact white matter, gray matter, and partial volume regions. The two-pool model is shown by the solid line, and the three-pool model is shown by the dashed line.

5.4.4 In Vivo Experiment (Optimized Protocol)

The optimized qMT design was determined using Monte-Carlo simulations with less number of measurements. In order to introduce more partial volume with non-exchanging component and better appreciate the effect of partial volume with non-exchanging component the slice thickness was doubled to 4mm.

Figure 5.9 compares the quantitative maps estimated by both mCRI and NE-mCRI. NE-mCRI decomposes the standard two-pool (*PD*) model into exchanging and non-exchanging terms (PD_E and PD_{NE}). PD_{NE} has high contrast and expected anatomical distribution for CSF. The removal of the CSF component can be noticed in all quantitative maps (R_1, f, k, and T_2^B). The correction of partial volume effect with CSF is more appreciated in k map and less in T_2^B, which is in agreement with simulations (figure 5.2). Difference maps between mCRI and NE-mCRI for each quantitative map better shows the effect of correction using three-pool model on partial volume regions. Model preference is quantified in the figure 5.9, which compares mCRI (two-pool model) and NE-mCRI (three-pool model) fit residuals as well as results of a model selection approach using the Bayesian information criterion (BIC, (100)), which shows NE-mCRI approach to be justified over the majority of brain voxels.

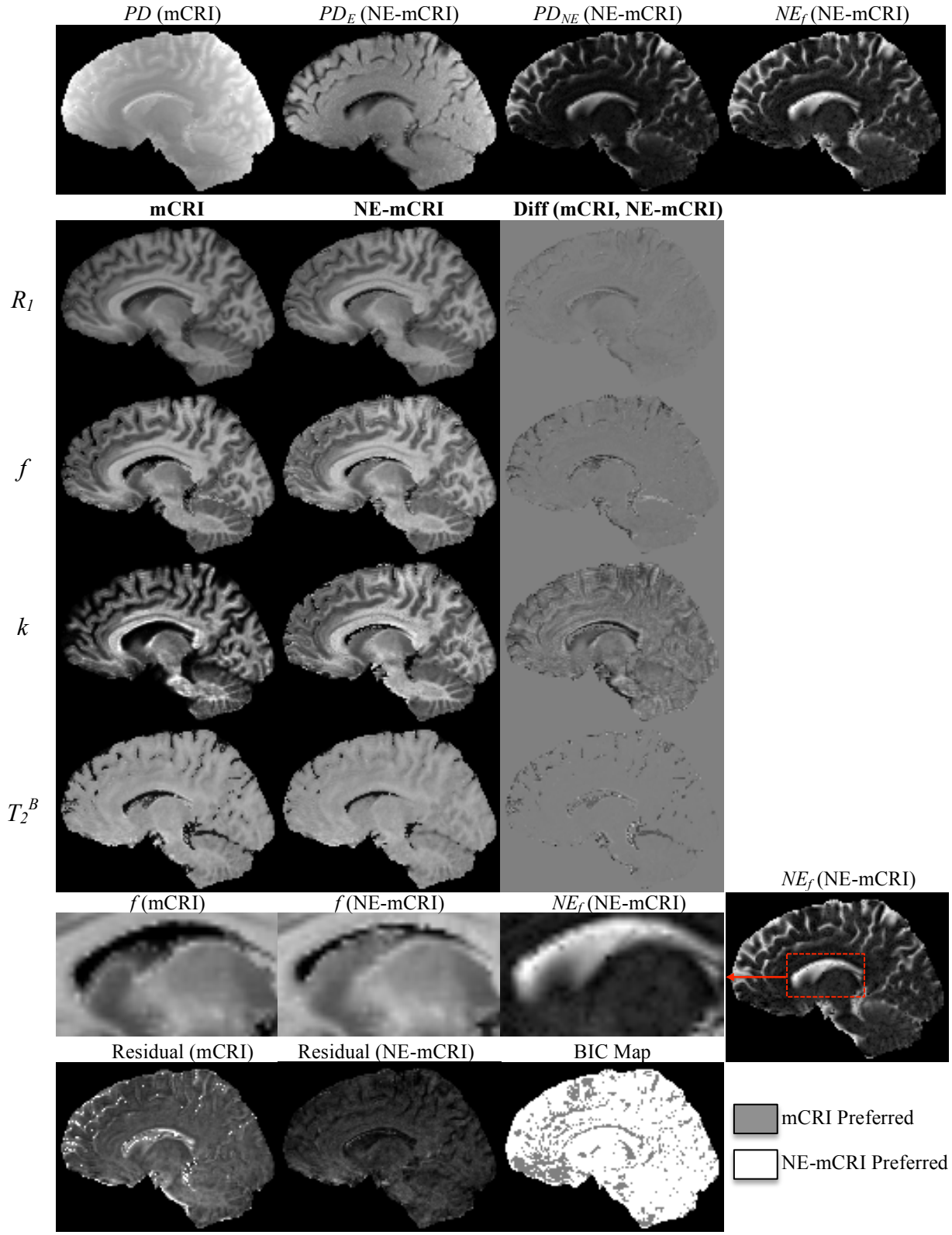

Figure 5.9. First row: *PD* estimated by each method and NE_f map. **Second-fifth rows:** R_1, f, k, T_2^B estimated by each method and the difference map. **Sixth row:** Zoom areas of f maps and corresponding NE_f map. **Last row:** Residual maps from each method and BIC map.

5.5 Discussion

MT imaging offers unique sensitivity to macromolecular content of tissues typically non-accessible with conventional MRI. Accurate modeling of MT exchange processes is essential to yield specific characterization of the macromolecular fraction in both normal and pathological conditions. This study demonstrates that partial volume effect with non- or slowly- exchanging compartments, i.e. CSF influences both *MTR* and key two-pool MT parameters. As partial volume effect with CSF may be significant for gray matter at typical resolutions of quantitative techniques (98,99), CSF may be a serious confounder for MT-based characterization of GM myelination using either *MTR* or *f* potentially affecting both histogram- and voxel-wise analysis.

To compensate this effect, we have proposed a new MT model with an additional non-exchanging compartment (NE-mCRI), which removed CSF (non-exchanging) contamination from brain qMT maps. The biases are elevated for fast single point (constrained) mCRI *f* mapping presumably due to deviations of the apparent cross-relaxation rate in partial volume effect voxels from its assumed constraining value. Our results demonstrate that explicit modeling of partial volume effect using our NE-mCRI approach efficiently corrects the biases due to partial volume effect with CSF in mCRI. Hence, combination of NE-mCRI with the constrained fit may be particularly promising for unbiased *f* mapping in cortical GM in clinically acceptable scan times.

It is not clear now if similar correction is possible for *MTR*, as the proposed approach involves detailed modeling of the MT effect. Our results show higher non-exchanging fraction in WM compared to intact GM. While association of the NE compartment with microscopic structures is yet to be revealed, several interesting observations can be made. WM has many free water compartments associated with axonal, myelin, and extra-axonal water, all described by a

single pool in the standard two-pool model. Myelin water is expected to have the highest rate of MT exchange with macromolecular-rich myelin, mediating MT with other compartments primarily through diffusion at much lower rates. Hence, the NE pool may be considered as an approximation to such more slowly exchanging compartments.

Finally, the NE-mCRI may enable direct estimation of partial volume effect with CSF and circumvent assumptions of image-based estimation of PVE during segmentation. The direct estimation of partial volume effect may be potentially useful to improve accuracy of brain atrophy measurements in multiple sclerosis and Alzheimer disease, and in older patients who often have enlarged perivascular spaces and/or chronic lacunar infarcts filled with CSF. With the feasibility of in vivo imaging, NE-mCRI may improve existing tradeoffs with 4-pool models and provide more accurate characterization of WM. Additionally, it has potential to improve accuracy of qMT in edematous conditions or in fat (non-exchanging) liver.

Chapter 6: Applications of Quantitative Magnetization Transfer Imaging

6.1 Introduction

In previous chapters, we have discussed the principle of the quantitative magnetization transfer (qMT) imaging and how to determine the parameters of two-pool model using qMT imaging. This chapter will focus on the clinical application of qMT imaging method in brain and knee imaging. One of the main applications of qMT imaging is on myelin imaging. Many studies have shown the great sensitivity and specificity of qMT parameter to the myelin content in the central nervous system (13-17). Therefore, this chapter will begin with an introduction to myelin and myelin related diseases and then we will discuss the application of MT methods in myelin imaging.

6.2 Myelin and Multiple Sclerosis

Neurons in brain continually send and receive signals through axons, which are protected by a type of insolation called myelin sheath (figure 6.1).

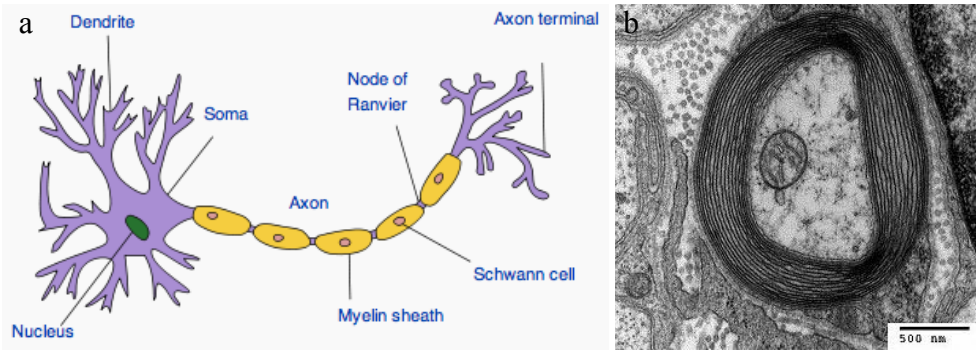

Figure 6.1. Structure of a typical neuron (http://en.wikipedia.org/wiki/Neuron.) (**a**), Transmission electron micrograph of myelinated axons generated at Trinity College, Hartford, CT (**b**).

Myelin sheaths are an extension of a glial plasma membrane layers wrapped around the axon of nerve fibers that facilitate conduction and accelerate the propagation of electric impulses (101). In multiple sclerosis (MS), these myelin sheaths are eroded (demyelination) and the underlying nerve fiber could also be damaged due to mistaken attack by immune system (figure 6.2). This leads to a failure in the ability of nerve cells to transmit signals and causes symptoms that can range from numbness and tingling to blindness and paralysis. MS is a complex disease that is highly variable in symptoms, clinical course, and underlying pathological changes in neural tissues.

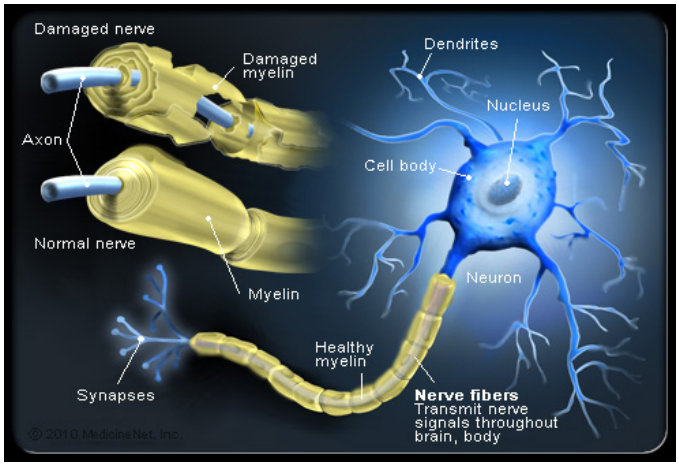

Figure 6.2. Structure of a normal nerve fiber and damaged nerve in multiple sclerosis (http://www.medicinenet.com/image-collection/)

The estimated total economic cost of MS to the U.S. is between $6.8 to $11.9 billion annually (102) and the annual healthcare cost for each MS patient is between $8,528 to $54,244 (2013 data) (103). An early detection of the inflammatory process at early stages enables patients to begin the treatment, which can hinder the degenerative progression of MS. Therefore; new diagnosis and treatment approaches are continuously being sought. Since its introduction by Young et al. (104), MRI has become an important diagnostic tool providing noninvasive

evidence of MS lesions in the central nervous system (CNS). Lesions that are hyperintense on T_2-weighted scans can be seen in the brains of more than 95% patients with established MS (105-108), and active lesions are enhanced on T_1-weighted scans after the administration of gadolinium contrast (109). Areas of permanent tissue damage (e.g., irreversible demyelination and axonal loss) may be identified as profound hypointense regions on T_1-weighted scans without administration of gadolinium contrast (110,111).

Unfortunately, conventional MRI correlates poorly with clinical disability (112-117) and its prognostic value is very limited (112,113,117-122), and it has limited sensitivity and specificity to the pathological substrates of MS including demyelination, re-myelination, inflammation, edema, and axonal damage. Various MRI methods such as magnetization transfer (1-12), diffusion MRI (25,26,28,123), and multicomponent relaxometry (29,31,33,35) have been proposed to characterize white matter (WM) tissue properties specifically the myelin content. Among these methods, quantitative magnetization transfer (qMT) imaging shows promising results in assessing the myelin content (13-16).

6.3 MT Imaging Reveals Severe Demyelination in Cats on Irradiated Diet

6.3.1 Introduction

Cats fed an irradiated diet develop a profound, widespread demyelinating disease of the CNS with severe neurologic dysfunction, including development of ataxia, paresis/paralysis, and blindness (124). There is no confounding inflammation or axonal loss in this animal model, making it a good model for investigating the myelin content in the brain. Several quantitative MRI methods have been proposed to measure the myelin content and axonal density of brain tissues. In this study, we report results from Magnetization Transfer (MT) imaging (19) on cats fed an irradiated diet. MT indirectly detects macromolecular associated hydrogen nuclei via their magnetic interaction with the observable water. In the normal CNS, white matter exhibits the largest MT effect due to the macromolecular content of the highly structured and lipid rich myelin. Pathologies that alter the structural integrity and the relative macromolecular-water composition show abnormal MT (125).

6.3.2 Materials and Methods

In this study a new and unique large animal model is being used to answer unresolved questions on endogenous remyelination of the CNS (124). One control cat and one diseased cat, which was fed a diet of irradiated dry food, and after being off the diet (Recovery stage) were scanned on a 3.0T GE Discovery MR750 (GE Healthcare; Waukesha, WI) using an HD knee coil. Two 3D spoiled gradient echo (SPGR) scans were acquired at TR/TE = 18/3.3 ms with different flip angles (4˚, 30˚), and two MT-weighted 3D gradient echo (SPGR) scans were acquired with TR/TE = 28/3.3 ms, $\alpha = 10^{\circ}$, one with an MT pre-pulse (Fermi shape, 3 kHz offset frequency, effective flip angle of 790˚), and one with different offset frequency (200 kHz) to have no MT effect. The matrix size was 192×192×56. Two measures of MT effect, the

magnetization transfer ratio (*MTR*) and magnetization transfer saturation (*MT-Sat*) (51) were calculated as a percentage of signal loss, and the additional saturation due to MT effect respectively.

6.3.3 Results

It took 3-4 months for cats on the irradiated diet to develop clinical signs. If returned to a non-irradiated diet, the disease cat recovered gradually to the healthy condition. At the height of the acute disease, there was a widespread vacuolation of myelin, myelin breakdown and extensive demyelination, especially in the optic nerves but also along the entire spinal cord and multifocally in the brain (figure 6.3).

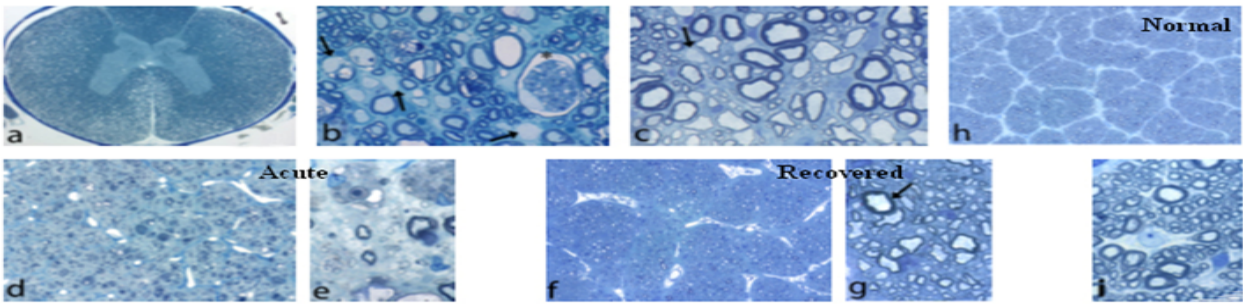

Figure 6.3: a) Spinal cord from a cat at peak of disease. The lateral and ventral columns show extensive vacuolation. **b)** At higher power, numerous axons are undergoing myelin degeneration (*) but the axon is intact. Numerous demyelinated axons (arrows) and remyelinated axons (thin myelin sheaths) are present. **c)** In the recovered cat spinal cord numerous remyelinated axons are present (thin myelin) with no loss of axons. **d, e)** In the optic nerve in acute disease there is widespread demyelination with only occasional preserved sheaths. **f, g)** In the recovered cat there is complete remyelination with almost all axons having thin myelin sheaths (g) except for one axon with normal thickness sheath (arrow). In the control cat **(h, i)** the normal pattern of myelination in the optic nerve is seen (Results from (107)).

Figure 6.4 is the representative coronal slices of *MT-Sat* maps for the control cat, diseased cat at the peak of the disease and the recovery stage.

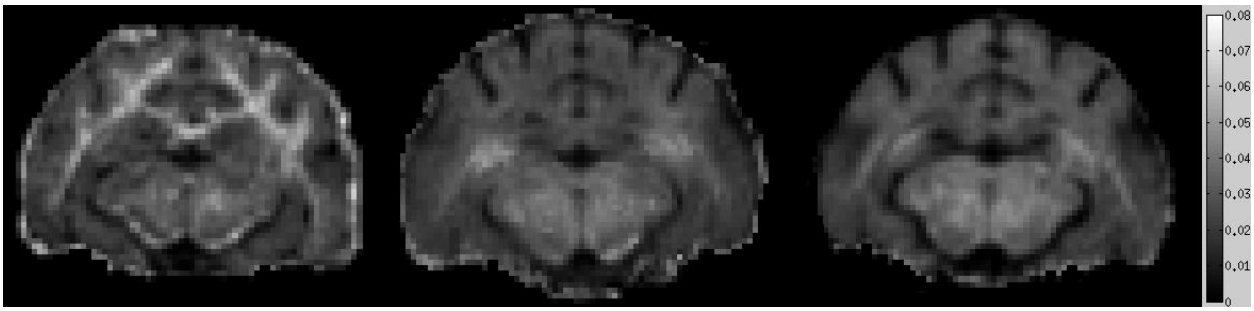

Figure 6.4: *MT-Sat* maps for control cat (left), diseased cat (middle), and recovered cat (right). *MT-Sat* is significantly decreased in WM of the diseased cat, leading to the loss of contrast between WM and GM in diseased animal compared to control.

Table 6.1 and Figure 6.5 represent the *MTR* and *MT-Sat* results from different white matter ROIs (periventricular (PV), pyramidal tract (PT), and subcortical (SC)). *MTR* and *MT-Sat* are sensitive to the amount of myelination, hence they are visibly decreased in white matter of the diseased cat compared to the control, while the increase in these parameters can be appreciate in the recovery stage compared to the peak of the disease.

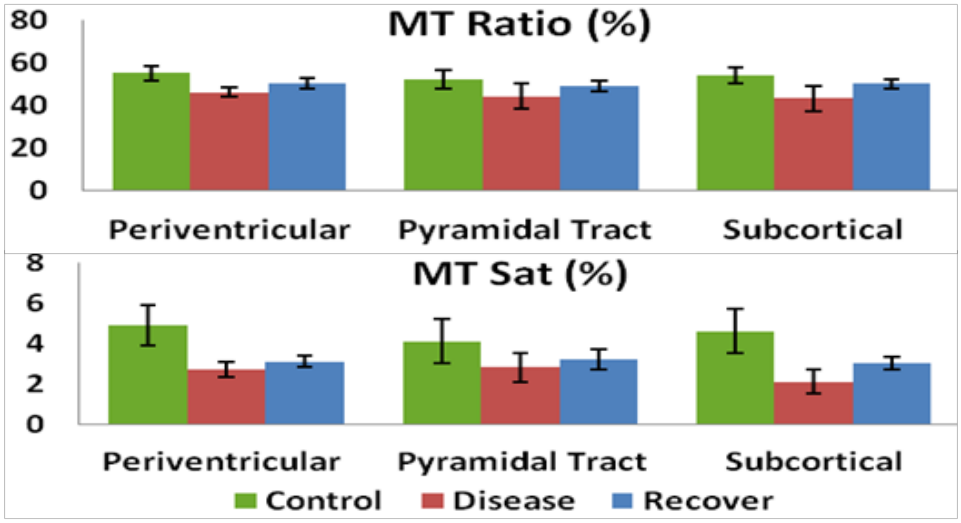

Figure 6.5: Mean MTR and MT-Sat from WM ROIs.

Table 6.1: Mean *MTR* and *MT-Sat* from WM ROIs.

	Control			Diseased			Recovered		
ROI	**PV**	**PT**	**SC**	**PV**	**PT**	**SC**	**PV**	**PT**	**SC**
***MTR* (%)**	55 3.5	52 4.3	54 3.7	46 2.4	44 6.0	43 5.8	50 2.5	49 2.7	50 2.1
***MT-Sat*(%)**	4.9 1.1	4.1 1.0	4.6 1.2	2.7 0.4	2.8 0.7	2.1 0.6	3.1 0.3	3.2 0.5	3.0 0.3

Compared to *MTR*, *MT-Sat* shows more significant discrimination between all disease stages confirmed both qualitatively (figure 6.4) and quantitatively (figure 6.5, Table 6.1). In the control animal, there is a significant contrast between white matter and gray matter, while this contrast is not noticeable in the diseased cat at both the peak of the disease and the recovery stage. MT imaging also reveals spatial heterogeneity of demyelination level in the diseased cat (figure 6.4). These results are consistent with anatomical maps from T_2-wieghted images (figure 6.6), showing the loss of contrast between WM and GM for the diseased cat.

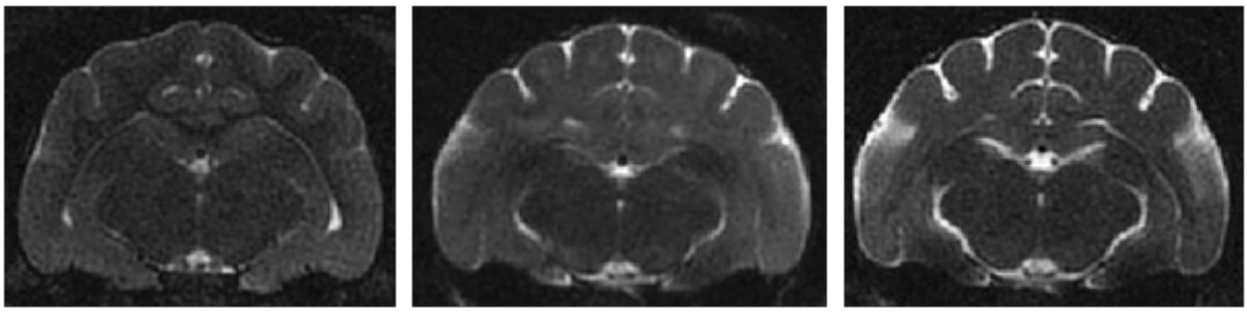

Figure 6.6: T_2-weighted images for control (left), diseased (middle), and recovered (right) cats. High contrast between WM and GM is noticeable in control animal.

6.3.4 Conclusions

The irradiated diet is a novel feline animal model featuring both demyelination and remyelination. There was no confounding effect of inflammation and axonal loss in this animal study, making it a good model for investigating the myelin content in the brain. Markedly reduced *MTR* and *MT-Sat* in the diseased cat reflects the degeneration of myelin characteristic of

this animal model and increase of these parameters in the recovery phase reveals the remyelination process. MT imaging also shows the spatial heterogeneity of the as-yet poorly understood disease process, making it a useful tool for further study in this novel animal model. *MT-Sat* measures were more discriminative between different disease stages than *MTR*, which may imply more specific nature of *MT-Sat* measure.

6.4 Quantitative MRI Analysis of MS Patients vs. Healthy Control

6.4.1 Introduction

Quantitative MTI promises new ways to characterize MS disease burden and predict the development of MS lesions through sensitive and truly quantitative, noninvasive biomarkers. Over the past few years, bound pool fraction (f) has become a center of attention as a potential biomarker of myelin in brain tissues. QMT imaging showed that the bound pool fraction is greater in white matter than in gray matter (126), and smaller in MS lesions than in normal white matter (2), which suggests that bound pool fraction is capable of reflecting myelin contents in tissue. However, clinical applications of bound pool fraction mapping have been hindered due to the absence of fast and accurate qMT imaging. In our study, the optimized qMT imaging with less number of measurement and new fast bound pool fraction mapping based on single MT measurement (9) have been utilized along with other establish MRI methods such as *MTR*, T_1, and DTI for brain characterization in MS patients.

6.4.2 Materials and Methods

This study is longitudinal study involving 18 relapsing-remitting MS patients and 12 healthy control subjects. MS patients have a neurological examination before MRI scan. Neurological status is reported as the Expanded Disability Status Scale (EDSS) and Multiple Sclerosis Functional Composite (MSFC). In the first phase of study, MS patients had EDSS range 1.0-5.0. MRI data includes pre- and post-contrast anatomical images (BRAVO, T_2-FLAIR), IDEAL (B0 mapping and R_2* for quantifying iron content in tissue), DTI (25 directions), AFI (B1 mapping), 4 MT weighted data (α=13˚, Δ(kHz)/α_{MT}(˚) = [2.5/1150 ,2.5/550 ,5/650 ,11/1150], TR/TE = 40/3.4ms), and 2 SPGR data at flip angles α= [5˚, 30˚], TR/TE = 30/4.7ms. All images were coregistered to high resolution BRAVO ($0.86\times0.86\times1.5$ mm^3) using

a brain extraction tool and rigid body coregistration (BET and FLIRT, FSL, Oxford, UK). Anatomical data were intensity corrected using Jim software (Xinapse systems, Aldwincle, UK). Brain segmentations were done on BRAVO using FSL software (FSL, Oxford, UK) with FAST automated single-channel procedure applying three classes of tissue for healthy control brains and four classes of tissue for MS patients.

MS lesions were independently segmented from T_2-FLAIR images by the region-growing semi-automated algorithm using Jim software (Xinapse Systems, Aldwincle, UK). Since MS lesions potentially can fall into any tissue class during brain segmentation, lesion masks were excluded from WM and GM masks obtained by FSL, thus providing masks of normal appearing brain tissues. DTI data were corrected for eddy-current distortion prior to coregistration to BRAVO images and then processed using FSL software (FSL, Oxford, UK). Flip angle (B1) and field (B0) maps were measured by AFI (59) and IDEAL (58). Parametric maps were generated from both mCRI (53) and fast single-point (9) methods. *MTR* maps were generated with the correction of B1 errors (49). MT saturation maps (51) were generated using SPGR data and one MT data with the highest MT power.

6.4.3 Results

Figure 6.7 shows the example of different maps obtained from an MS patient. BRAVO data is used for brain segmentation using FSL software, and T_2 lesion maps is generate from T_2-FLAIR data by Jim software.

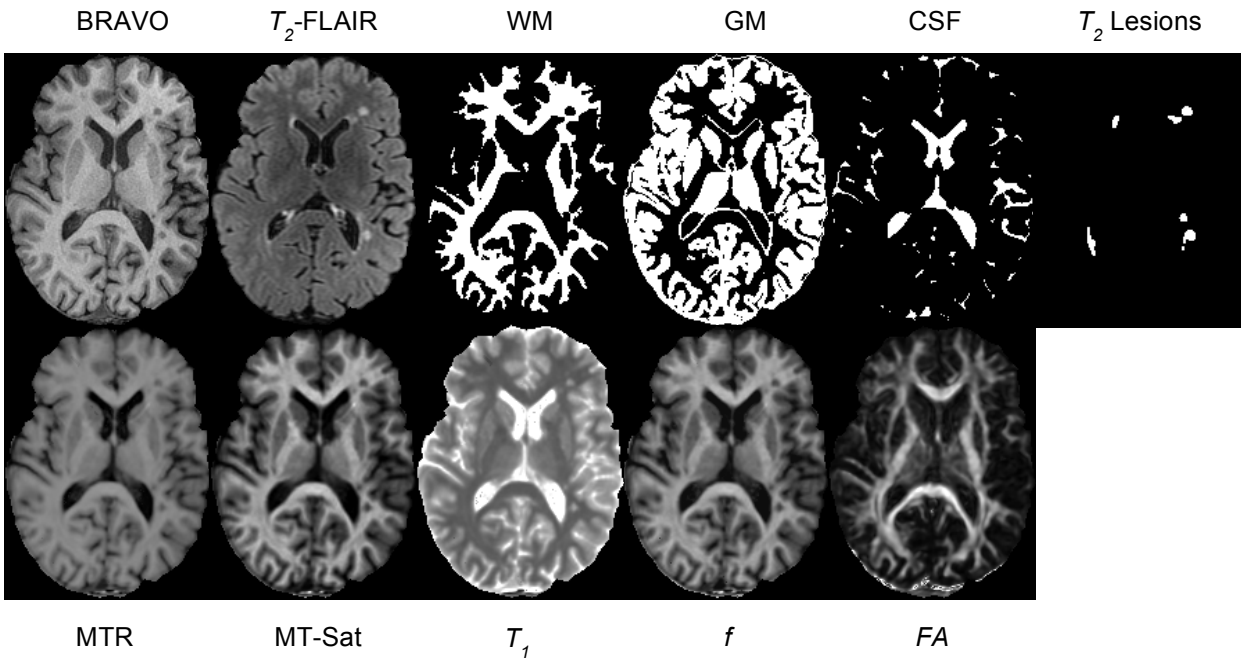

Figure 6.7. Example of anatomical images, segmented normal appearing WM, normal appearing GM, CSF, lesion masks, MT ratio (MTR), MT saturation (MT-sat), T_1, bound pool fraction (f), and fractional anisotropy (FA) maps obtained from an MS patient.

Mean parameters values (± standard deviation) in segmented brain tissues are listed in Table 6.2.

Table 6.2. Group comparison between imaging parameters in tissues.

Parameter	Normal Appearing White Matter			Gray Matter		Lesion
	Control	MS	Effect Size (%)	Control	MS	MS
FA	0.46±0.014	**0.44±0.021***	4.44	0.17±0.008	0.17±0.008	0.28±0.031
AD	$1.14\times10^{-3}\pm1.95\times10^{-5}$	**$1.17\times10^{-3}\pm2.54\times10^{-5}$ *****	-2.60	$0.98\times10^{-3}\pm2.46\times10^{-5}$	$0.98\times10^{-3}\pm4.09\times10^{-5}$	$1.53\times10^{-3}\pm1.05\times10^{-4}$
RD	$5.38\times10^{-4}\pm1.81\times10^{-5}$	**$5.70\times10^{-4}\pm2.98\times10^{-5}$ ****	-5.78	$7.55\times10^{-4}\pm1.29\times10^{-5}$	$7.60\times10^{-4}\pm5.86\times10^{-5}$	$10.1\times10^{-4}\pm9.29\times10^{-5}$
MD	$7.39\times10^{-4}\pm1.65\times10^{-5}$	**$7.71\times10^{-4}\pm2.57\times10^{-5}$ *****	-4.24	$8.29\times10^{-4}\pm1.65\times10^{-5}$	$8.34\times10^{-4}\pm3.55\times10^{-5}$	$11.8\times10^{-4}\pm9.36\times10^{-5}$
MTR	0.530±0.007	**0.524±0.017 *****	1.14	0.400±0.001	0.405±0.012	0.409±0.0241
MTS	$6.31\times10^{-2}\pm2.37\times10^{-3}$	**$5.98\times10^{-2}\pm3.98\times10^{-3}$ ****	5.37	$2.97\times10^{-2}\pm0.88\times10^{-3}$	**$3.18\times10^{-2}\pm1.18\times10^{-3}$ *****	$3.53\times10^{-2}\pm3.84\times10^{-3}$
R_1 (s^{-1})	0.808±0.026	0.783±0.051	3.14	0.521±0.017	0.531±0.027	0.592±0.040
f (%)	12.4±0.39	**11.5±0.71 *****	7.53	6.43±0.16	**6.57±0.022 ***	7.18±0.72
T_2^B (μs)	11.2±0.24	11.3±0.30	-0.89	9.87±0.39	**10.7±0.73 *****	10.3±0.56

Comparison with control: *P<0.05, **P<0.01, ***P<0.001

Mean parameter values computed within each tissue mask were compared between control subjects and MS patients using independent two-tailed t-tests. Significant changes in the value of all parameters except T_1 and T_2^B can be seen in normal appearing white matter between two groups, while the significant changes in value of parameters for normal appearing gray matter can be seen only in MT-saturation (*MT-Sat*), bound pool fraction (f), and T_2 of bound pool (T_2^B). Furthermore, the effect size of each parameter in normal appearing white matter were calculated to quantify the difference between control and MS patient using each parameter, which is defined as

$$Effect\ Size(X,Y) = \frac{mean(X-Y)}{0.5\times mean(X+Y)}\times 100\% \qquad [6.1]$$

6.4.4 Discussion

The new fast and accurate qMT imaging with less number of measurement and new fast bound pool fraction mapping based on single MT measurement (9) have been utilized along with other establish MRI methods such as *MTR*, T_1, and DTI for brain characterization in MS patients. The initial result of this ongoing study shows that bound pool fraction (f) has higher sensitivity in differentiating the normal appearing white matter for the lesion comparing to other parameters including *MTR*, T_1, and DTI results. Next step of qMT-MS study is to compare the parameters between two groups in different white matter regions of interest (ROIs) and find the correlation between these parameters, lesion volume, and the neurological exam scores. Therefore, MNI152 standard-space T_1-weighted template from FSL is coregistered to BRAVO image of each subject using affine coregistration by FSL, and the transform matrices are applied to DTI-based white matter ROIs (Laboratory of Brain Anatomical MRI, Johns Hopkins University).

6.5 Factors Influencing QMT Parameters of Articular Cartilage

6.5.1 Introduction

Osteoarthritis is one of the most prevalent chronic diseases in the United States and worldwide, which is characterized by a loss of proteoglycan content and disruption of the highly organized collagen fiber network of articular cartilage (127-129). Early detection of osteoarthritis is important for slowing down or even stopping the disease progression (130,131). Thus, there is need to develop new and improved non-invasive methods to identify patients with early osteoarthritis and to monitor disease-related and treatment-related changes of articular cartilage in osteoarthritis research studies.

Magnetization transfer (MT) may provide information about the macro molecular content (i.e. collagen and proteoglycans), but standard MT ratio (*MTR*) is a pulse sequence-dependent composite and it is not specific to any particular cartilage components. Quantitative magnetization transfer (qMT) imaging can be used to probe macromolecular tissue composition typically non-accessible by conventional MRI techniques (132).

Cross-relaxation imaging (CRI), an efficient qMT approach, yields unique measures including the fraction of protons bound to macromolecules (*f*), the cross-relaxation (exchange) rate between water protons and bound protons (*k*), and the transverse relaxation time of macromolecular bound protons (T_2^B) (7) and has been applied for qMT parameter mapping in human patellar cartilage in vivo at 3.0T with a scan time under 30 minutes (133). Several studies reported that qMT parameters are correlated with macromolecular content in ex-vivo cartilage samples (134,135) and change with age and activity level in human patellar cartilage in-vivo (133). However, the mechanisms responsible for changes in qMT parameters with cartilage degeneration remain unknown. Thus, this study was performed to investigate the factors leading

to changes in qMT measures of cartilage in controlled conditions including phantom experiments and an ex-vivo bovine cartilage degradation model.

6.5.2 Materials and Method

Magnetization Exchange Model in Articular Cartilage: Articular cartilage is a highly complex and dynamic tissue. Recently, the magnetization exchange within the collagen-bulk-water, proteoglycan-collagen, and the collagen fibrillar water-collagen cartilage subsystems were modeled and quantified (figure 6.8) (136). It has been shown that the magnetization exchange rates for proteoglycan-collagen and collagen fibrillar water-collagen were $120s^{-1}$ and $4.4s^{-1}$, respectively (136), which shows a strong magnetization exchange rate between the matrix molecules (collagen and proteoglycan) and an intermediate magnetization exchange rate between collagen fibrillar water and collagen.

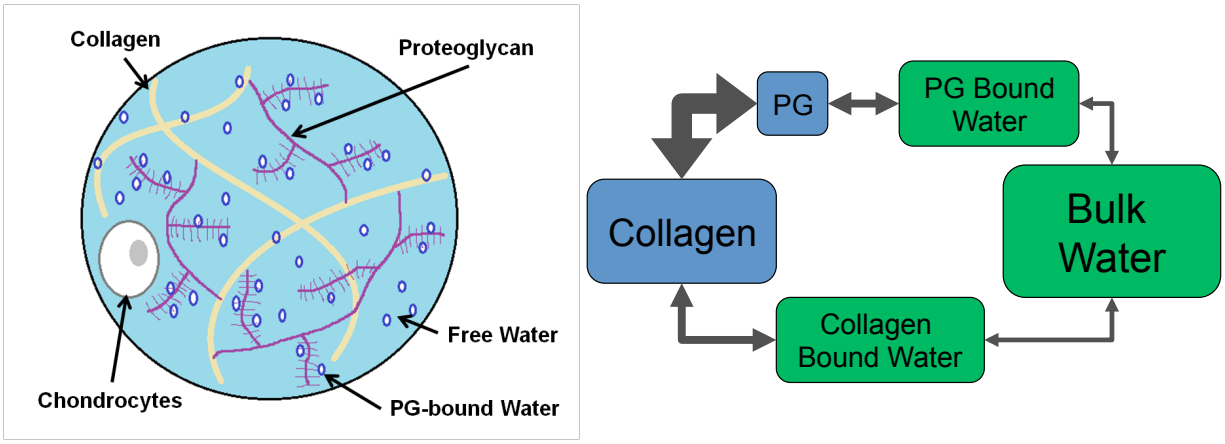

Figure 6.8. Left: Extracellular matrix of collagen with different classes of proteins such as collagen and proteoglycan. **Right**: The model of magnetization exchange between different subsystems of cartilage. The width of arrows represents the magnetization exchange rates between these subsystems.

Estimation of all parameters of this model is not feasible in clinical MRI so we can simplify this complex model to the two-pool model with reasonable approximation (figure 6.9).

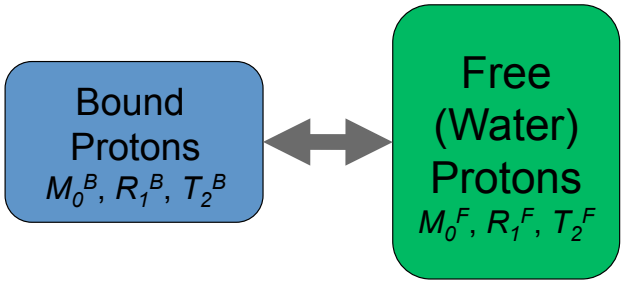

Figure 6.9. Two-pool model approximates the magnetization exchange within articular cartilage complex system.

6.5.3 Phantom Studies

Phantom solutions containing 5% to 25% collagen and proteoglycan (PG) were prepared by dissolving bovine Achilles tendon type 1 collagen and bovine trachea chondroitin sulfate (Sigma-Aldrich, St. Louis, MO) respectively in saline. The second set of phantom solutions containing 20% collagen were prepared in the same manner and heated at temperatures ranging between 20ºC and 100ºC for 30 minutes. This heating protocol was shown in previous studies to cause incremental increases in denaturation of type 1 collagen solution starting at threshold temperatures between 50ºC and 60ºC (137).

6.5.4 Ex-Vivo Bovine Cartilage Study

A fresh bovine patella specimen was excised from a skeletally mature cow. A transverse cut was made through the cartilage and bone separating the patellar specimen into superior and inferior halves, which allowed one portion of the cartilage to be immersed in 25 mg/ml of trypsin solution and the other portion to be immersed within saline solution for 24 hours with antibiotics added to both solutions (figure 6.10).

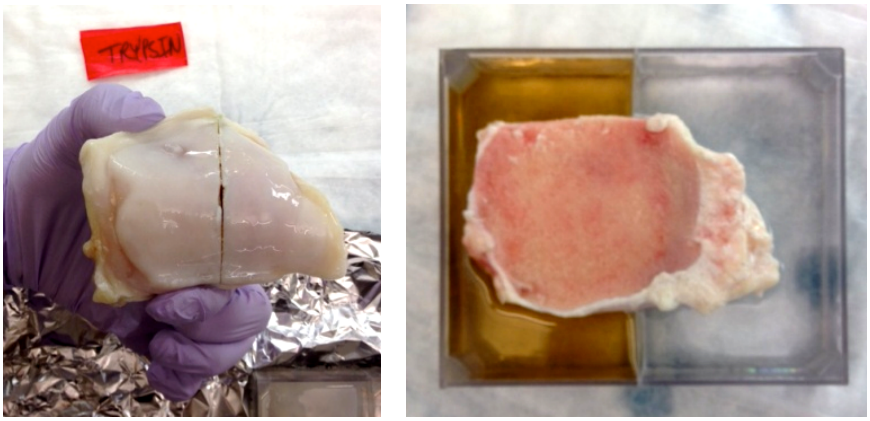

Figure 6.10. Ex-vivo proteoglycan degradation experiment. Transverse cut of specimen into superior and inferior portions. One portion immersed in 25mg/ml trypsin, the other portion in saline for 24 hours.

6.5.5 Data Acquisition

All phantoms and the bovine patellar cartilage specimen before and after enzymatic degradation were placed in a container filled with saline solution and imaged on a 3.0T scanner (Discovery MR750, GE Healthcare; Waukesha, WI) using an single-channel wrist coil. For the phantom study, variable flip angle (VFA) SPGR data were acquired at excitation flip angles (FA) α=[4,6,15,25,35,50]˚ and MT-weighted SPGR data were acquired at α=15˚ for several off-resonance frequencies Δ=[2.5,4,6,8,10,12,14,18,20,22] kHz and MT saturation powers α_{MT}=[850,1300]˚ with TR/TE=37/2.1ms and 1.5×1.5×2 mm^3 voxel size. For the bovine cartilage study, VFA data were acquired at FAs α=[4,10,20,30]˚ and MT-weighted data were acquired (α=13˚, Δ(kHz)/α_{MT}(˚)=2/750,2/1550,5/750,11/1350,13/1250,13/1350,20/1550,21/950) with TR/TE=41/3.8ms and 0.5×0.5×3 mm^3 voxel size. Spatially varying flip angle (B1) map was measured by AFI (59) for subsequent flip angle corrections.

6.5.6 Data Processing

The qMT processing workflow was implemented according to (53) (figure 6.11). All processing has been done by in-house-written C and MATLAB (MathWorks, Natick, MA) software using nonlinear least squares fitting.

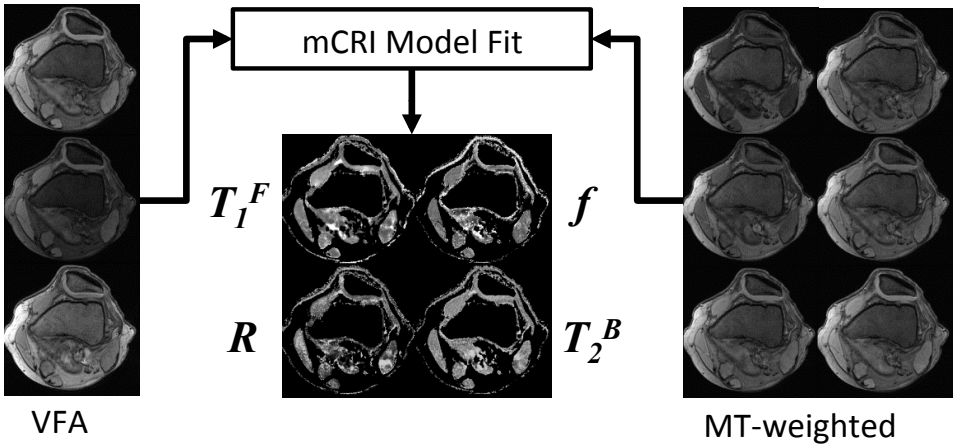

Figure 6.11. Modified cross-relaxation imaging processing pipeline for cartilage imaging.

6.5.7 Results

As shown in the first row of figure 6.12, there was a large incremental increase in f with increasing collagen concentration. At the same time, the level of f associated with PG was minor compared with that of collagen at all concentrations, although some minimal incremental increase was observed in f with increasing PG concentration. No significant changes in both R and T_2^B were observed with increasing collagen and proteoglycan concentrations.

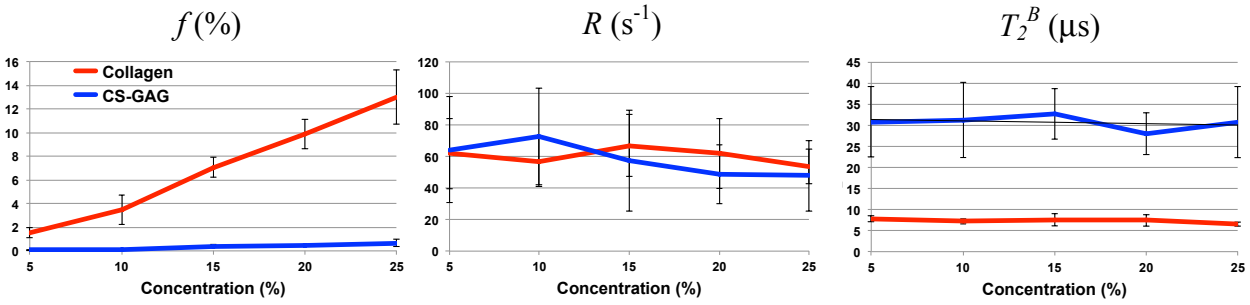

Figure 6.12. Comparison of qMT parameters estimated in phantoms with different concentrations of collagen and proteoglycan.

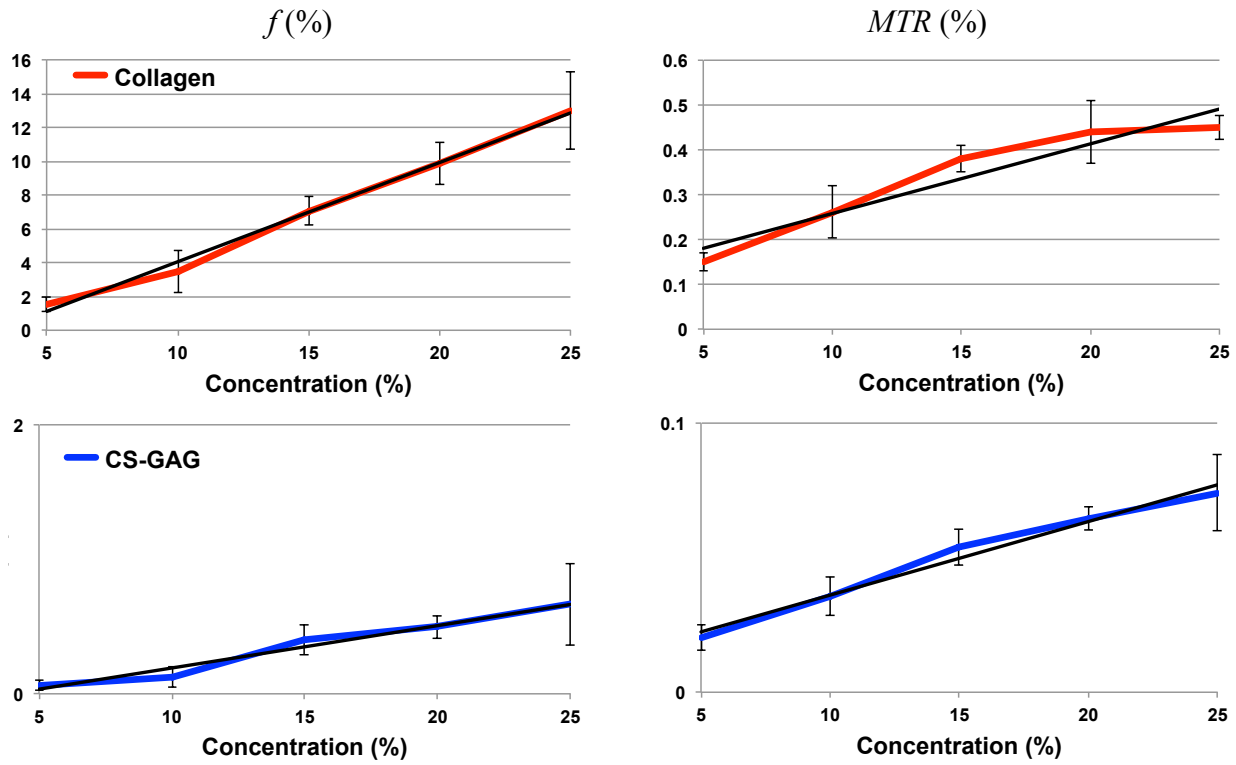

Figure 6.13. Comparison of bound pool fraction and MTR estimated in phantoms with different concentration of collagen and proteoglycan.

Figure 6.13 and table 6.3 show result of a linear regression analysis of bound pool fraction and *MTR* from both collagen and proteoglycan phantoms. There is a stronger correlation between bound pool fraction and concentration than *MTR* and concentration. Higher slope of fitted line for collagen shows higher sensitivity of bound pool fraction to the collagen concentration.

Table 6.3. Results of Linear Regression of Bound Pool Fraction and *MTR* in phantoms.

	***f* (%)**		***MTR***	
	Collagen	**Proteoglycan**	**Collagen**	**Proteoglycan**
R^2	0.993	0.972	0.917	0.982
Slope	2.94	0.158	0.078	0.014
Intercept	-1.82	-0.123	0.102	0.009

The dependence of qMT parameters on denaturation temperature is shown in figure 6.14. There was an incremental decrease in f and incremental increase in T_2^B with increasing temperature above the critical temperature threshold of 50°C when collagen denaturation begins. No significant changes in both R and MTR were observed with increasing the temperature.

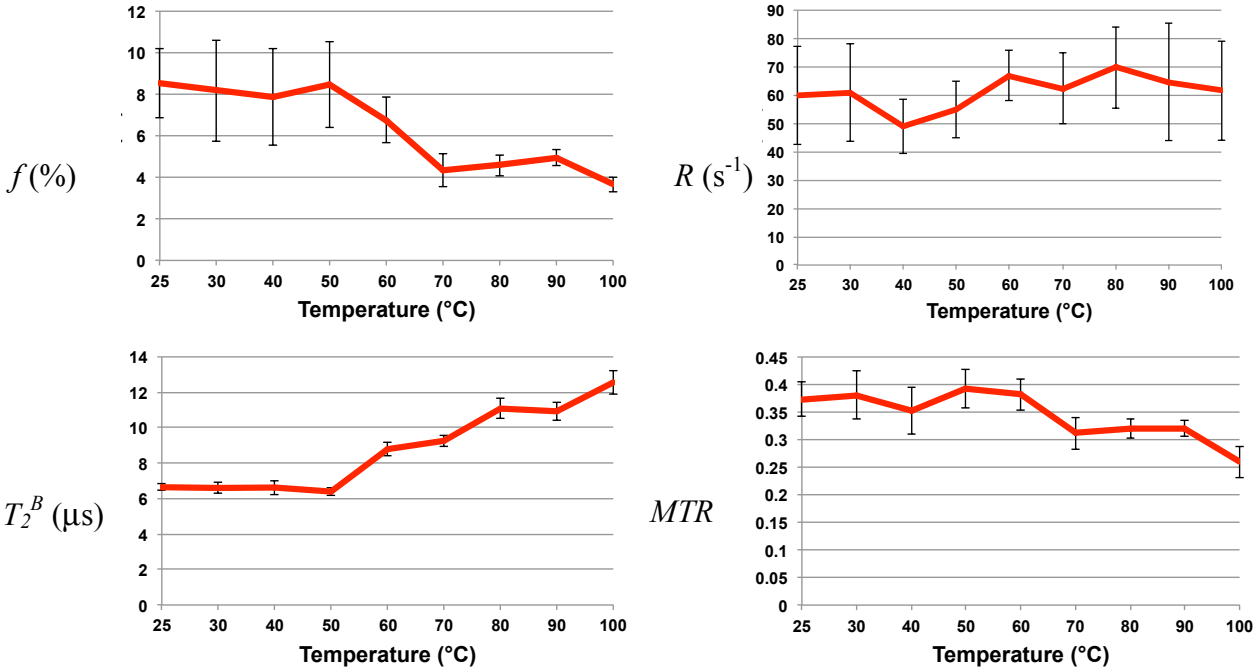

Figure 6.14. Comparison of qMT parameters and MTR with increasing the temperature.

As shown in figures 6.15 and 6.16, trypsin induced proteoglycan loss in bovine cartilage resulted in no significant change in f, but a decrease in R, and an increase in T_2^B.

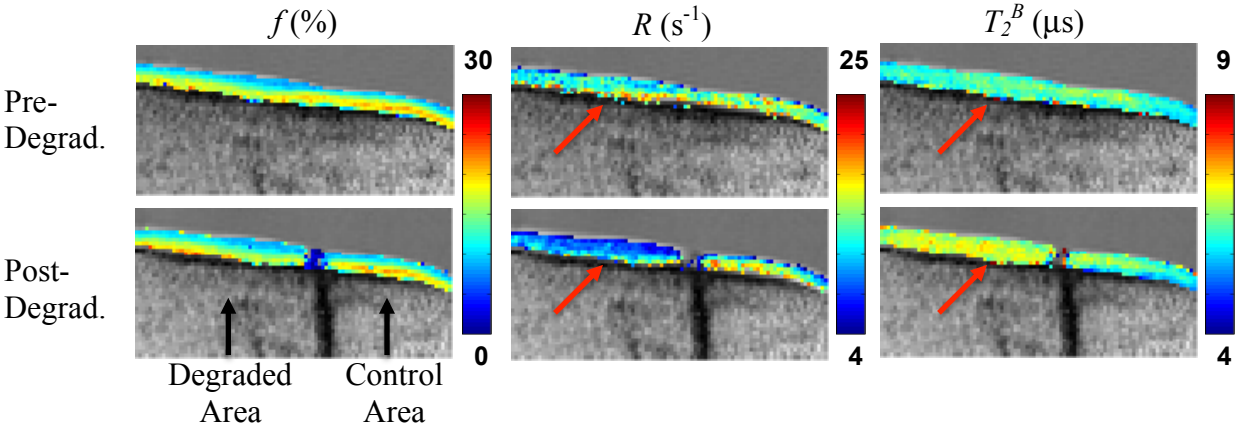

Figure 6.15. Ex-vivo proteoglycan degradation parametric maps. Significant decrease in R and increase in T_2^B after proteoglycan loss (red arrows).

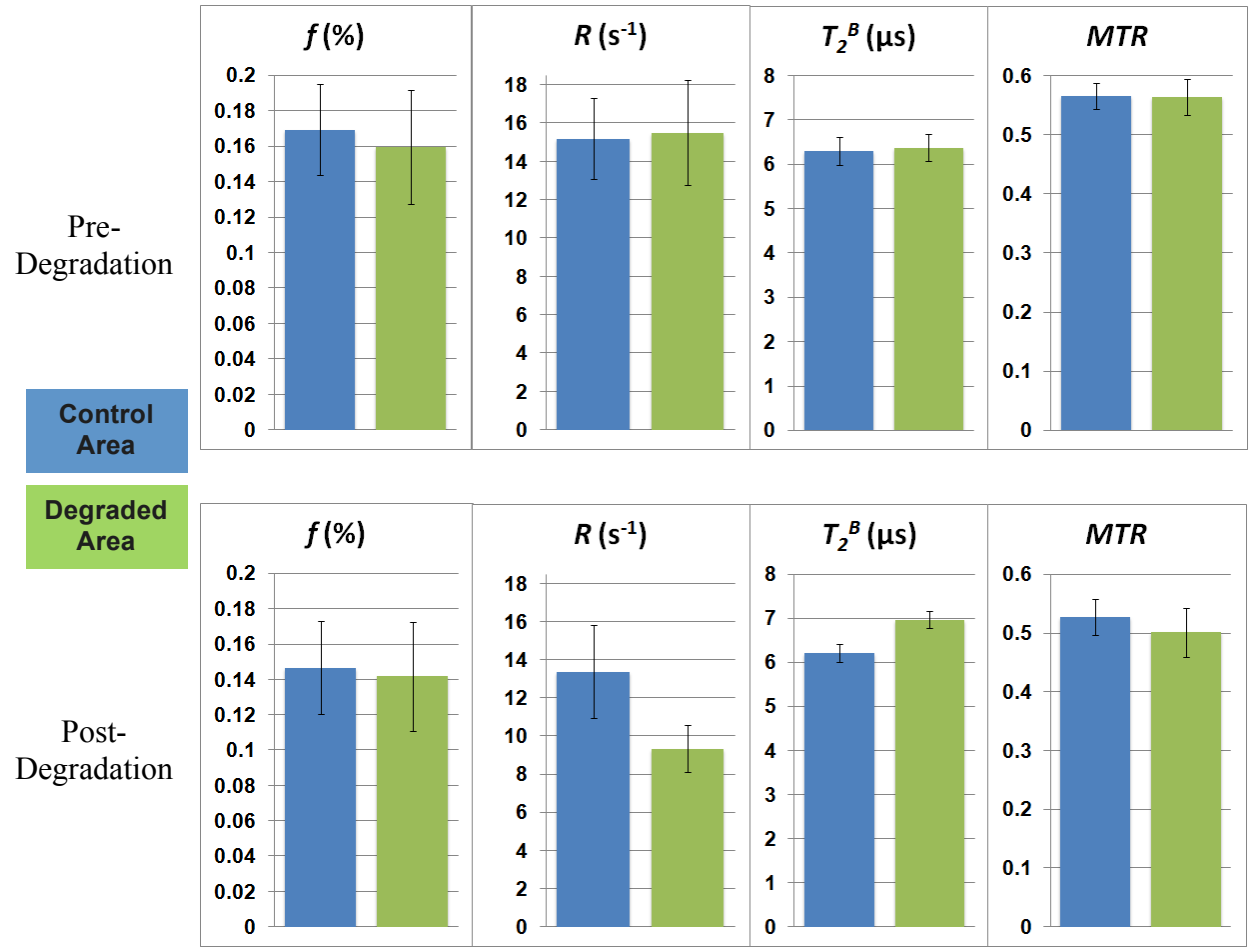

Figure 6.16. Ex-vivo proteoglycan degradation results. Significant reduction in R and increase in T_2^B after proteoglycan loss.

6.5.8 Discussion

Our study suggests that f is primarily influenced by the content of structurally intact collagen as f significantly increased with increasing collagen solution concentration and fragmentation of collagen solution due to thermal denaturation resulted in a decrease in f. The minimal influence of proteoglycan content on f is illustrated in both the phantom studies in which there was only a negligible increase in f with increasing proteoglycan solution concentration and the bovine cartilage study in which f did not change with proteoglycan loss

due to trypsin degradation. Also we have shown that the exchange rate (R) is strongly affected by proteoglycan content. Loss of proteoglycan within trypsin degraded bovine cartilage resulted in more than 35% decrease in R; this can be justified by the loss of the magnetization exchange pathways in cartilage (figure 6.8), where loss of proteoglycan removes the one of main magnetization exchange pathway between collagen and bulk water through proteoglycan. Also loss of bulk water from cartilage due to decreased proteoglycan content may reduce the exchange rate between mobile and collagen-bound protons. There is no significant change in R was seen with different collagen concentrations in phantoms.

Factors leading to changes in T_2^B appear to be more complex. Both thermal denaturation of collagen solution and loss of proteoglycan within trypsin degraded bovine cartilage resulted in an increase in T_2^B. Fragmentation of collagen due to denaturation may increase mobility of the molecules and thereby increase T_2^B. The decreased organization of the cartilage matrix due to proteoglycan loss may increase spin diffusion of collagen-bound protons, the primary mechanism defining T_2 relaxation time in the semisolid fraction (60), and thereby also increase T_2^B. However, exact mechanisms of the observed dependencies require further investigation.

Our results showing strong association of f with collagen content differ from those of previous studies which have shown that f is correlated with PG content in human cadaveric cartilage (133) and that trypsin degradation of bovine cartilage leads to a decrease in f (134). However, some previous studies have used qMT-fitting models, which fixed T_2^B. Such constraint may cause significant bias in the measurement of other qMT parameters if significant variability of T_2^B is present. The high sensitivity of T_2^B to denaturation of collagen solution and trypsin degradation of bovine cartilage noted in our study suggests that T_2^B may change

significantly with cartilage degeneration, and, hence, should be estimated along with the other qMT parameters. Another potential source of discrepancy is the differences in the measurement and estimation approaches. Also we have shown that the decrease in R can be an indicator of proteoglycan loss. While proteoglycan appears to provide minor contribution to bound pool fraction as measured by the two-pool MT model, it efficiently facilitates magnetization transfer between water and collagen. In conclusion, our study has shown that while some qMT measures may have utility for direct assessment of collagen content (*f*), multiple factors may be responsible for changes in qMT parameters at different stages of cartilage degradation. The observed trends and unique sensitivity of qMT measures to macromolecules, however, suggest that a multivariate analysis involving all qMT parameters may be the most specific method to analyze the complex changes, which occur during cartilage degeneration.

Chapter 7: Conclusion and Future Direction

Since its introduction by Wolff and Balaban in 1989 (19), magnetization transfer has been widely used in research and clinical studies to assess the information about the macromolecular content of tissue. Magnetization transfer imaging including both semi-quantitative, MT ratio (*MTR*) and MT-saturation (*MT-Sat*), and quantitative (qMT) approaches serve as natural indicators of tissue microstructural properties such as myelination level in both gray and white matter structures. The most common approach for characterizing MT effect is *MTR*, but this approach has several issues such as lack of reproducibility of *MTR* using different scanners and sequence parameters and also being sensitive to B_0 and B_1 inhomogeneities. Therefore, fully quantitative MT (qMT) methods are required to estimate all the parameter of MT model with high sensitivity and specificity to biological changes. The main goal of this dissertation was to develop, evaluate, and apply qMT imaging methods to correctly characterize the changes in biological tissues.

Chapter 1 and 2 of this dissertation introduced the fundamental theory of magnetic resonance imaging (MRI) and magnetization transfer (MT) imaging. In chapter 2 the most common MT model (two-pool model) was discussed and different MT methods was introduced.

Chapter 3 demonstrated the method mCRI to improve the accuracy of cross-relaxation imaging (CRI) by taking into account the contribution of bio-exponential longitudinal relaxation into variable flip angling (VFA) method. Two technical approaches have been develop to correct the biases in CRI parameter estimation caused by the MT-induced bi-exponential behavior of longitudinal relaxation of water spins based on either the global fit of both VFA and MT SPGR data to the two-pool signal model or the simple analytical recalculation formulas for key cross-relaxation parameters. While the choice between these techniques depends on a

tradeoff between the correction accuracy and image processing speed, both approaches do not require extra data compared to the original CRI method.

Chapter 4 introduced new fast and accurate f and T_1 mapping which considers the magnetization transfer effects. The optimized fast f and T_1 correction protocol developed in this work (VFA-MT) requires a single MT scan in addition to regular VFA measurements for accurate T_1 mapping. The presented approach is promising for fast high-resolution whole brain f and T_1 mapping with correction of MT effects within clinically acceptable scan times.

In Chapter 5, the new qMT model has been proposed where a two-pool MT subsystem is augmented by a third non-exchanging and very slowly exchanging (NE) pool. It has been shown that the partial volume effect with non- or slowly- exchanging compartments, i.e. CSF influences both *MTR* and key two-pool MT parameters. The proposed method (NE-mCRI) efficiently corrects the biases due to CSF partial volume effect in mCRI and may enable direct estimation of partial volume effect with CSF and circumvent assumptions of image-based estimation of partial volume effect during segmentation. The direct estimation of PVE may be potentially useful to improve accuracy of brain atrophy measurements in multiple sclerosis and Alzheimer disease, and in older patients who often have enlarged perivascular spaces and/or chronic lacunar infarcts filled with CSF.

Chapter 6 focused on the clinical application of qMT imaging method in brain and knee imaging. The new bound pool fraction mapping was applied in MS study along with other establish MRI methods such as *MTR*, T_1, and DTI for brain characterization in MS patients. The initial result of this ongoing study shows that bound pool fraction (f) has higher sensitivity in differentiating the normal appearing white matter for the lesion comparing to other parameters

including *MTR*, T_1, and DTI results. In knee imaging, we have shown that qMT parameters are useful in characterizing both collagen and proteoglycan content. Our results show that bound pool fraction appears to be an indicator of the content and the molecular structure of collagen while decrease in the exchange rate (*R*) can be an indicator of proteoglycan loss. The observed trends and unique sensitivity of mCRI parameters to macromolecules suggest that a multivariate analysis involving all parameters may be the most specific method to analyze the complex change occurring during cartilage degeneration.

Several studies have already applied different quantitative magnetization transfer method in brain imaging. New advances in qMT imaging such improving in the accuracy and shortening the scan time make the parameters of this method as new biomarker in the diagnosis of many human CNS diseases. Ideally, the combination of different quantitative MRI method such as qMT, DTI, and multicomponent relaxometry (mcDESPOT) can serve as a standard clinical setting to diagnose white matter/gray mater abnormalities and differentiate demyelination, inflammation, edema, and axonal degeneration in the brain of patients and if early detection of pathologic tissue changes, better discrimination between differently affected tissue, and sensitive monitoring of treatment response is possible.

References

1. Henkelman RM, Huang X, Xiang QS, Stanisz GJ, Swanson SD, Bronskill MJ. Quantitative interpretation of magnetization transfer. Magn Reson Med 1993;29(6):759-766.
2. Sled JG, Pike GB. Quantitative imaging of magnetization transfer exchange and relaxation properties in vivo using MRI. Magn Reson Med 2001;46(5):923-931.
3. Yarnykh VL. Pulsed Z-spectroscopic imaging of cross-relaxation parameters in tissues for human MRI: theory and clinical applications. Magn Reson Med 2002;47(5):929-939.
4. Ramani A, Dalton C, Miller DH, Tofts PS, Barker GJ. Precise estimate of fundamental in-vivo MT parameters in human brain in clinically feasible times. Magn Reson Imaging 2002;20(10):721-731.
5. Gochberg DF, Gore JC. Quantitative imaging of magnetization transfer using an inversion recovery sequence. Magn Reson Med 2003;49(3):501-505.
6. Tozer D, Ramani A, Barker GJ, Davies GR, Miller DH, Tofts PS. Quantitative magnetization transfer mapping of bound protons in multiple sclerosis. Magn Reson Med 2003;50(1):83-91.
7. Yarnykh VL, Yuan C. Cross-relaxation imaging reveals detailed anatomy of white matter fiber tracts in the human brain. Neuroimage 2004;23(1):409-424.
8. Ropele S, Seifert T, Enzinger C, Fazekas F. Method for quantitative imaging of the macromolecular 1H fraction in tissues. Magn Reson Med 2003;49(5):864-871.
9. Yarnykh VL. Fast macromolecular proton fraction mapping from a single off-resonance magnetization transfer measurement. Magn Reson Med 2012;68(1):166-178.

10. Dortch RD, Li K, Gochberg DF, Welch EB, Dula AN, Tamhane AA, Gore JC, Smith SA. Quantitative magnetization transfer imaging in human brain at 3 T via selective inversion recovery. Magn Reson Med 2011;66(5):1346-1352.

11. Gloor M, Scheffler K, Bieri O. Quantitative magnetization transfer imaging using balanced SSFP. Magn Reson Med 2008;60(3):691-700.

12. Soellinger M, Langkammer C, Seifert-Held T, Fazekas F, Ropele S. Fast bound pool fraction mapping using stimulated echoes. Magn Reson Med 2011;66(3):717-724.

13. Underhill HR, Rostomily RC, Mikheev AM, Yuan C, Yarnykh VL. Fast bound pool fraction imaging of the in vivo rat brain: association with myelin content and validation in the C6 glioma model. Neuroimage 2011;54(3):2052-2065.

14. Schmierer K, Tozer DJ, Scaravilli F, Altmann DR, Barker GJ, Tofts PS, Miller DH. Quantitative magnetization transfer imaging in postmortem multiple sclerosis brain. J Magn Reson Imaging 2007;26(1):41-51.

15. Ou X, Sun SW, Liang HF, Song SK, Gochberg DF. Quantitative magnetization transfer measured pool-size ratio reflects optic nerve myelin content in ex vivo mice. Magn Reson Med 2009;61(2):364-371.

16. Dula AN, Gochberg DF, Valentine HL, Valentine WM, Does MD. Multiexponential T2, magnetization transfer, and quantitative histology in white matter tracts of rat spinal cord. Magn Reson Med 2010;63(4):902-909.

17. Samsonov A, Alexander AL, Mossahebi P, Wu YC, Duncan ID, Field AS. Quantitative MR imaging of two-pool magnetization transfer model parameters in myelin mutant shaking pup. Neuroimage 2012;62(3):1390-1398.

18. Stanisz GJ, Odrobina EE, Pun J, Escaravage M, Graham SJ, Bronskill MJ, Henkelman RM. T1, T2 relaxation and magnetization transfer in tissue at 3T. Magn Reson Med 2005;54(3):507-512.

19. Wolff SD, Balaban RS. Magnetization transfer contrast (MTC) and tissue water proton relaxation in vivo. Magn Reson Med 1989;10(1):135-144.

20. Eng J, Ceckler TL, Balaban RS. Quantitative 1H magnetization transfer imaging in vivo. Magn Reson Med 1991;17(2):304-314.

21. Ceckler T, Maneval J, Melkowits B. Modeling magnetization transfer using a three-pool model and physically meaningful constraints on the fitting parameters. J Magn Reson 2001;151(1):9-27.

22. Le Bihan D, Turner R, Moonen CT, Pekar J. Imaging of diffusion and microcirculation with gradient sensitization: design, strategy, and significance. J Magn Reson Imaging 1991;1(1):7-28.

23. Le Bihan D, Moonen CT, van Zijl PC, Pekar J, DesPres D. Measuring random microscopic motion of water in tissues with MR imaging: a cat brain study. J Comput Assist Tomogr 1991;15(1):19-25.

24. Basser PJ, Mattiello J, LeBihan D. Estimation of the effective self-diffusion tensor from the NMR spin echo. J Magn Reson B 1994;103(3):247-254.

25. Basser PJ, Mattiello J, LeBihan D. MR diffusion tensor spectroscopy and imaging. Biophys J 1994;66(1):259-267.

26. Basser PJ. Inferring microstructural features and the physiological state of tissues from diffusion-weighted images. NMR Biomed 1995;8(7-8):333-344.

27. Basser PJ, Pierpaoli C. Microstructural and physiological features of tissues elucidated by quantitative-diffusion-tensor MRI. J Magn Reson B 1996;111(3):209-219.

28. Basser PJ, Pajevic S, Pierpaoli C, Duda J, Aldroubi A. In vivo fiber tractography using DT-MRI data. Magn Reson Med 2000;44(4):625-632.

29. Armspach JP, Gounot D, Rumbach L, Chambron J. In vivo determination of multiexponential T2 relaxation in the brain of patients with multiple sclerosis. Magn Reson Imaging 1991;9(1):107-113.

30. Menon RS, Allen PS. Application of continuous relaxation time distributions to the fitting of data from model systems and excised tissue. Magn Reson Med 1991;20(2):214-227.

31. Menon RS, Rusinko MS, Allen PS. Multiexponential proton relaxation in model cellular systems. Magn Reson Med 1991;20(2):196-213.

32. Stewart WA, MacKay AL, Whittall KP, Moore GR, Paty DW. Spin-spin relaxation in experimental allergic encephalomyelitis. Analysis of CPMG data using a non-linear least squares method and linear inverse theory. Magn Reson Med 1993;29(6):767-775.

33. MacKay A, Whittall K, Adler J, Li D, Paty D, Graeb D. In vivo visualization of myelin water in brain by magnetic resonance. Magn Reson Med 1994;31(6):673-677.

34. Whittall KP, MacKay AL, Graeb DA, Nugent RA, Li DK, Paty DW. In vivo measurement of T2 distributions and water contents in normal human brain. Magn Reson Med 1997;37(1):34-43.

35. Deoni SC, Rutt BK, Arun T, Pierpaoli C, Jones DK. Gleaning multicomponent T1 and T2 information from steady-state imaging data. Magn Reson Med 2008;60(6):1372-1387.

36. Ogawa S, Lee TM, Kay AR, Tank DW. Brain magnetic resonance imaging with contrast dependent on blood oxygenation. Proc Natl Acad Sci U S A 1990;87(24):9868-9872.

37. Ogawa S, Tank DW, Menon R, Ellermann JM, Kim SG, Merkle H, Ugurbil K. Intrinsic signal changes accompanying sensory stimulation: functional brain mapping with magnetic resonance imaging. Proc Natl Acad Sci U S A 1992;89(13):5951-5955.

38. Lossef SV, Rajan SS, Patt RH, Carvlin M, Calcagno D, Gomes MN, Barth KH. Gadolinium-enhanced magnitude contrast MR angiography of popliteal and tibial arteries. Radiology 1992;184(2):349-355.

39. Yucel EK. Magnetic resonance angiography of the peripheral arteries. Magn Reson Imaging Clin N Am 1993;1(2):229-238.

40. Prince MR. Gadolinium-enhanced MR aortography. Radiology 1994;191(1):155-164.

41. Korosec FR, Frayne R, Grist TM, Mistretta CA. Time-resolved contrast-enhanced 3D MR angiography. Magn Reson Med 1996;36(3):345-351.

42. Mistretta CA, Grist TM, Korosec FR, Frayne R, Peters DC, Mazaheri Y, Carrol TJ. 3D time-resolved contrast-enhanced MR DSA: advantages and tradeoffs. Magn Reson Med 1998;40(4):571-581.

43. Graham SJ, Henkelman RM. Understanding pulsed magnetization transfer. J Magn Reson Imaging 1997;7(5):903-912.

44. Morrison C, Henkelman RM. A model for magnetization transfer in tissues. Magn Reson Med 1995;33(4):475-482.

45. Quesson B, Thiaudière E, Delalande C, Dousset V, Chateil JF, Canioni P. Magnetization transfer imaging in vivo of the rat brain at 4.7 T: interpretation using a binary spin-bath model with a superLorentzian lineshape. Magn Reson Med 1997;38(6):974-980.

46. Dousset V, Grossman RI, Ramer KN, Schnall MD, Young LH, Gonzalez-Scarano F, Lavi E, Cohen JA. Experimental allergic encephalomyelitis and multiple sclerosis: lesion characterization with magnetization transfer imaging. Radiology 1992;182(2):483-491.

47. Stanisz GJ, Kecojevic A, Bronskill MJ, Henkelman RM. Characterizing white matter with magnetization transfer and T(2). Magn Reson Med 1999;42(6):1128-1136.

48. Lee RR, Dagher AP. Low power method for estimating the magnetization transfer bound-pool macromolecular fraction. J Magn Reson Imaging 1997;7(5):913-917.

49. VL Y. Analytical Method for Correction of B1 Errors in High-Field Magnetization Transfer Ratio Mapping. In Proceedings of the 17th Annual Meeting of ISMRM Honolulu, Hawai'i, USA2009. p 4482.

50. Alexander AL, Hurley SA, Samsonov AA, Adluru N, Hosseinbor AP, Mossahebi P, Tromp dP, Zakszewski E, Field AS. Characterization of cerebral white matter properties using quantitative magnetic resonance imaging stains. Brain Connect 2011;1(6):423-446.

51. Helms G, Dathe H, Kallenberg K, Dechent P. High-resolution maps of magnetization transfer with inherent correction for RF inhomogeneity and T1 relaxation obtained from 3D FLASH MRI. Magn Reson Med 2008;60(6):1396-1407.

52. Stanisz GJ, Webb S, Munro CA, Pun T, Midha R. MR properties of excised neural tissue following experimentally induced inflammation. Magn Reson Med 2004;51(3):473-479.

53. Mossahebi P, Yarnykh VL, Samsonov A. Analysis and correction of biases in cross-relaxation MRI due to biexponential longitudinal relaxation. Magn Reson Med 2013 (57905@N).

54. Morrison C, Stanisz G, Henkelman RM. Modeling magnetization transfer for biological-like systems using a semi-solid pool with a super-Lorentzian lineshape and dipolar reservoir. J Magn Reson B 1995;108(2):103-113.

55. Wang HZ, Riederer SJ, Lee JN. Optimizing the precision in T1 relaxation estimation using limited flip angles. Magn Reson Med 1987;5(5):399-416.

56. Bernstein MA, King KF, Zhou XJ. Handbook of MRI pulse sequences. Amsterdam ; Boston: Academic Press; 2004. p. p.

57. Portnoy S, Stanisz GJ. Modeling pulsed magnetization transfer. Magn Reson Med 2007;58(1):144-155.

58. Reeder SB, Pineda AR, Wen Z, Shimakawa A, Yu H, Brittain JH, Gold GE, Beaulieu CH, Pelc NJ. Iterative decomposition of water and fat with echo asymmetry and least-squares estimation (IDEAL): application with fast spin-echo imaging. Magn Reson Med 2005;54(3):636-644.

59. Yarnykh VL. Actual flip-angle imaging in the pulsed steady state: a method for rapid three-dimensional mapping of the transmitted radiofrequency field. Magn Reson Med 2007;57(1):192-200.

60. Edzes HT, Samulski ET. Cross relaxation and spin diffusion in the proton NMR or hydrated collagen. Nature 1977;265(5594):521-523.

61. Prantner AM, Bretthorst GL, Neil JJ, Garbow JR, Ackerman JJ. Magnetization transfer induced biexponential longitudinal relaxation. Magn Reson Med 2008;60(3):555-563.

62. Ou X, Gochberg DF. MT effects and T1 quantification in single-slice spoiled gradient echo imaging. Magn Reson Med 2008;59(4):835-845.

63. Bieri O, Scheffler K. On the origin of apparent low tissue signals in balanced SSFP. Magn Reson Med 2006;56(5):1067-1074.

64. RR E. Application of Fourier transform spectroscopyto magnetic resonance. In: WA A, editor. 1 ed. Volume 371966. p 93-102.

65. Koenig SH, Brown RD, Ugolini R. Magnetization transfer in cross-linked bovine serum albumin solutions at 200 MHz: a model for tissue. Magn Reson Med 1993;29(3):311-316.

66. Yarnykh VL. Optimal radiofrequency and gradient spoiling for improved accuracy of T1 and B1 measurements using fast steady-state techniques. Magn Reson Med 2010;63(6):1610-1626.

67. Underhill HR, Yuan C, Yarnykh VL. Direct quantitative comparison between cross-relaxation imaging and diffusion tensor imaging of the human brain at 3.0 T. Neuroimage 2009;47(4):1568-1578.

68. Mossahebi P SA. Rapid and accurate variable flip angle T1 mapping with correction of on-resonance MT effects In Proceedings of the 20th Annual Meeting of ISMRM Melbourne, Australia2012. p 4267.

69. Levesque IR, Pike GB. Characterizing healthy and diseased white matter using quantitative magnetization transfer and multicomponent T(2) relaxometry: A unified view via a four-pool model. Magn Reson Med 2009;62(6):1487-1496.

70. Does MD, Gore JC. Compartmental study of T(1) and T(2) in rat brain and trigeminal nerve in vivo. Magn Reson Med 2002;47(2):274-283.

71. Koenig SH, Brown RD, Spiller M, Lundbom N. Relaxometry of brain: why white matter appears bright in MRI. Magn Reson Med 1990;14(3):482-495.

72. Boulant N. T1 and T2 effects during radio-frequency pulses in spoiled gradient echo sequences. J Magn Reson 2009;197(2):213-218.

73. Odrobina EE, Lam TY, Pun T, Midha R, Stanisz GJ. MR properties of excised neural tissue following experimentally induced demyelination. NMR Biomed 2005;18(5):277-284.

74. Rausch M, Tofts P, Lervik P, Walmsley A, Mir A, Schubart A, Seabrook T. Characterization of white matter damage in animal models of multiple sclerosis by magnetization transfer ratio and quantitative mapping of the apparent bound proton fraction f. Mult Scler 2009;15(1):16-27.

75. Ou X, Sun SW, Liang HF, Song SK, Gochberg DF. The MT pool size ratio and the DTI radial diffusivity may reflect the myelination in shiverer and control mice. NMR Biomed 2009;22(5):480-487.

76. Deoni SC, Rutt BK, Peters TM. Rapid combined T1 and T2 mapping using gradient recalled acquisition in the steady state. Magn Reson Med 2003;49(3):515-526.

77. Vrenken H, Geurts JJ, Knol DL, van Dijk LN, Dattola V, Jasperse B, van Schijndel RA, Polman CH, Castelijns JA, Barkhof F, Pouwels PJ. Whole-brain T1 mapping in multiple sclerosis: global changes of normal-appearing gray and white matter. Radiology 2006;240(3):811-820.

78. Deoni SC. High-resolution T1 mapping of the brain at 3T with driven equilibrium single pulse observation of T1 with high-speed incorporation of RF field inhomogeneities (DESPOT1-HIFI). J Magn Reson Imaging 2007;26(4):1106-1111.

79. Bakshi R, Miletich RS, Kinkel PR, Emmet ML, Kinkel WR. High-resolution fluorodeoxyglucose positron emission tomography shows both global and regional cerebral hypometabolism in multiple sclerosis. J Neuroimaging 1998;8(4):228-234.

80. Cifelli A, Arridge M, Jezzard P, Esiri MM, Palace J, Matthews PM. Thalamic neurodegeneration in multiple sclerosis. Ann Neurol 2002;52(5):650-653.

81. Sanfilipo MP, Benedict RH, Sharma J, Weinstock-Guttman B, Bakshi R. The relationship between whole brain volume and disability in multiple sclerosis: a comparison of normalized gray vs. white matter with misclassification correction. Neuroimage 2005;26(4):1068-1077.

82. Bakshi R, Ariyaratana S, Benedict RH, Jacobs L. Fluid-attenuated inversion recovery magnetic resonance imaging detects cortical and juxtacortical multiple sclerosis lesions. Arch Neurol 2001;58(5):742-748.

83. Davies GR, Altmann DR, Hadjiprocopis A, Rashid W, Chard DT, Griffin CM, Tofts PS, Barker GJ, Kapoor R, Thompson AJ, Miller DH. Increasing normal-appearing grey and white matter magnetisation transfer ratio abnormality in early relapsing-remitting multiple sclerosis. J Neurol 2005;252(9):1037-1044.

84. Sharma J, Zivadinov R, Jaisani Z, Fabiano AJ, Singh B, Horsfield MA, Bakshi R. A magnetization transfer MRI study of deep gray matter involvement in multiple sclerosis. J Neuroimaging 2006;16(4):302-310.

85. Khaleeli Z, Altmann DR, Cercignani M, Ciccarelli O, Miller DH, Thompson AJ. Magnetization transfer ratio in gray matter: a potential surrogate marker for progression in early primary progressive multiple sclerosis. Arch Neurol 2008;65(11):1454-1459.

86. Fabiano AJ, Sharma J, Weinstock-Guttman B, Munschauer FE, Benedict RH, Zivadinov R, Bakshi R. Thalamic involvement in multiple sclerosis: a diffusion-weighted magnetic resonance imaging study. J Neuroimaging 2003;13(4):307-314.

87. Bermel RA, Puli SR, Rudick RA, Weinstock-Guttman B, Fisher E, Munschauer FE, Bakshi R. Prediction of longitudinal brain atrophy in multiple sclerosis by gray matter magnetic resonance imaging T2 hypointensity. Arch Neurol 2005;62(9):1371-1376.

88. Bakshi R, Lindsay BD, Bates VE, Kinkel PR, Mechtler LL, Kinkel WR. Cerebral venous infarctions presenting as enhancing space-occupying lesions: MRI findings. J Neuroimaging 1998;8(4):210-215.

89. Kidd D, Barkhof F, McConnell R, Algra PR, Allen IV, Revesz T. Cortical lesions in multiple sclerosis. Brain 1999;122 (Pt 1):17-26.

90. Peterson JW, Bö L, Mörk S, Chang A, Trapp BD. Transected neurites, apoptotic neurons, and reduced inflammation in cortical multiple sclerosis lesions. Ann Neurol 2001;50(3):389-400.

91. Bakshi R. Solitary inflammatory demyelination in the brain or spinal cord with tumor-like MRI presentations. Arch Neurol 2001;58(4):677.

92. Minagar A. Gray matter involvement in multiple sclerosis: a new window into pathogenesis. J Neuroimaging 2003;13(4):291-292.

93. Bermel RA, Innus MD, Tjoa CW, Bakshi R. Selective caudate atrophy in multiple sclerosis: a 3D MRI parcellation study. Neuroreport 2003;14(3):335-339.

94. Tjoa CW, Benedict RH, Weinstock-Guttman B, Fabiano AJ, Bakshi R. MRI T2 hypointensity of the dentate nucleus is related to ambulatory impairment in multiple sclerosis. J Neurol Sci 2005;234(1-2):17-24.

95. Geurts JJ, Pouwels PJ, Uitdehaag BM, Polman CH, Barkhof F, Castelijns JA. Intracortical lesions in multiple sclerosis: improved detection with 3D double inversion-recovery MR imaging. Radiology 2005;236(1):254-260.

96. Li JG, Graham SJ, Henkelman RM. A flexible magnetization transfer line shape derived from tissue experimental data. Magn Reson Med 1997;37(6):866-871.

97. Koo BB, Hua N, Choi CH, Ronen I, Lee JM, Kim DS. A framework to analyze partial volume effect on gray matter mean diffusivity measurements. Neuroimage 2009;44(1):136-144.

98. Deoni SC, Matthews L, Kolind SH. One component? Two components? Three? The effect of including a nonexchanging "free" water component in multicomponent driven equilibrium single pulse observation of T1 and T2. Magn Reson Med 2013;70(1):147-154.

99. Yang AW, Jensen JH, Hu CC, Tabesh A, Falangola MF, Helpern JA. Effect of cerebral spinal fluid suppression for diffusional kurtosis imaging. J Magn Reson Imaging 2013;37(2):365-371.

100. McQuarrie ADR, Tsai C-L. Regression and time series model selection. Singapore ; River Edge, N.J.: World Scientific; 1998. xxi, 455 p. p.

101. Siegel GJ. Basic neurochemistry : molecular, cellular, and medical aspects. Burlington, MA: Elsevier Academic; 2006. xxiv, 992 p. p.

102. Whetten-Goldstein K, Sloan FA, Goldstein LB, Kulas ED. A comprehensive assessment of the cost of multiple sclerosis in the United States. Mult Scler 1998;4(5):419-425.

103. Adelman G, Rane SG, Villa KF. The cost burden of multiple sclerosis in the United States: a systematic review of the literature. J Med Econ 2013;16(5):639-647.

104. Young IR, Hall AS, Pallis CA, Legg NJ, Bydder GM, Steiner RE. Nuclear magnetic resonance imaging of the brain in multiple sclerosis. Lancet 1981;2(8255):1063-1066.

105. Rovaris M, Filippi M. Magnetic resonance techniques to monitor disease evolution and treatment trial outcomes in multiple sclerosis. Curr Opin Neurol 1999;12(3):337-344.

106. Filippi M, Horsfield MA, Adèr HJ, Barkhof F, Bruzzi P, Evans A, Frank JA, Grossman RI, McFarland HF, Molyneux P, Paty DW, Simon J, Tofts PS, Wolinsky JS, Miller DH. Guidelines for using quantitative measures of brain magnetic resonance imaging abnormalities in monitoring the treatment of multiple sclerosis. Ann Neurol 1998;43(4):499-506.

107. Filippi M, Rocca MA, Martino G, Horsfield MA, Comi G. Magnetization transfer changes in the normal appearing white matter precede the appearance of enhancing lesions in patients with multiple sclerosis. Ann Neurol 1998;43(6):809-814.

108. Inglese M. Multiple sclerosis: new insights and trends. AJNR Am J Neuroradiol 2006;27(5):954-957.

109. Katz D, Taubenberger JK, Cannella B, McFarlin DE, Raine CS, McFarland HF. Correlation between magnetic resonance imaging findings and lesion development in chronic, active multiple sclerosis. Ann Neurol 1993;34(5):661-669.

110. Bitsch A, Kuhlmann T, Stadelmann C, Lassmann H, Lucchinetti C, Brück W. A longitudinal MRI study of histopathologically defined hypointense multiple sclerosis lesions. Ann Neurol 2001;49(6):793-796.

111. Fisher E, Chang A, Fox RJ, Tkach JA, Svarovsky T, Nakamura K, Rudick RA, Trapp BD. Imaging correlates of axonal swelling in chronic multiple sclerosis brains. Ann Neurol 2007;62(3):219-228.

112. Kappos L, Moeri D, Radue EW, Schoetzau A, Schweikert K, Barkhof F, Miller D, Guttmann CR, Weiner HL, Gasperini C, Filippi M. Predictive value of gadolinium-enhanced magnetic resonance imaging for relapse rate and changes in disability or impairment in multiple sclerosis: a meta-analysis. Gadolinium MRI Meta-analysis Group. Lancet 1999;353(9157):964-969.

113. Molyneux PD, Barker GJ, Barkhof F, Beckmann K, Dahlke F, Filippi M, Ghazi M, Hahn D, MacManus D, Polman C, Pozzilli C, Kappos L, Thompson AJ, Wagner K, Yousry T, Miller DH, MS ESGoIB-biSP. Clinical-MRI correlations in a European trial of interferon beta-1b in secondary progressive MS. Neurology 2001;57(12):2191-2197.

114. Zivadinov R, Bakshi R. Role of MRI in multiple sclerosis I: inflammation and lesions. Front Biosci 2004;9:665-683.

115. Zivadinov R, Bakshi R. Role of MRI in multiple sclerosis II: brain and spinal cord atrophy. Front Biosci 2004;9:647-664.

116. Bakshi R, Minagar A, Jaisani Z, Wolinsky JS. Imaging of multiple sclerosis: role in neurotherapeutics. NeuroRx 2005;2(2):277-303.

117. Filippi M, Rocca MA. Conventional MRI in multiple sclerosis. J Neuroimaging 2007;17 Suppl 1:3S-9S.

118. Filippi M, Horsfield MA, Morrissey SP, MacManus DG, Rudge P, McDonald WI, Miller DH. Quantitative brain MRI lesion load predicts the course of clinically isolated syndromes suggestive of multiple sclerosis. Neurology 1994;44(4):635-641.

119. Filippi M, Paty DW, Kappos L, Barkhof F, Compston DA, Thompson AJ, Zhao GJ, Wiles CM, McDonald WI, Miller DH. Correlations between changes in disability and

T2-weighted brain MRI activity in multiple sclerosis: a follow-up study. Neurology 1995;45(2):255-260.

120. Molyneux PD, Filippi M, Barkhof F, Gasperini C, Yousry TA, Truyen L, Lai HM, Rocca MA, Moseley IF, Miller DH. Correlations between monthly enhanced MRI lesion rate and changes in T2 lesion volume in multiple sclerosis. Ann Neurol 1998;43(3):332-339.

121. Sailer M, O'Riordan JI, Thompson AJ, Kingsley DP, MacManus DG, McDonald WI, Miller DH. Quantitative MRI in patients with clinically isolated syndromes suggestive of demyelination. Neurology 1999;52(3):599-606.

122. Brex PA, Ciccarelli O, O'Riordan JI, Sailer M, Thompson AJ, Miller DH. A longitudinal study of abnormalities on MRI and disability from multiple sclerosis. N Engl J Med 2002;346(3):158-164.

123. Pierpaoli C, Basser PJ. Toward a quantitative assessment of diffusion anisotropy. Magn Reson Med 1996;36(6):893-906.

124. Duncan ID, Brower A, Kondo Y, Curlee JF, Schultz RD. Extensive remyelination of the CNS leads to functional recovery. Proc Natl Acad Sci U S A 2009;106(16):6832-6836.

125. Filippi M, Inglese M, Rovaris M, Sormani MP, Horsfield P, Iannucci PG, Colombo B, Comi G. Magnetization transfer imaging to monitor the evolution of MS: a 1-year follow-up study. Neurology 2000;55(7):940-946.

126. Sled JG, Levesque I, Santos AC, Francis SJ, Narayanan S, Brass SD, Arnold DL, Pike GB. Regional variations in normal brain shown by quantitative magnetization transfer imaging. Magn Reson Med 2004;51(2):299-303.

127. Venn M, Maroudas A. Chemical composition and swelling of normal and osteoarthrotic femoral head cartilage. I. Chemical composition. Ann Rheum Dis 1977;36(2):121-129.

128. Squires GR, Okouneff S, Ionescu M, Poole AR. The pathobiology of focal lesion development in aging human articular cartilage and molecular matrix changes characteristic of osteoarthritis. Arthritis Rheum 2003;48(5):1261-1270.

129. Billinghurst RC, Dahlberg L, Ionescu M, Reiner A, Bourne R, Rorabeck C, Mitchell P, Hambor J, Diekmann O, Tschesche H, Chen J, Van Wart H, Poole AR. Enhanced cleavage of type II collagen by collagenases in osteoarthritic articular cartilage. J Clin Invest 1997;99(7):1534-1545.

130. Burstein D, Hunter DJ. "Why aren't we there yet?" Re-examining standard paradigms in imaging of OA: summary of the 2nd annual workshop on imaging based measures of osteoarthritis. Osteoarthritis Cartilage 2009;17(5):571-578.

131. Qvist P, Bay-Jensen AC, Christiansen C, Dam EB, Pastoureau P, Karsdal MA. The disease modifying osteoarthritis drug (DMOAD): Is it in the horizon? Pharmacol Res 2008;58(1):1-7.

132. Henkelman RM, Stanisz GJ, Graham SJ. Magnetization transfer in MRI: a review. NMR Biomed 2001;14(2):57-64.

133. Sritanyaratana N SA, Hurley SA, Johnson KM, Mossahebi P, Block WF, Kijowski R. Quantitative Magnetization Transfer of Entire Human Patellofemoral Joint in 30 Minutes. In Proceedings of the 19th Annual Meeting of ISMRM Montréal, Québec, Canada2011. p 3231.

134. Stikov N, Keenan KE, Pauly JM, Smith RL, Dougherty RF, Gold GE. Cross-relaxation imaging of human articular cartilage. Magn Reson Med 2011;66(3):725-734.

135. Henkelman RM, Stanisz GJ, Menezes N, Burstein D. Can MTR be used to assess cartilage in the presence of Gd-DTPA2-? Magn Reson Med 2002;48(6):1081-1084.

136. Lattanzio PJ, Marshall KW, Damyanovich AZ, Peemoeller H. Macromolecule and water magnetization exchange modeling in articular cartilage. Magn Reson Med 2000;44(6):840-851.

137. Harel A, Eliav U, Akselrod S, Navon G. Magnetization transfer based contrast for imaging denatured collagen. J Magn Reson Imaging 2008;27(5):1155-1163.